Florida International University

FIU Digital Commons

2-13-2020

Constructal Design and Aeroelastic Stability Analysis of HALE Aircraft

Ehsan Izadpanahi
eizad001@fiu.edu

Follow this and additional works at: https://digitalcommons.fiu.edu/etd

Part of the Aerospace Engineering Commons, and the Mechanical Engineering Commons

FLORIDA INTERNATIONAL UNIVERSITY

Miami, Florida

CONSTRUCTAL DESIGN AND AEROELASTIC STABILITY ANALYSIS OF

HALE AIRCRAFT

A dissertation submitted in partial fulfillment of the

requirements for the degree of

DOCTOR OF PHILOSOPHY

in

MECHANICAL ENGINEERING

by

Ehsan Izadpanahi

2020

To: John L. Volakis
    College of Engineering and Computing

This dissertation, written by Ehsan Izadpanahi, and entitled Constructal Design and Aeroelastic Stability Analysis of HALE Aircraft, having been approved in respect to style and intellectual content, is referred to you for judgment.

We have read this dissertation and recommend that it be approved.

_____
Cesar Levy

_____
Ibrahim Nur Tansel

_____
Cheng-Xian Lin

_____
Sakhrat Khizroev

_____
Pezhman Mardanpour, Major Professor

Date of Defense: February 13, 2020

The dissertation of Ehsan Izadpanahi is approved.

_____
John L. Volakis
College of Engineering and Computing

_____
Andrés G. Gil
Vice President for Research and Economic Development
and Dean of the University Graduate School

Florida International University, 2020

DEDICATION

To my parents.

I am grateful for your continuous support and sacrifice.

ACKNOWLEDGMENTS

ABSTRACT OF THE DISSERTATION

CONSTRUCTAL DESIGN AND AEROELASTIC STABILITY ANALYSIS OF

HALE AIRCRAFT

by

Ehsan Izadpanahi

Florida International University, 2020

Miami, Florida

Professor Pezhman Mardanpour, Major Professor

In the new generation of the Unmanned Aerial Vehicle (UAV), the capability of increasing the flight duration and altitude is the area of interest for designers. The High-Altitude Long-Endurance (HALE) aircraft can fly farther and for a longer period by using high aspect ratio flexible wings. The primary applications and flight missions of this type of aircraft are environmental monitoring, surveillance, and communications. While using high-aspect-ratio, flexible, light-weighted wings improve the efficiency and reduces the required power, it will bring new challenges into the design of the aircraft. One of the major concerns is aeroelastic instability, which can appear as flutter, divergence, limit cycle oscillation, etc.

The main objectives of this research are to investigate the effects of different design parameters on the aeroelastic stability of HALE aircraft. I seek to find the reason why certain configurations can extend the aeroelastic flight envelope and postpone the instabilities. A numerical package is developed that connects three computer programs; Gmsh, Nonlinear Aeroelastic Trim And Stability of HALE Aircraft (NATASHA), and Variational Asymptotic Beam Sectional Analysis (VABS). The Gmsh software provides a discretized model of the wing cross-section of the aircraft. The wing data is then imported to VABS software to obtain the structural and inertial properties. NATASHA uses the structural and inertial properties of the

sections to perform stability analysis, and the results of the trim solution are imported to VABS software for stress analysis. VABS uses the trim solution to recover the stresses.

Different design parameters such as engine/store location and wing sweep and curvature are considered, and the nonlinear aeroelastic analyses are performed. Most of the studies on the effects of design parameters on aeroelastic stability take a descriptive approach, and they use the state-of-the-art numerical techniques to compare the performance of different designs and reveal the best of the options available. In the present study, I shed light on how a certain design parameter could influence the flow in the system, including the flow of stresses and how changing the geometry in the direction that provides greater access to the currents flowing through it, leads to a better design. I propose how the configuration should evolve towards a better design by facilitating the flow of stresses. This approach stems from constructal law.

TABLE OF CONTENTS

LIST OF TABLES

LIST OF FIGURES

Nomenclature

a	Deformed beam aerodynamic frame of reference
b	Undeformed beam cross-sectional frame of reference
B	Deformed beam cross-sectional frame of reference
b_i	Unit vectors in undeformed beam cross-sectional frame ($i = 1, 2, 3$)
B_i	Unit vectors of deformed beam cross-sectional frame ($i = 1, 2, 3$)
c	Chord
C^{bi}	Transformation matrix from the inertial frame i to deformed frame b
C^{Bi}	Transformation matrix from the inertial frame i to deformed frame B
C^{ib}	Transformation matrix from the undeformed frame b to inertial frame i
C^{iB}	Transformation matrix from the deformed frame B to inertial frame i
c_{d_0}, c_{l_0}	Aerodynamic drag and lift coefficients at zero angle of attack
$c_{m\beta}$	Pitch moment coefficient w.r.t. flap deflection (β)
$c_{l\alpha}$	Lift coefficient w.r.t. angle of attack (α)
$c_{l\beta}$	Lift coefficient w.r.t. flap deflection (β)
e_1	Column matrix
e	Offset of aerodynamic center from the origin of frame of reference along b_2
f	Column matrix of distributed, applied force measured in B_i basis
F	Column matrix of internal force measured in B_i basis
$\mathbf{g}$	Gravitational vector in B_i basis
H	Column matrix of cross-sectional angular momentum measured in B_i basis
i	Inertial frame of reference
$\mathbf{i}_i$	Unit vectors for inertial frame of reference ($i = 1, 2, 3$)
I	Cross-sectional inertia matrix
k	Column matrix of initial curvature and twist measured in b_i basis
K	Column matrix of deformed beam curvature and twist measured in B_i basis

m	Column matrix of distributed, applied moment measured in B_i basis
M	Column matrix of internal moment measured in B_i basis
P	Column matrix of cross-sectional linear momentum measured in B_i basis
r	Column matrix of position vector measured in b_i basis
u	Column matrix of displacement vector measured in b_i basis
V	Column matrix of velocity measured in B_i basis
x_1	Axial coordinate of beam
α	Angle of attack
β	Trailing edge flap angle
γ	Column matrix of 1D generalized force strain measures
Δ	Identity matrix
κ	Column matrix of elastic twist and curvature measures
λ	Column matrix of induced flow states
μ	Mass per unit length
ξ	Column matrix of center of mass offset from the frame of reference origin
ρ	Air density
ψ	Column matrix of small incremental rotations
Ω	Column matrix of cross-sectional angular velocity
$(\ )'$	Partial derivative with respect to x_1
$\dot{(\ )}$	Partial derivative with respect to time
$\hat{(\ )}$	Nodal variable

CHAPTER 1

INTRODUCTION

1.1   History of Unmanned Aircraft Systems

To define Unmanned Aircraft Systems (UASs), the unmanned system must have a flying vehicle. Unmanned aircraft are called drone, remotely piloted vehicle or aircraft (RPV or RPA), Unmanned Aerial Vehicle (UAV), and many more. UASs must consist of an airborne component in order to operate a task without a pilot on board and capable of a sustainable flight [36].

In 1896 a steam-powered aircraft flew over the Potomac River. This aircraft was launched by Samuel Pierpont Langley using a catapult launcher. This unmanned aircraft traveled for a mile with no guidance system. Later in 1918, gyroscope was used by Elmer Sperry as a simple tool for autopilot flight for both manned and unmanned aircraft. During World War I, the Kettering Bug program employed an unmanned biplane, which was designed to navigate up to 40 miles to the target. However, the development of UAS stopped until World War II, which Germany developed air-to-ground guided munitions and cruise missiles that significantly advanced UAS technology. Up to late 1980 and early 1990 a variety of systems was developed, such as the first operational unmanned helicopter (Gyrodyne QH-50), or the Lockheed D-21 and many more systems. However, due to the immature technologies, these systems had limited capabilities and effectiveness [36].

With the advancement in the Global Positioning Systems (GPS), electronics and satellite communication, the designs of UAS entered the modern era. The Boeing Condor Program funded by DARPA was the first UAS to use GPS navigation and auto-landing technology. Although it did not become operational, Condor set the bar for later systems, capable of enduring 59 hours of operation time and reaching

a maximum altitude of 67,000 ft. Following the Condor program, new systems such as the General Atomics Predator, Teledyne Ryan Global Hawk, and the Lockheed DarkStar were developed. These aircraft were the first to perform operations that could go beyond-line-of-sight using high-bandwidth digital satellite communications links [36].

Mission requirements are the bases of any design of UASs. One of the most widely known UASs is Predator, due to its contribution to recent conflicts in Iraq and Afghanistan and appearance in many movies and TV shows. Although UASs have been used in military applications, they are not limited to these missions. Currently, there are four categories of UAS recognized by the Federal Aviation Administration (FAA): recreational, commercial, governmental, and educational. This vast range of applications led to numerous designs and configurations, with different complexities.

There are many types of UAS; some are presented in Fig. 1.1. Small Unmanned Aircraft Systems (SUAS) are lightweight but still larger than Micro Air Vehicles (MAV). MAVs have a maximum physical length of 6 inches with weight less than 0.5 lb, while SUAS has a gross weight between 1 to 55 lb. SUAS and MAV are electrically powered with half an hour to two-hour endurance. Another category of UAS is the medium to long endurance and usually low-altitude. They have a gross weight between 1,000 to 10,000 lb capable of carrying large payloads and flying for 12 to 40 hours [36].

Another type of UAV is the High-Altitude Long-Endurance (HALE) aircraft that is designed to achieve flights with more than 24 hours at high altitudes. Some divide this category into two different sub-categories that distinguish the long-endurance and ultra-long-endurance UAVS. However, this research stays with the definition of HALE aircraft that encompass both long-endurance and ultra-long-endurance
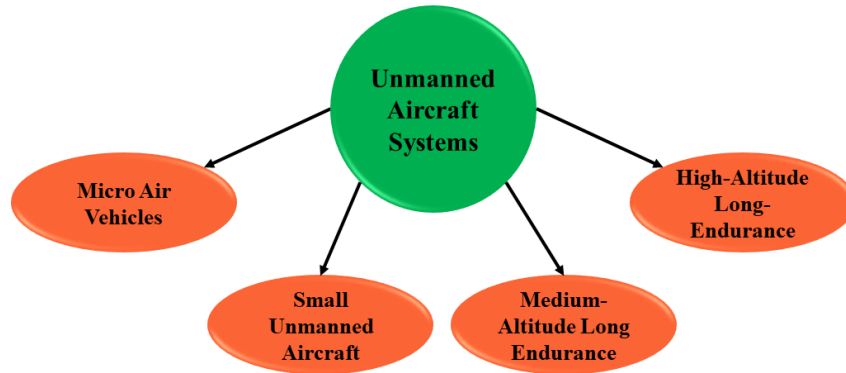
Figure 1.1: Classification of unmanned aircraft systems

UAVS. From Northrop Grumman Global Hawk (RQ-4B) that can fly for 33 hour at maximum altitude of 65,000 feet to Airbus Zephyr SE model that is a solar powered aircraft that can fly at 70,000 feet altitude and has a flight endurance record of more than 25 days, are examples of HALE aircraft.

1.2 High-Altitude Long-Endurance (HALE) Aircraft

HALE aircraft concept goes back to the early 1980's [38, 105]. One of the earliest designs was the Pathfinder solar-powered aircraft that was developed under a classified governmental program. NASA was also sponsoring an Environmental Research and Sensor Technology (ERAST) program that was tasked with developing high-altitude UASs to gather data of the upper atmosphere. NASA wanted to measure the ozone hole phenomenon, which was an issue that was highly talked about at the time but not well understood. The Aurora Flight Sciences – Perseus, AeroVironment – Pathfinder (solar-powered), General Atomics -Atlus, and Scaled Composites

-Raptor were developed under this program. Although these high-altitude UAVs were not used primarily for their original missions, the technologies developed like groundbreaking airframes and propulsion systems had a heavy impact on the advancement of UASs.

This type of aircraft has a wide range of flight missions, from earth science missions, such as extreme weather observation and oceanographic research, to government services such as forest fire damage assessment and border and coastal patrol, to civil missions like sat-cell phone services and agriculture yield maximizing.

1.3 Aeroelastic Instability

Aeroelasticity deals with the interaction between elasticity, aerodynamics, and dynamics [43]. According to Fung [31], aeroelasticity covers the effects of aerodynamic forces on an elastic body. While in classical elasticity, the external loading is independent of the structure's deformation, in aeroelasticity the body deformation plays a critical role in determining the aerodynamic forces. The most common problem in aeroelasticity is stability analysis. Aerospace structures may experience instability during flight. There are different types of aeroelastic instabilities, such as divergence, flutter, and Limit Cycle Oscillation (LCO) [46].

According to Hodges [43] "flutter is a self-excited and potentially destructive oscillatory instability in which aerodynamic forces on a flexible body couple with its natural modes of vibration to produce oscillatory motions with increasing amplitude." There is no clear explanation in the literature to discuss why this phenomenon occurs. Fung [31] explains that flutter happens because "the speed of flow affects the amplitude ratios and phase shifts between motion in various degrees of freedom in such a way that energy can be absorbed by the airfoil from the airstream

4

passing by." Bendiksen [18] explained that in order for the flutter to happen, wings must extract the energy from the airstream. This can cause the inability of the structure of the aircraft's structure to compensate for the aerodynamic, elastic, and inertial forces [46].

On the other hand, divergence is a static instability. Hodges [43] explains that "When this [the aerodynamic forces overpower the elastic forces] occurs such that inertial forces have little effect, we refer to this as a static-aeroelastic instability – or divergence." He [43] further explains that "divergence occurs when a lifting surface deforms under aerodynamic loads in such a way as to increase the applied load, and the increased load deflects the structure further — eventually to the point of failure."

The real events in nature, however, can be different from the results of linear analysis, such as flutter and divergence. In an actual aircraft, flying at the speeds below flutter, there is a possibility for the self-excited oscillations to develop. Additionally, other conditions in the atmosphere, such as gust can destabilize a system that was predicted to be stable by linear analysis. These situations can result in a steady–state periodic oscillations called limit cycle oscillations [43]. According to Hodges [43] "there can be fatigue problems leading to concerns about the life of certain components of an aircraft as well as passenger comfort and pilot endurance. To capture such behavior in an analysis, the aircraft must be treated as a nonlinear system."

1.4   Constructal Law

The constructal law explains that the design evolution is a universal physics phenomenon [6, 14, 15]. It states [5]: "For a finite-size flow system to persist in time (to

live), its configuration must *evolve* freely such that it provides greater and greater access to the currents that flow through it."

The key concept is thinking of flow systems in nature. Flow, the movement of one entity relative to another is described by what the flow carries (fluid, heat, mass, electricity, stress, etc.), how much it carries (flow rate, current, etc.), and where the stream is located (i.e., how it is configured). The "where" (i.e., the configuration in space and time) is the focus of the constructal theories that stem from the constructal law [10, 11, 12, 46]. The constructal law accounts for the emergence and evolution of shape and structure in the flow configurations of any system that has the freedom to change [46].

The optimization methods search through a predefined existing arrangements and chose the one that is suitable for the design objectives. With the constructal law, the designer *discovers* the configuration without any presumptions, and *constructs* the missing geometry from the principles. Unlike optimization, the constructal approach enables the design to transform and evolve toward the better [46].

From engineering [6] to biology [13], there is a large body of knowledge concerning the application of the Constructal Law in design that shows the successful implementation of the constructal theories for the analysis and design of systems [46]. These applications include mechanical structures [57]; thermal structures [54, 61, 78, 92, 104]; heat, fluid, and power distribution systems [2, 15, 76]; porous structures [3, 56, 58, 101]; transportation and economic structures [8, 98]; product design [19, 40, 41]; physics of life [7]; human dynamic, security, and sustainability [16, 75].

1.5   Project Motivation and Research Objectives

In June 2003, the Helios prototype, which was a highly flexible ultra-lightweight flying wing, crashed during the flight test. During the flight, the aircraft experienced normal turbulence, which led to an unexpected high wing dihedral. Then the aircraft became unstable, and the leading edge failed. One of the reasons behind the crash was reported as: "Lack of adequate analysis methods led to an inaccurate risk assessment of the effects of configuration changes leading to an inappropriate decision to fly an aircraft configuration highly sensitive to disturbances" [81, 82].

The main objectives of this research are to investigate the effects of different design parameters on aeroelastic stability of HALE aircraft and I seek to find the reason why certain configurations can extend the aeroelastic flight envelope and postpone the instabilities. Different design parameters such as engine/store location and wing shape and curvature will be considered, and the linear and nonlinear aeroelastic analyses will be performed.

Most of the studies on the effects of design parameters on aeroelastic stability take a descriptive approach, and they use the state-of-the-art numerical techniques to compare the performance of different designs and reveal the best of the options available. In the present study, I shed light on how a certain design parameter could influence the *flows* in the system, including the flow of stresses and how by morphing the geometry in the direction that provides greater access to the currents flowing through it leads to a better design. I also propose how the configuration should evolve towards a better design by facilitating the flow of stresses [46].

AEROELASTIC THEORY AND NUMERICAL PROCEDURE

2.1   Aeroelastic Theory

2.1.1   Structural theory: nonlinear composite beam theory
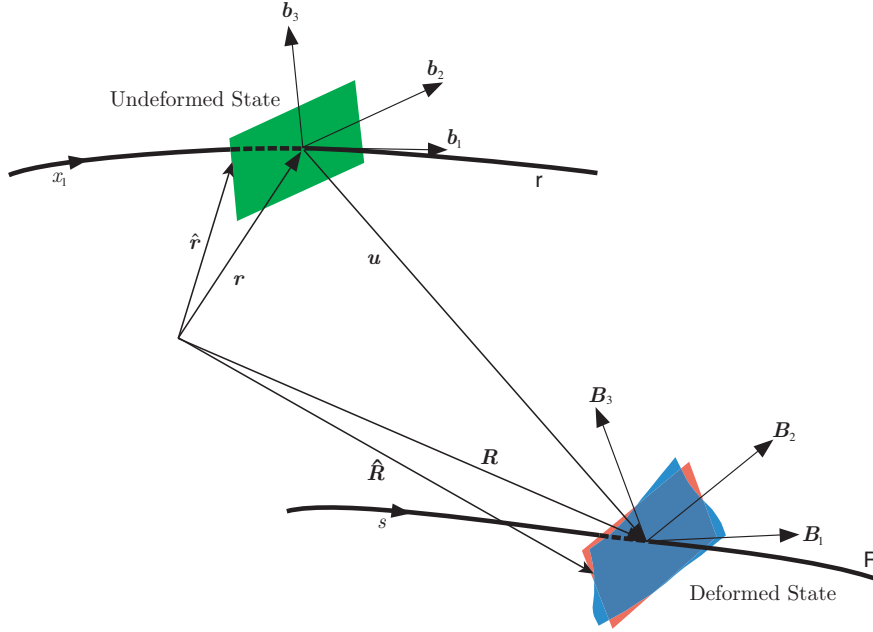
Figure 2.1: Sketch of beam kinematics [42]

The equations of motion which are presented in Eq. (2.1) are based on force, moment, angular velocity and velocity with nonlinearities of second order. These variables can be expressed in the bases of the deformed and undeformed frames, $B(x_1, t)$ and $b(x_1)$, respectively; see Fig. 2.1.

$$F'_B + \widetilde{K}_B F_B + f_B = \dot{P}_B + \widetilde{\Omega}_B P_B$$

$$M'_B + \widetilde{K}_B M_B + (\widetilde{e}_1 + \widetilde{\gamma}) F_B + m_B = \dot{H}_B + \widetilde{\Omega}_B H_B + \widetilde{V}_B P_B$$

(2.1)

In this set of equations, F_B and M_B represent the column matrices of cross-sectional stress and moment resultant; V_B and Ω_B define column matrices of cross-sectional

frame velocity and angular velocity; P_B and H_B indicate the column matrices of cross-sectional linear and angular momentum measures; $\widetilde{K}_B$ is Column matrix of deformed beam's curvature and twist. All of the aforementioned variables measure in $\mathbf{B}_i$ basis. The structural and the inertial constitutive equations relate the stress resultants and moments to the generalized strains and velocities as follow [42]:

$$
\left\{ \begin{array}{c} \gamma \\ \kappa \end{array} \right\} = \left[\begin{array}{cc} R & S \\ S^T & T \end{array} \right] \left\{ \begin{array}{c} F_B \\ M_B \end{array} \right\}
\tag{2.2}
$$

$$
\left\{ \begin{array}{c} P_B \\ H_B \end{array} \right\} = \left[\begin{array}{cc} \mu\Delta & -\mu\widetilde{\xi} \\ \mu\widetilde{\xi} & I \end{array} \right] \left\{ \begin{array}{c} V_B \\ \Omega_B \end{array} \right\}
\tag{2.3}
$$

Here, R, S, and T represent 3×3 partitions of the cross-sectional flexibility matrix; μ is the mass per unit length; Δ is the 3×3 identity matrix; I defines the 3×3 cross-sectional inertia matrix; ξ is $\lfloor 0 \quad \xi_2 \quad \xi_3 \rfloor^T$ in which ξ_2 and ξ_3 represent the position coordinates of the cross-sectional mass center with respect to the reference line. Finally, strain- and velocity-displacement equations are utilized to derive the intrinsic kinematical partial differential equations [42].

$$
V_B' + \widetilde{K}_B V_B + (\widetilde{e}_1 + \widetilde{\gamma})\Omega_B = \dot{\gamma}
$$
$$
\Omega_B' + \widetilde{K}_B \Omega_B = \dot{\kappa}
\tag{2.4}
$$

In these equations, the tilde $\widetilde{(\ )}$ represents the antisymmetric 3×3 matrix associated with the column matrix over which the tilde is placed; $\dot{(\ )}$ defines the partial derivative with respect to time; and $(\ )'$ is the partial derivative with respect to the axial coordinate, x_1. In order to solve these first-order, partial differential equations one may eliminate γ and κ using Eq. (2.2) and P_B and H_B using Eq. (2.3), and also 12 boundary conditions are required, in terms of force (F_B), moment (M_B), velocity (V_B) and angular velocity (Ω_B). Displacement and rotation variables do

not appear in this formulation, and singularities due to finite rotations are avoided. The position and the orientation can be obtained as post-processing operations by integrating,

$$r'_i = C^{ib}e_1$$
$$r_i + u'_i = C^{iB}(e_1 + \gamma)$$

(2.5)

and

$$(C^{bi})' = -\widetilde{k}C^{bi}$$
$$(C^{Bi})' = -(\widetilde{k} + \widetilde{\kappa})C^{Bi}$$

(2.6)

2.1.2 Aerodynamics theory: 2D induced flow theory of Peters

The aerodynamic model of Peters et al. [90] is utilized in this study. This finite-state model is a state-space, thin-airfoil, inviscid, incompressible approximation of an infinite-state representation of the aerodynamic loads. By using known airfoil parameters, it can consider induced flow in the wake and apparent mass effects. Additionally, It can accommodate large motion of the airfoil as well as the deflection of a small trailing-edge flap. Available studies in literature [90, 95] indicate that although this model cannot simulate the three-dimensional effects associated with the wingtip, it can accurately approximate the aerodynamic loads acting on high-aspect-ratio wings. The lift, drag and pitching moment at the quarter-chord are given by

$$L_{\text{aero}} = \rho b \left[(c_{l_0} + c_{l_\beta}\beta)V_T V_{a_2} - c_{l_\alpha}\dot{V}_{a_3}b/2 - c_{l_\alpha}V_{a_2}(V_{a_3} + \lambda_0 - \Omega_{a_1}b/2) - c_{d_0}V_T V_{a_3} \right]$$

(2.7)

$$D_{\text{aero}} = \rho b \left[-(c_{l_0} + c_{l_\beta}\beta)V_T V_{a_3} + c_{l_\alpha}(V_{a_3} + \lambda_0)^2 - c_{d_0}V_T V_{a_2} \right]$$

(2.8)

$$M_{\text{aero}} = 2\rho b \left[(c_{m_0} + c_{m_\beta}\beta)V_T - c_{m_\alpha}V_T V_{a_3} - bc_{l_\alpha}/8V_{a_2}\Omega_{a_1} - b^2 c_{l_\alpha}\dot{\Omega}_{a_1}/32 + bc_{l_\alpha}\dot{V}_{a_3}/8 \right]$$

$$(2.9)$$

Here,

$$V_T = (V_{a_2}^2 + V_{a_3}^2)^{1/2}. \tag{2.10}$$

$$\sin\alpha = \frac{-V_{a_3}}{V_T} \tag{2.11}$$

$$\alpha_{\text{rot}} = \frac{\Omega_{a_1} b/2}{V_T} \tag{2.12}$$

and β is the angle of flap deflection, V_{a_2} and V_{a_3} denote the measure numbers of V_a. The effect of unsteady wake (induced flow) and apparent mass included as λ_0 and acceleration terms in the force and moment equation, which λ_0 can be calculated using the induced flow model of Peters et al. [90]:

$$[A_{\text{induced flow}}]\{\dot{\lambda}\} + \left(\frac{V_T}{b}\right)\{\lambda\} = \left(-\dot{V}_{a_3} + \frac{b}{2}\dot{\Omega}_{a_1}\right)\{c_{\text{induced flow}}\} \tag{2.13}$$

$$\lambda_0 = \frac{1}{2}\{b_{\text{induced flow}}\}^T\{\lambda\} \tag{2.14}$$

Here λ defines the column matrix of induced flow states, and $[A_{\text{induced flow}}]$, $\{c_{\text{induced flow}}\}$, $\{b_{\text{induced flow}}\}$ represents constant matrices, which are derived in Ref. [90].

2.1.3   Gust airloads model

The gust airloads are taken into account separately from the aerodynamic forces of the flight dynamic velocities. The unsteady gust model measures the chordwise variation of the gust field on the deformed state of the wing. Here, an interpretation of the Peters and Johnson [89] theory that considers these effects is provided. The total induced flow is ω^B, defining the vertical gust velocity in the deformed beam frame.

$$\overline{L} = \omega_0 + \frac{1}{2}\omega_1 + \frac{1}{2}\left(\dot{\omega}_0 + \frac{1}{2}\dot{\omega}_1\right)\frac{b}{V_T} \qquad (2.15)$$

Here $\overline{L}$ denotes the velocity-normalized lift coefficient presented by Peters and Johnson [89]; ω_n is the coefficient of the nth Chebychev polynomial mode shape. ω^B can approximated as

$$\omega^B = \sum_0^N \omega_n T_n \qquad (2.16)$$

where T_n is the nth order Chebychev polynomial. The gust force can be provided as

$$f_{gust} = \left\{ \begin{array}{c} 0 \\ -\rho b C_{l\alpha}\left(V_3 + \omega_0\right)\overline{L} \\ \rho b C_{l\alpha} V_2 \overline{L} \end{array} \right\} \qquad (2.17)$$

and the gust contribution to the induced flow can be presented as

$$\lambda_{0_{gust}} = \dot{\omega}_0 + \frac{1}{2}\dot{\omega}_1 \qquad (2.18)$$

2.2 Nonlinear Aeroelastic Trim And Stability of HALE Aircraft (NATASHA)

NATASHA [21, 86] is a powerful code for determining the aeroelastic behavior of HALE aircraft. The aeroelastic system is constructed by unifying the aerodynamic equations with the structural equations.

$$[A]\{\dot{x}\} + \{B(x)\} = \{f_{cont}\} \qquad (2.19)$$

Here, $\{x\}$ and $\{f_{cont}\}$ define the vectors of all of the aeroelastic variables and the flight controls, respectively. The resulting nonlinear ordinary differential equations are then linearized about a static equilibrium state, which is obtained by nonlinear algebraic equations. Utilizing the Newton-Raphson procedure, NATASHA solves these equations to obtain the steady-state trim solution [86]. The stability of the structure can be analyzed by linearizing this system of nonlinear aeroelastic equations about the resulting trim state, which leads to a standard eigenvalue problem. The linearized system is represented as

$$[A]\left\{\dot{\hat{x}}\right\} + [B]\left\{\hat{x}\right\} = \left\{\hat{f}_{cont}\right\} \tag{2.20}$$

where $\hat{()}$ is the perturbation about the steady-state values.

The trim equations are available in the study by Patil et al. [86]. They mentioned that the trim conditions are the same as steady-state conditions, which all the time-derivatives are zero. The symmetric trim equations are

$$\hat{g}_2\hat{V}_2 + \hat{g}_3\hat{V}_3 - \tan\phi\left(\hat{g}_3\hat{V}_2 - \hat{g}_2\hat{V}_3\right) = 0 \tag{2.21}$$

$$\hat{V}_2^2 + \hat{V}_3^2 - \hat{V}_\infty^2 = 0 \tag{2.22}$$

where ϕ and V_∞ are the prescribed flight angle and airspeed, respectively.

NATASHA is verified and validated [62, 95], specifically, for the effects of sweep on the flutter and divergence, its results have been verified [62] against the classical cantilever wing model of Goland and Luke [35]. There are various studies available in the literature that present the system of the equations and the methods of solution of NATASHA [86, 21]. Additionally, Chang and Hodges [20] used the geometrically exact fully intrinsic beam formulation to study the vibration characteristics of curved

13

beams. They compared their results with available data in the literature for the cases of in-plane and out-of-plane vibration and validated the beam formulation for the case of curved beams. This formulation is the same formation behind NATASHA's structural part.

2.3   Variational Asymptotic Beam Sectional Analysis (VABS)

VABS [106, 107, 109] is commercial software that uses the variational method to simplify a three-dimensional nonlinear analysis. It projects a three-dimensional slender structures to a two-dimensional cross-sectional and one-dimensional beam analysis. VABS decreases the analysis time from hours to seconds while maintaining the accuracy of detailed 3D FEA. It uses a finite element mesh of the cross-section and material properties as inputs to calculate the cross-sectional properties (e.g., structural properties and inertial properties). It also performs stress recovery uses inputs such as axial and shear forces, moments, distributed forces, and moments including applied and inertial [46].

2.4   Stress Recovery Procedure

Three different computer programs Gmsh [34], VABS [106, 107, 109], and NATASHA [86, 21] are used in this study as well as several functions that are developed in MATLAB to connect these software packages and also perform the post-processing of stresses [46].

The geometries of the cross-section of wings and fuselage are produced and meshed in the open-source software, Gmsh [34]. Gmsh uses the finite element method to create the mesh. It has four different modules for creating geometry,

14

mesh, solving, and post-processing. I only used the geometry and mesh modules of Gmsh to create and mesh the cross-sectional geometry of the aircraft. I imported these geometries and meshes, along with the material properties, into the VABS software to obtain the cross-sectional and elemental properties of different parts of the aircraft. It is noteworthy that the curvature should be implemented in VABS to achieve the corrected cross-sectional properties because the initial twist and curvature of the geometry introduce some elastic couplings [46, 108].

In the next step, the values of cross-sectional and elemental properties are used in NATASHA to perform stability analysis. Finally, the trim state results calculated in NATASHA are returned to the VABS software to acquire the stresses through the structure. The stresses are post-processed using an in–house program written in MATLAB [46]. A schematic view of the steps of this research is presented in Fig. 2.2.
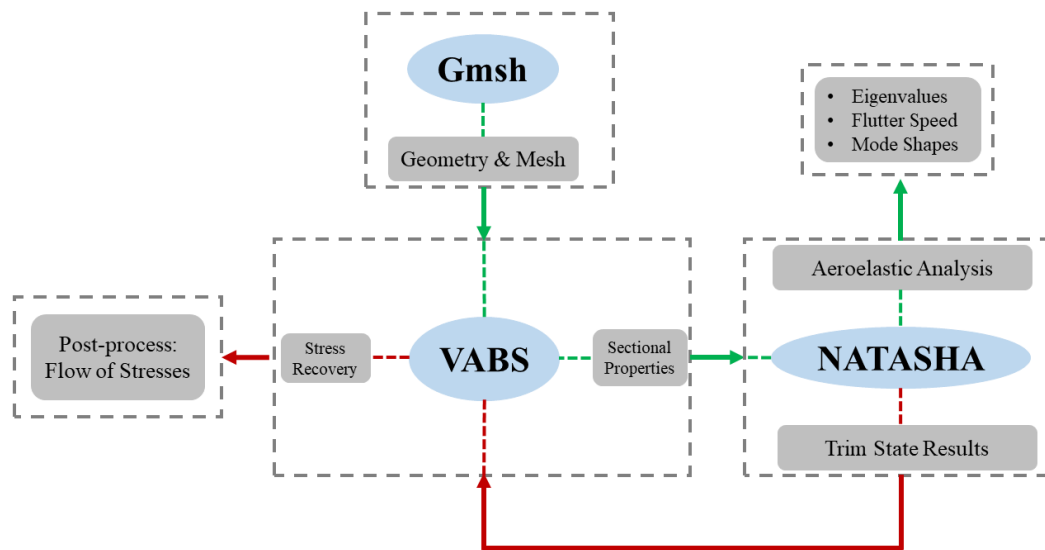
Figure 2.2: Schematic view of the study procedure.

CHAPTER 3

FLUTTER SUPPRESSION WITH DESIGN PARAMETERS

3.1 Background

Several approaches have been taken to solve the problem of aircraft flutter. These include modifying the structure, adding mass balance, imposing flight restrictions and the use of active flutter suppression systems [1, 52, 91], each having its limitations [44, 91].

Several researches show that engine or store location can greatly affect the flutter boundary [27, 29, 74, 97]. An experimental and theoretical investigation by Tang et al. [97] showed that the store could increase the flutter speed significantly by placing the store at 50% of the span. Studies [62, 68] showed that the location of the engines on a flying wing leads to flutter suppression. They reported that engine placement at 60% of the span forward of the reference line increases the flutter speed significantly (about two times of their base model).

Sweep is another design parameter that can significantly enhance the flutter characteristics of the flying wing aircraft. Swept wing configuration is a common aircraft design practice, which was used as early as the 1950s in the design of airplanes and fighters such as MiG-15 and F-86 Sabre. The effect of sweep angle on the aerodynamic and stability of an aircraft has been comprehensively discussed in the literature [4, 26, 37, 39, 47, 59, 60, 71, 77]. Several experimental and theoretical investigations suggested that generally, sweep angle increases the flutter speed of the wing [4, 47, 59, 71]. Different wings with various geometries and materials have been investigated in these studies, and their results suggested that an increase in sweep extends the stability boundaries. Mardanpour et al. [62] studied the effect

of sweep on the nonlinear aeroelastic characteristic of flying wing aircraft. Their results show that both aft and forward sweep increases the flutter speed [46].

The curved wing geometry is a common shape in marine animals such as swordfish and tuna [100] or birds such as swift [51, 100]. There are variety of curved wings proposed and investigated in the literature, including crescent-moon-shaped wings [100], gull wings [102], curved wing with curvature in chordwise direction [22, 23, 24, 32, 80, 94], curved wings with curvature in spanwise direction [80, 94], wings with curved leading edge [17, 25, 49], and inflected wings [80].

Most of the studies on curved wings only consider the aerodynamic changes of adding curvature to the wing, while the stability was not taken into account. Chiarelli et al. [22, 24] studied the flutter characteristics of the chordwise curved wing in comparison with a swept wing configuration. Their investigation reports that the flutter speed of the curved wing is higher than the swept wing configuration. However, in their model, the tip of the curved wing is behind the tip of the swept model. This means that the component of the airflow (i.e., lift force) acting on the swept structure is larger. A better comparison of the flutter boundary of these geometries calls to the same externally applied load, i.e., aerodynamic load. This could be attained if the tips of the wings are positioned at the same location [46].

Changing the design parameters of the aircraft can significantly affect flutter. This chapter presents the effects of these parameters on the flutter characteristics of very flexible flying wings aircraft and cantilevered wing. In this chapter, the effects of engine placement and armament placement on the flutter characteristics of the cantilevered wing configurations are presented. Additionally, the effects of engine placement, sweep, and curvature on the flutter characteristics of the flying wing aircraft models.

3.2 Engine Placement Effects on Flutter Characteristics of High-Aspect-Ratio Wings

In this section, the effects of engine placement on the flutter behavior of a very flexible high-aspect-ratio wing is presented. Flutter speed and frequency contours are presented for engine placement along the span and in $\mathbf{b}_2$ and $\mathbf{b}_3$ directions. Results for engine placement between 60% to 80% of span with offsets from the reference line show a significant increase in flutter speed. Fig. 3.1 shows the schematic view of this wing carrying an engine. As shown in Fig. 3.1, η is the dimensionless length in the $\mathbf{b}_1$ direction, along which the engine is located.
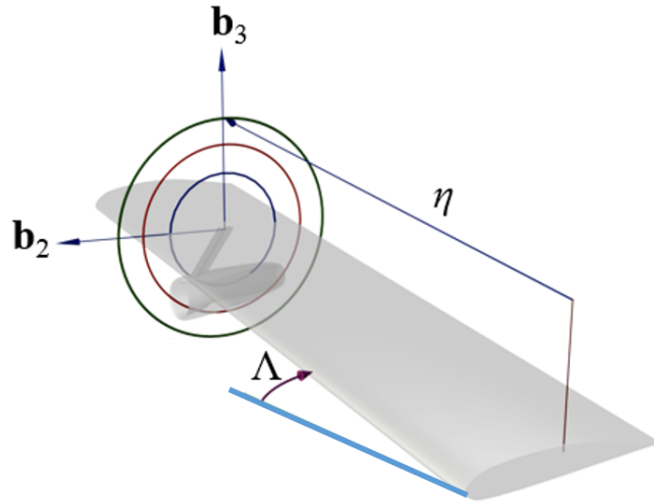
Figure 3.1: Schematic 3D view of a very flexible high-aspect-ratio.

3.2.1 Properties and dimensions of the model

The properties of the cantilever wing are presented in Table 3.1. The wing is aft swept 15°, and modeled using 20 elements. For the base model of the present study, a wing is considered in the absence of an engine. The real and imaginary parts of

the eigenvalues for the clean wing is shown in Fig. 3.2 and Fig. 3.3. The clean wing

flutters at the speed of 32.9 m/s and frequency of 22.47 rad/s [65].

Span	16
Aft sweep angle	15
Number of elements	20
Torsional stiffness	10^4
Out-of-plane bending stiffness	2×10^4
In-plane bending stiffness	4×10^6
Mass per element	0.75
Mass polar moment of inertia per element	0.1
Chord, c	1
Offset of aerodynamic center from elastic axis, e	0.25
Lift-curve slope, $c_{l\alpha}$	2π
Drag coefficient, c_{d_0}	0.01
Gravity, g	9.8
Air density, ρ	0.0889

Table 3.1: Wing properties (SI units) [65].

Figure 3.2: Normalized real part of eigenvalues versus normalized speed of clear wing [65].

19

Figure 3.3: Normalized imaginary part of eigenvalues versus normalized speed of clear wing [65].

3.2.2 Flutter analysis

The results of different engine placement on the flutter speed and flutter frequency are presented in Figs. 3.4– 3.7. The engine is mounted in the x_1/l and x_2/b plane as well as in the x_1/l and x_3/b plane. It should be noted that the effect of the engine's mount flexibility is not taken into account. These results are normalized with the flutter speed and frequency of the clean wing.

Figure 3.4 shows the results of the flutter speed in the x_1/l and x_2/b plane. The results indicate a significant increase in the flutter speed between 60% to 80% of the span forward of the elastic axis. The same conclusion was previously reported by Madranpour et al. [63] for wing without sweep, which they reported a substantial increase in the flutter speed between 70 to 95 percent of the span. Additionally, as the engine moves toward the tip of the wing, flutter speed decreases. Apparently, for the engine placement behind the reference line, in the area between 60 and 80

percent of the span, the flutter speed reduces. This drop reported by Madranpour et al.[63] at 35% to 55% of span behind the reference line.

Figure 3.5 illustrates the flutter frequency in the x_1/l and x_2/b plane. The flutter frequency decreases as the engine moves toward the tip of the wing. However, at the tip of the wing and behind the reference line, a significant increase in the flutter frequency is observed.

The contour of flutter speed in the x_1/l and x_3/b plane is shown in the Fig. 3.6. In this plane, the flutter speed increases and decreases at the tip of the wing below and above the reference line, respectively.

The contour of flutter frequency in the x_1/l and x_3/b plane is also presented in Fig. 3.7. It is observed that as the engine moves toward the tip of the wing, the flutter frequency reduces. There is only a small area at approximately 95 percent of the span and below the reference line in which the flutter frequency increases.
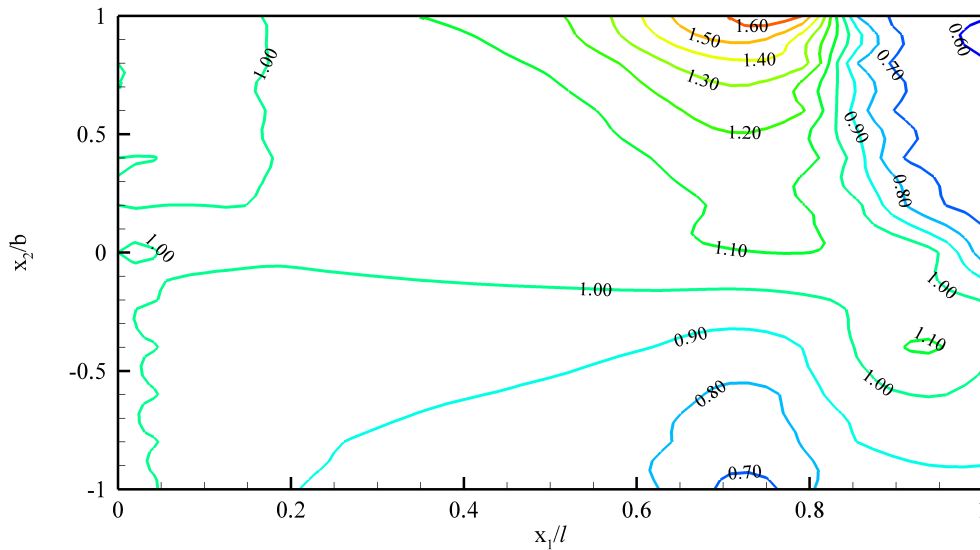
Figure 3.4: Contour of normalized flutter speed for engine placement in chord wise direction, i.e. $\mathbf{b}_2$ [65].
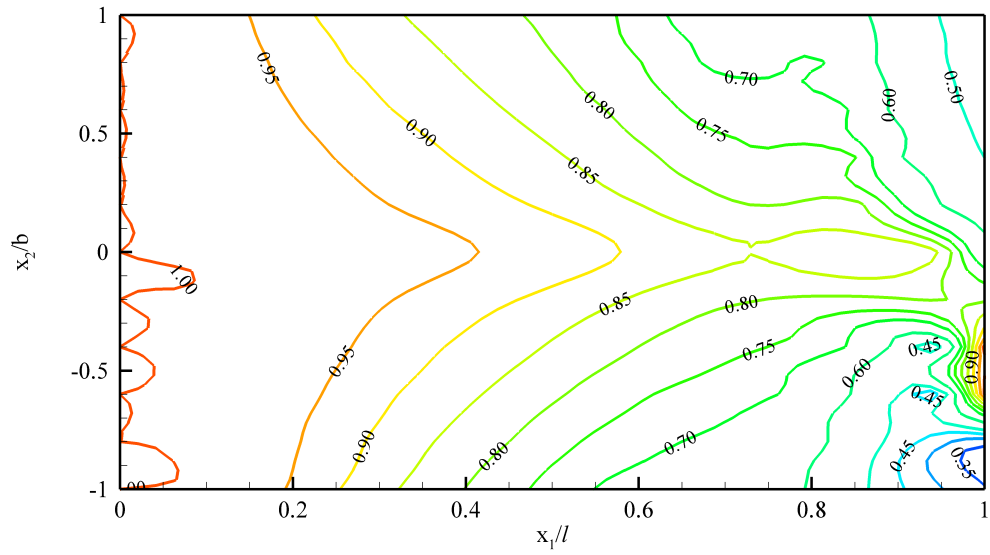
Figure 3.5: Contour of normalized flutter frequency for engine placement in chord wise direction, i.e. $\mathbf{b}_2$ [65].
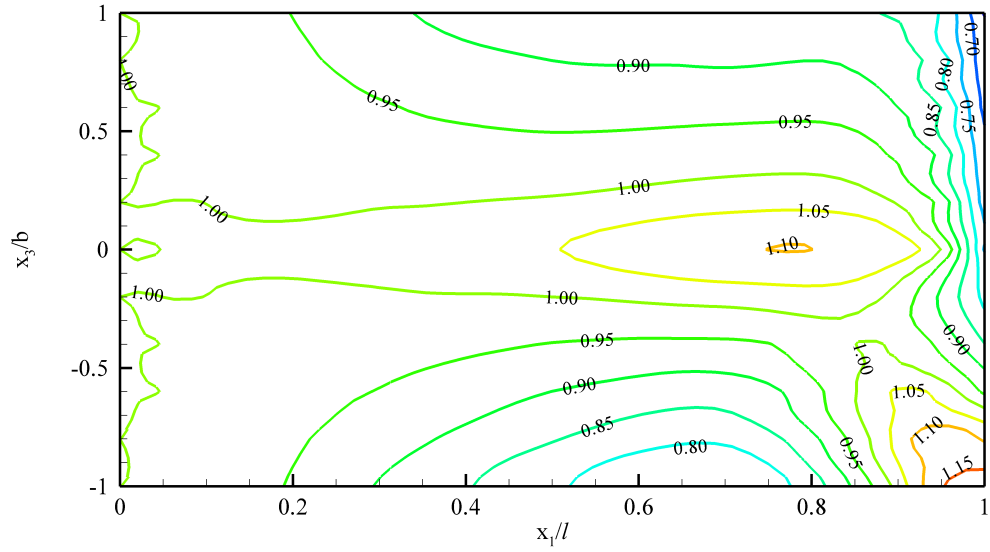
Figure 3.6: Contour of normalized flutter speed for engine placement in normal direction, i.e. $\mathbf{b}_3$ [65].
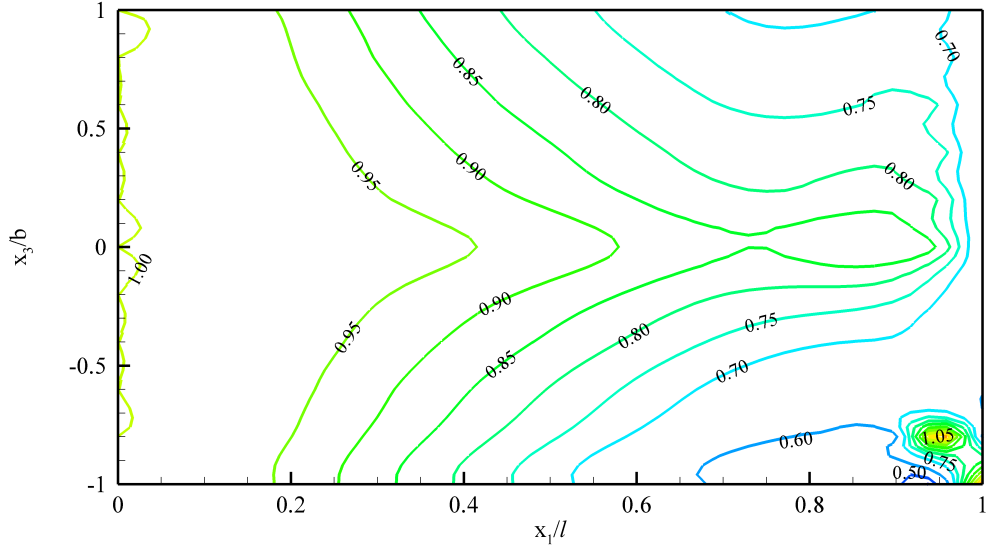
Figure 3.7: Contour of normalized flutter frequency for engine placement in normal direction, i.e. $\mathbf{b}_3$ [65].

3.3 Effect of Armament Placement on Flutter Behavior of a High-Aspect-Ratio Wing

This section discusses the effects of armament placement on the flutter behavior of high-aspect-ratio wing. Flutter speed and frequency contours are presented for armament placement in the span-wise direction and in $\mathbf{b}_2$ and $\mathbf{b}_3$ directions. The armament placement forward of the reference line increases the flutter speed. The schematic view of the wing with armament attached to it can be seen in Fig. 3.8.

3.3.1 Properties and dimensions of the model

The wing model used for the case study resembles a cantilever beam having a span of 18 meters and consisting of 20 elements, with 0 degree sweep angle $\Lambda = 0$. Table

3.2 represents the properties that have been used for modeling of the wing and armament in NATASHA. The base model is a clean wing without any concentrated mass attached to it [64].

Property	Value
Span $[m]$	18
Number of elements	20
Sweep angle $[degrees]$	0
$\mathbf{R}\ [N^{-1}]$	$\begin{bmatrix} 4.512 \times 10^{-8} & 0 & 0 \\ 0 & 1.742 \times 10^{-7} & 3.885 \times 10^{-12} \\ 0 & 3.885 \times 10^{-12} & 5.899 \times 10^{-6} \end{bmatrix}$
$\mathbf{S}\ [N^{-1}.m^{-1}]$	$\begin{bmatrix} 0 & 1.262 \times 10^{-11} & 3.752 \times 10^{-10} \\ -1.446 \times 10^{-11} & 0 & 0 \\ -5.094 \times 10^{-6} & 0 & 0 \end{bmatrix}$
$\mathbf{T}\ [N^{-1}.m^{-2}]$	$\begin{bmatrix} 2.147 \times 10^{-5} & 0 & 0 \\ 0 & 2.733 \times 10^{-5} & 9.218 \times 10^{-13} \\ 0 & 9.218 \times 10^{-13} & 4.162 \times 10^{-7} \end{bmatrix}$
$\mathbf{I}\ [kg.m]$	$\begin{bmatrix} 9.684 \times 10^{-2} & 0 & 0 \\ 0 & 1.453 \times 10^{-3} & -2.851 \times 10^{-9} \\ 0 & -2.851 \times 10^{-9} & 9.539 \times 10^{-2} \end{bmatrix}$
$\boldsymbol{\xi}\ [m]$	$\begin{bmatrix} 0 \\ 9.015 \times 10^{-4} \\ -4.618 \times 10^{-7} \end{bmatrix}$
Mass per unit length $[kg.m^{-1}]$	0.88
Chord, c $[m]$	1
Offset of aerodynamic center from reference line, e $[m]$	0.25
c_{l_α}	2π
c_{d_0}	0.01
c_{m_α}	-0.08
Gravity, $g\ [m.s^{-2}]$	9.8
Air Density, $\rho\ [kg.m^{-3}]$	0.0889
Armament mass $[kg]$	10.0
$\mathbf{I}_{Armament}\ [kg.m]$	$\begin{bmatrix} 1.28 \times 10^{-1} & 0 & 0 \\ 0 & 3.44 \times 10^{-2} & 0 \\ 0 & 0 & 1.28 \times 10^{-1} \end{bmatrix}$
Bullet mass $[kg]$	1.0

Table 3.2: Properties of wing, armament and bullet in SI units [64].
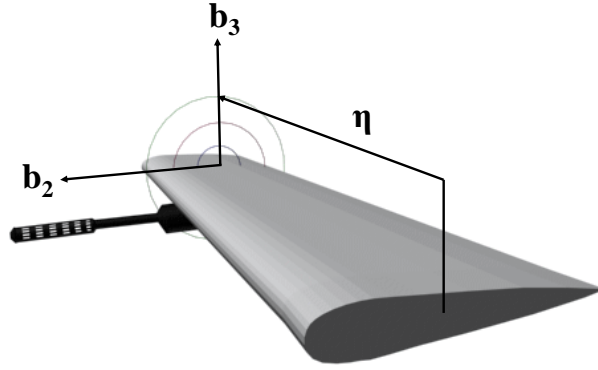
Figure 3.8: Schematic 3D view of a very flexible high-aspect-ratio wing [64].

The base model (i.e., clean wing) was seen to flutter at a speed of 34.8 m/s with a frequency of 15.7 rad/s. The base model's speed and frequency are used for normalization of the flutter speed and the eigenvalues. Figs. 3.9 and 3.10 represent the behavior of the eigenvalues for the base model. Fig. 3.9 indicates the behavior of the real part of eigenvalues, and Fig. 3.10 suggests the behavior of the imaginary part of the eigenvalues. The unstable mode is the first bending-torsion mode [64].
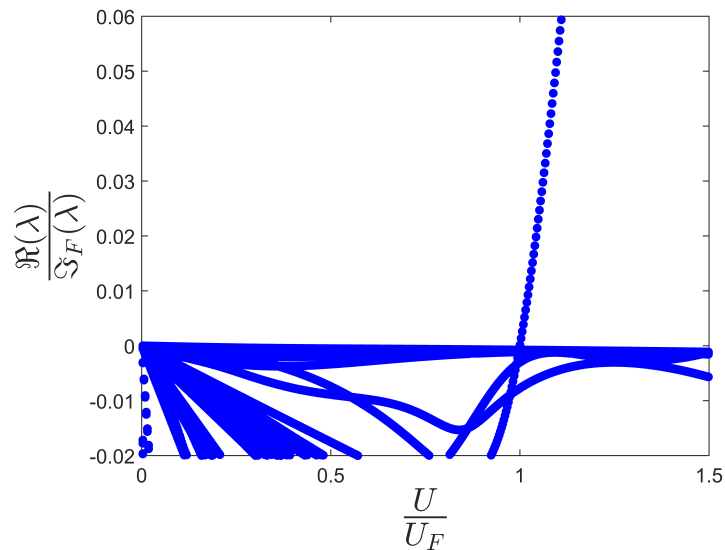

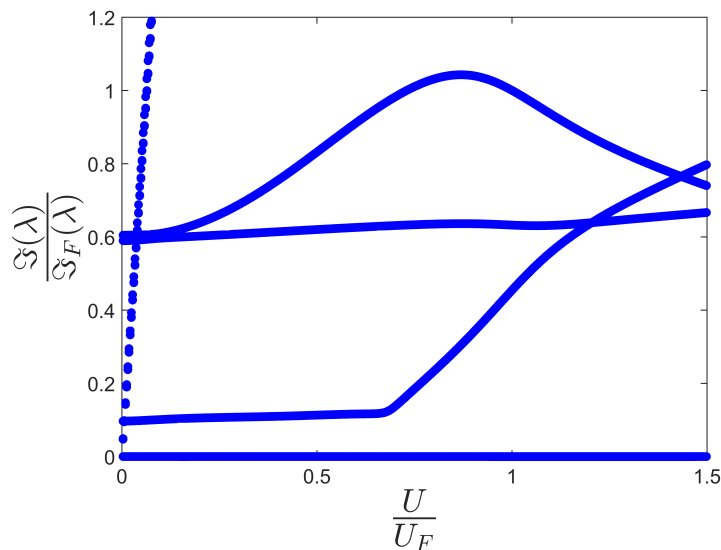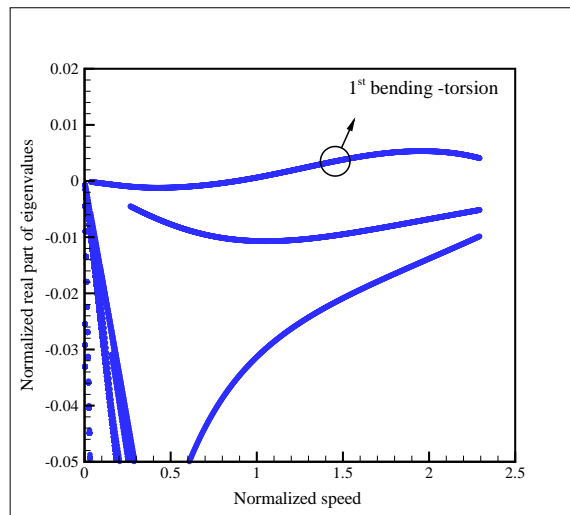Figure 3.9: Normalized real part of eigenvalues versus normalized speed of clean wing [64].
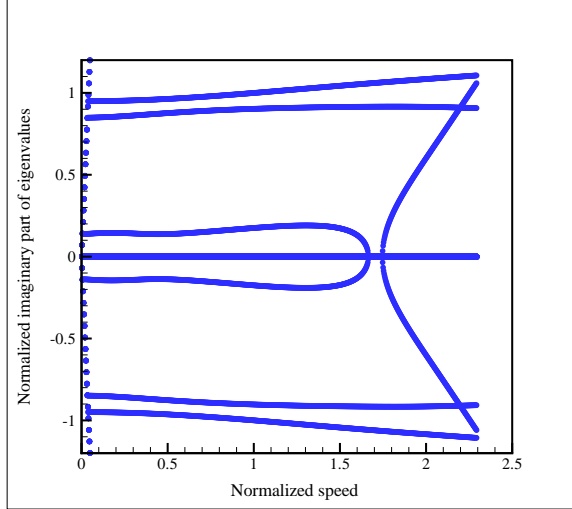
Figure 3.10: Normalized imaginary part of eigenvalues versus normalized speed of clean wing [64].

3.3.2 Flutter analysis

The results of flutter speed and frequency contours for different locations of the gun placement along the chordwise and in the normal direction are presented in this section. The gun is mounted in the b_1, b_2 plane as well as in the b_1, b_3 plane. It should be mentioned that the effect of the gun mount flexibility has not been taken into account.

Figure 3.11 shows the results of the flutter speed in the b_1 and b_2 plane. It is found that the flutter speed increases substantially when the gun is placed forward of the reference line. On the other hand, when the gun is placed behind the reference line at about 65% to 95% of the span, the flutter speed significantly decreases. Fig. 3.12 indicates the variations of flutter frequency in the b_1 and b_2 plane. The frequency decreases as the gun position moves towards the tip of the wing, but it significantly increases when the gun is placed at the tip [64].
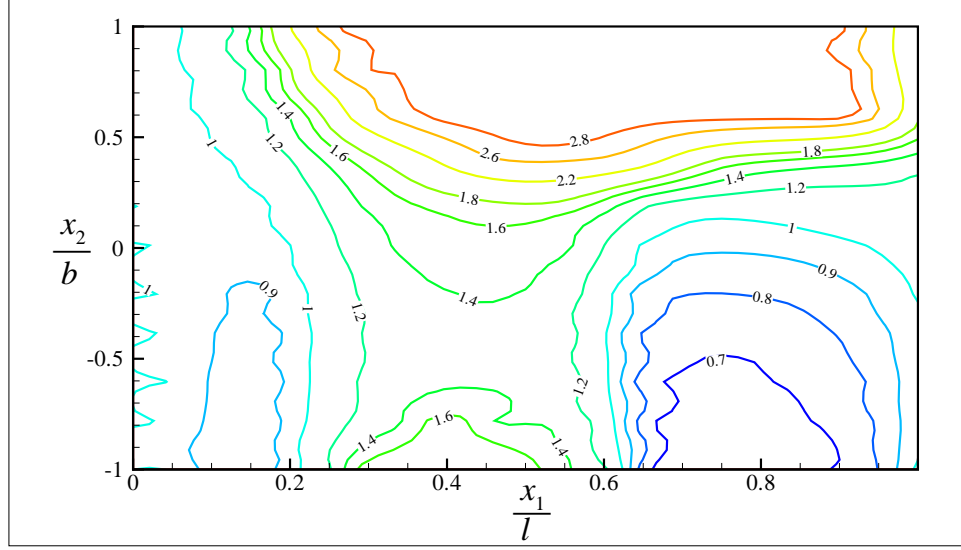
Figure 3.11: Contour of normalized flutter speed for gun placement in chord wise direction i.e. b_2; considering effects of gravity [64].
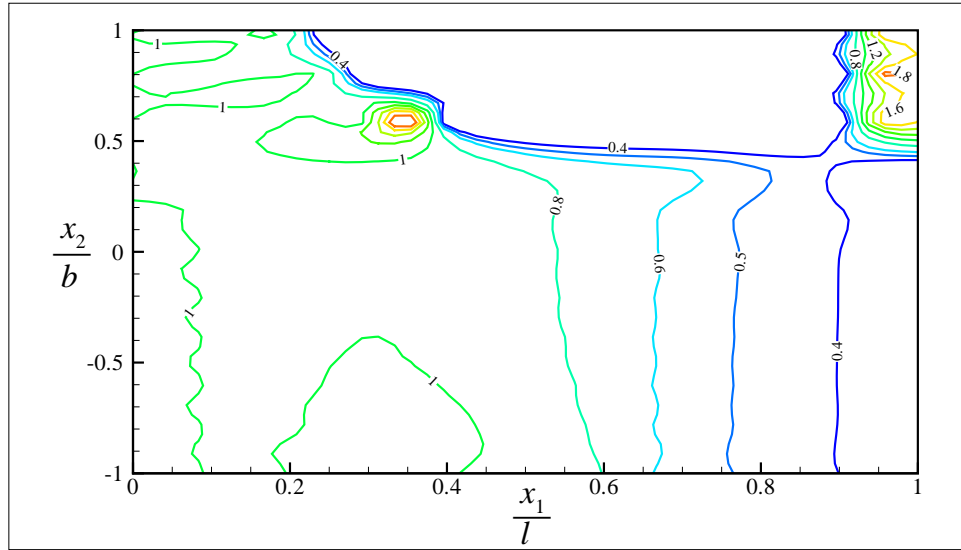
Figure 3.12: Contour of normalized flutter frequency for gun placement in chord wise direction i.e. b_2; considering effects of gravity [64].

The results for the flutter speed when the gun is placed in the $\boldsymbol{b}_1$ and $\boldsymbol{b}_3$ plane is illustrated in Fig. 3.13. It is found that when the gun is placed close to 50% of span, just above the reference line, flutter speed increases. Fig. 3.14 represents

flutter frequency in the b_1 and b_3 plane. It is observed that the frequency decreases as the gun is moved away from the root. Additionally, an increase in the frequency is observed at 50% of span above the reference line [64].
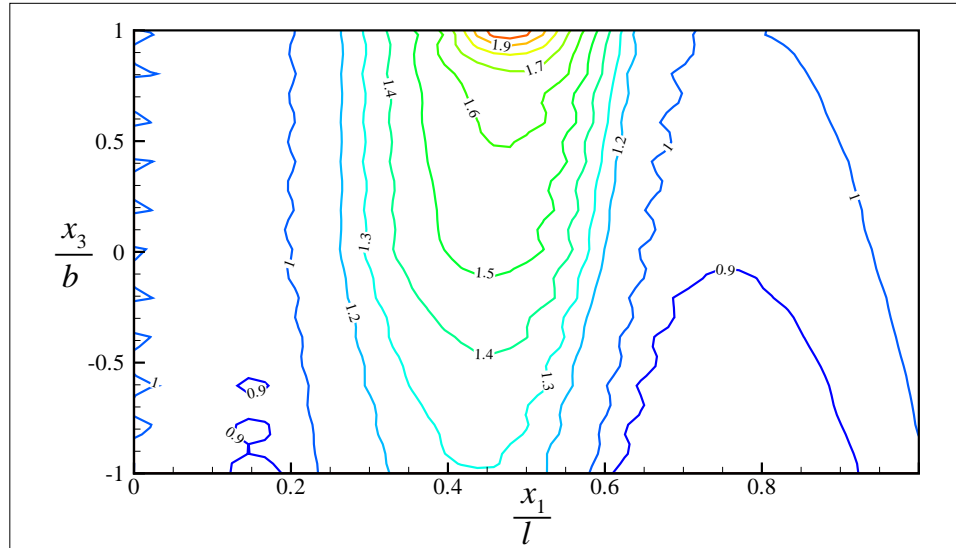
Figure 3.13: Contour of normalized flutter speed for gun placement in normal direction i.e. b_3; considering effects of gravity [64].
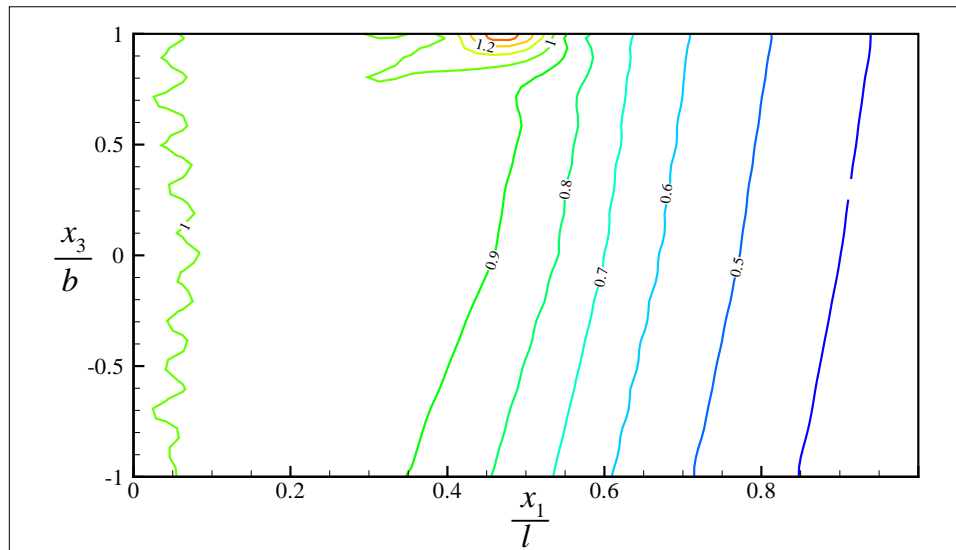
Figure 3.14: Contour of normalized flutter frequency for gun placement in normal direction i.e. b_3; considering effects of gravity [64].

3.4 Effects of Engine Placement on Flutter Characteristics of Flying Wing Aircraft

In section 3.2, the effects of engine placement on the flutter characteristics of a cantilevered wing is discussed. Here, the effects of engine placement on the flutter behavior of a flying wing aircraft are presented. Flutter speed and frequency contours are provided for engine placement along the span and in $\mathbf{b}_2$ and $\mathbf{b}_3$ directions. Results indicate an increase in flutter speed when the engine is mounted close to 80% of span with offsets from the reference line.

3.4.1 Properties and dimensions of the model

A flying wing aircraft is designed with two wings of length 16 m each and a fuselage of 3.2 m. Aluminum is the material used to design the wings, and the airfoil is NACA 0012. The wings are simulated using 20 elements, and the fuselage contains four elements. The fuselage is considered as a rigid body, and the wings are flexible [67]. Figure 3.15 shows the designed aircraft for this investigation. The properties of the wings and the aerodynamic coefficients are presented in Tables 3.3 and 3.4.
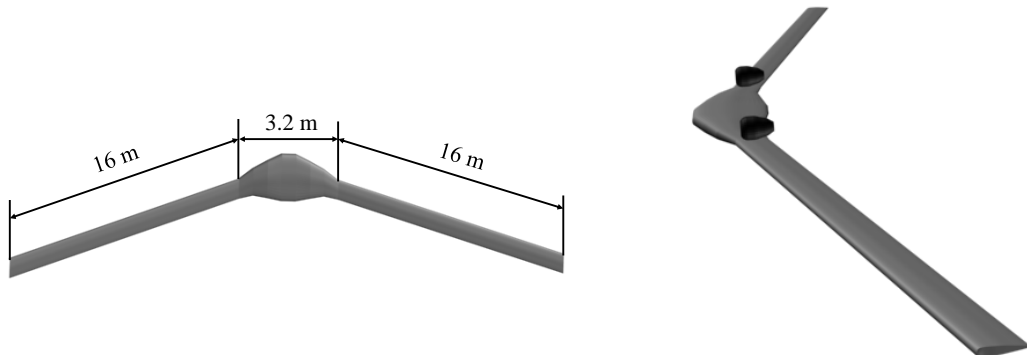
Figure 3.15: The dimensional geometry of flying wing aircraft [67].

Property	Value
Span $[m]$	16
Number of elements	20
Sweep angle $[degrees]$	15
R $[N^{-1}]$	$\begin{bmatrix} 9.06 \times 10^{-9} & 0 & 0 \\ 0 & 3.50 \times 10^{-8} & 7.22 \times 10^{-13} \\ 0 & 7.22 \times 10^{-13} & 1.18 \times 10^{-6} \end{bmatrix}$
S $[N^{-1}.m^{-1}]$	$\begin{bmatrix} 0 & 2.63 \times 10^{-12} & 7.57 \times 10^{-11} \\ -3.01 \times 10^{-12} & 0 & 0 \\ -1.02 \times 10^{-6} & 0 & 0 \end{bmatrix}$
T $[N^{-1}.m^{-2}]$	$\begin{bmatrix} 4.33 \times 10^{-6} & 0 & 0 \\ 0 & 5.53 \times 10^{-6} & 2.42 \times 10^{-14} \\ 0 & 2.42 \times 10^{-14} & 8.43 \times 10^{-8} \end{bmatrix}$
I $[kg.m]$	$\begin{bmatrix} 4.78 \times 10^{-1} & 0 & 0 \\ 0 & 7.2 \times 10^{-3} & -1.04 \times 10^{-10} \\ 0 & -1.04 \times 10^{-10} & 4.71 \times 10^{-1} \end{bmatrix}$
ξ $[m]$	$\begin{bmatrix} 0 \\ 8.98 \times 10^{-4} \\ -4.76 \times 10^{-7} \end{bmatrix}$
Mass per unit length $[kg.m^{-1}]$	4.38
Chord, c $[m]$	1

Table 3.3: Properties of the wing [67].

Property	Value
Offset of aerodynamic center from reference line, e $[m]$	0.125
c_{l_α}	2π
c_{l_δ}	1
c_{d_0}	0.02
c_{m_0}	-0.0005
c_{m_α}	-0.01
c_{m_δ}	-0.25
Gravity $[m.s^{-2}]$, g	9.8
Air density $[kg.m^{-3}]$, ρ	0.0889

Table 3.4: Aerodynamic properties and coefficients [67].

3.4.2 Flutter analysis

The flying wing is seen to flutter at 34.5 m/s and at a frequency of 6.9 rad/s when the engines are located at the root of the wing. This configuration is considered as the base model. The engines masses for all of the analysis is constant and equal to 10 kg for each engine. The unstable mode shape of the base model is shown in Fig. 3.16. The unstable mode contains first and second bending modes [67].
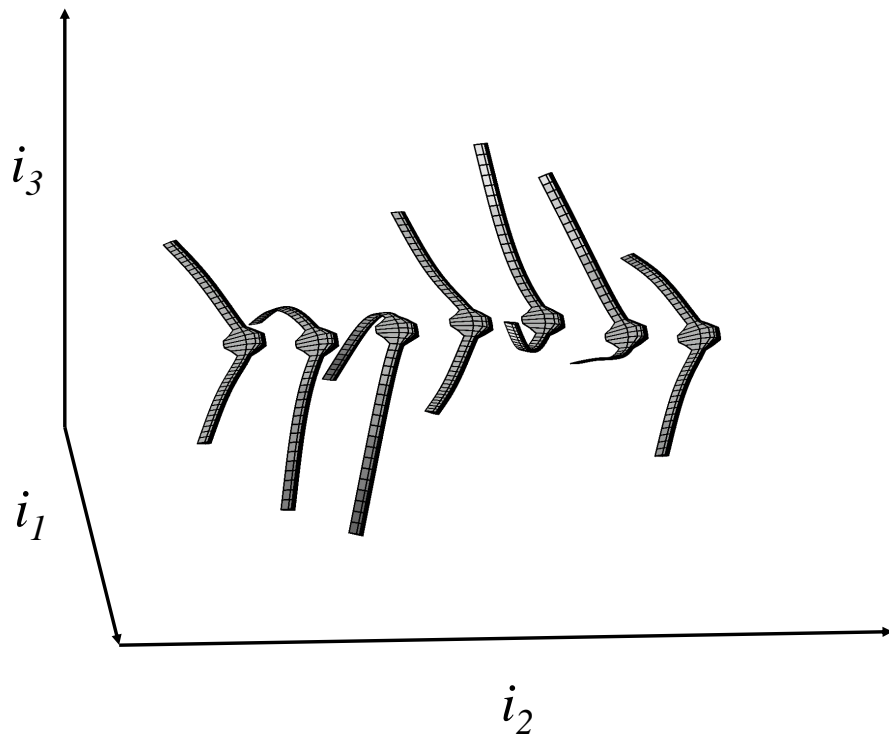
Figure 3.16: The unstable symmetric free-free mode shape of the flying wing [67].

The flutter results are normalized with flutter speed and flutter frequency of the base model. The results of flutter speed and frequency contours for different locations of the engine placement along the chordwise and in the normal direction are presented in this section. The engine is mounted in the b_1, b_2 plane as well as in the b_1, b_3 plane. The results have been obtained by increasing the speed step by

step. NATASHA trims the aircraft for the equality of drag to thrust and weight to lift. Consequently, higher speed requires higher thrust [67].

Figures 3.17 and 3.18 illustrate the results of the flutter speed and flutter frequency in the b_1 and b_2 plane. It is observed that the flutter speed increases considerably when the engine is mounted forward of the reference line, close to 80% of the span. On the other hand, when the engine is placed behind the elastic axis between 0 and 40% of the span, the flutter speed decreases substantially. The results for the flutter speed and flutter frequency when the engine is mounted in the b_1 and b_3 plane are illustrated in Figs. 3.19 and 3.20, respectively. It is found that as the location of the engine changes, the flutter speed varies significantly. The results for both flutter speed and frequency are almost symmetric for the engine placements above and below the reference line [67].
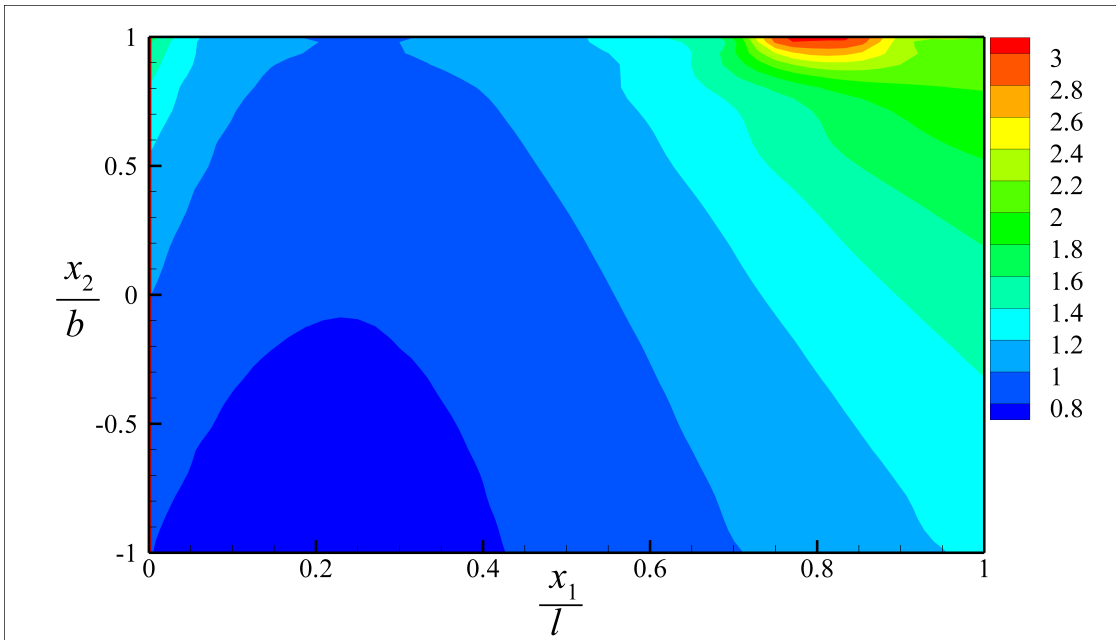
Figure 3.17: Contour of normalized flutter speed for engine placement in chord wise direction, b_2 [67].
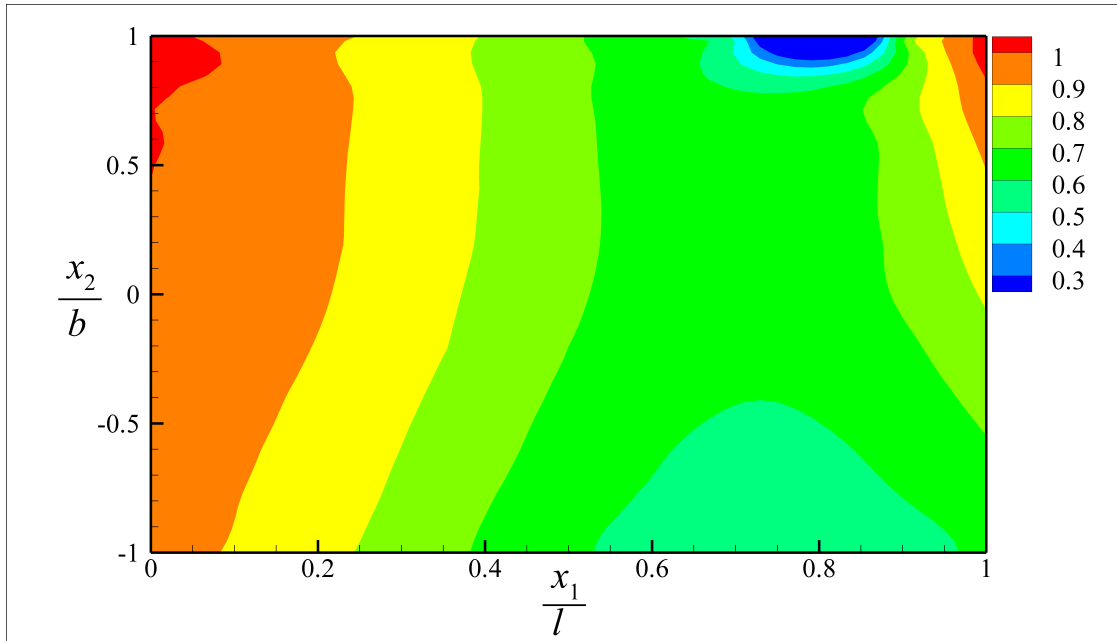
Figure 3.18: Contour of normalized flutter frequency for engine placement in chord wise direction, b_2 [67].
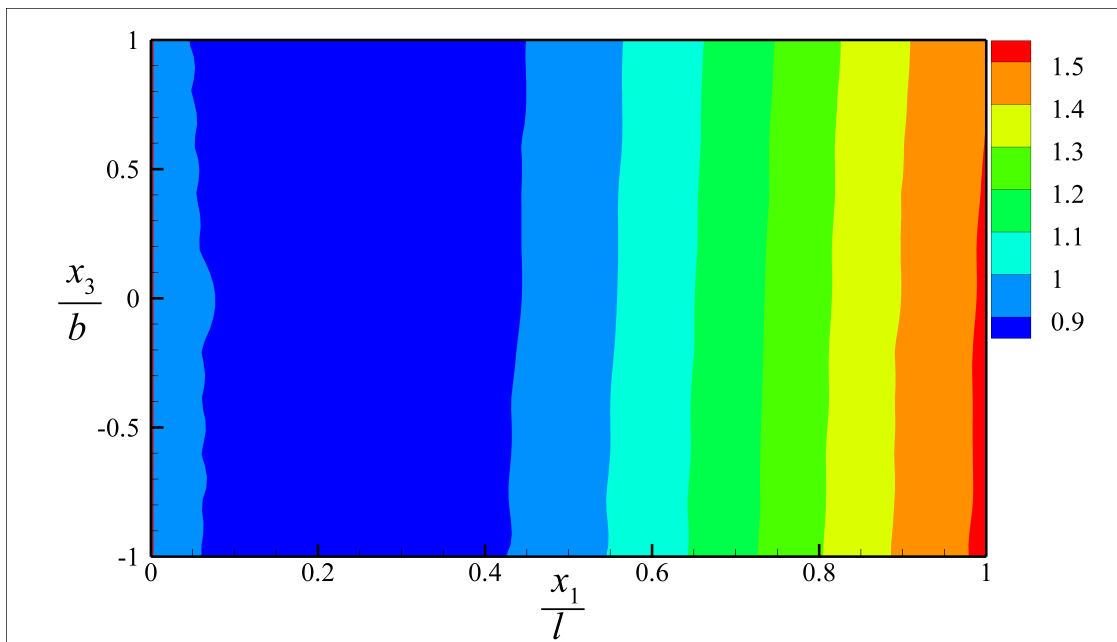
Figure 3.19: Contour of normalized flutter speed for engine placement in normal direction, b_3 [67].
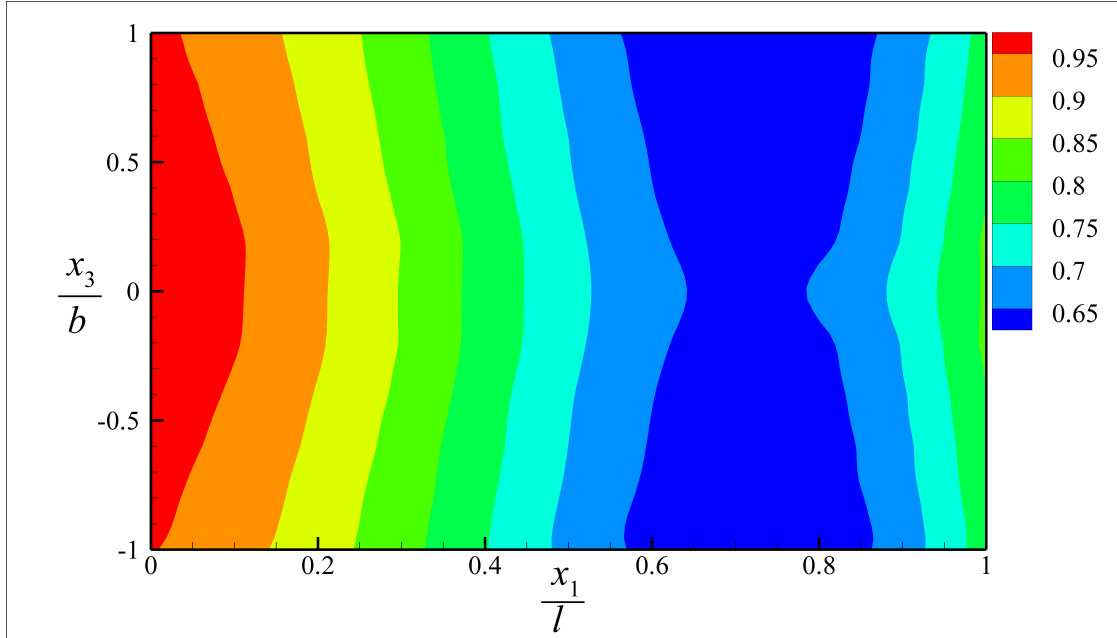
Figure 3.20: Contour of normalized flutter frequency for engine placement in normal direction, b_3 [67].

3.5 Effects of Sweep and Curvature on Flutter Characteristics of Flying Wing Aircraft

In this section, I compare two different flying wing aircraft with curved and swept wings. Three degrees of sweep and curvature are examined, and the results of the eigenvalue analysis of these configurations and their flutter characteristics are presented and compared.

3.5.1 Properties and dimensions of the model

The details of the geometry and the dimensions of the designed aircraft are presented in Fig. 3.21. The cross-section layout and the location of the reference point of the airfoil are presented in Fig. 3.22. Moreover, different views of the swept and

curved wing aircraft are presented in Figs. 3.23 and 3.24, respectively. The swept model in these figures has 15–degrees backward sweep and the curved model has 30–degrees curvature. Although the angles are different, the tips of the wings of these configurations are located at the same position (see Fig. 3.21) [46].
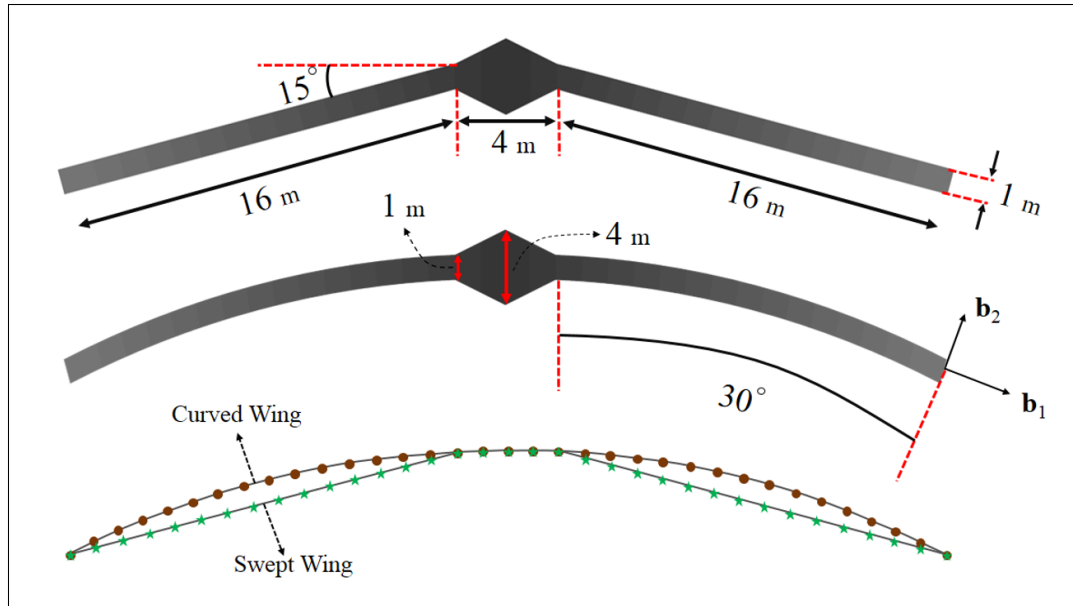
Figure 3.21: Dimensions and schematic top view of the reference lines of the swept and curved configurations [46].
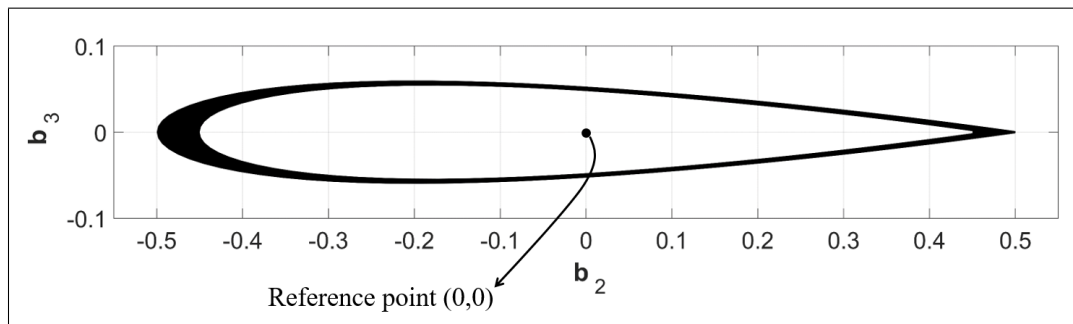
Figure 3.22: Position of the reference point of the cross-section [46].
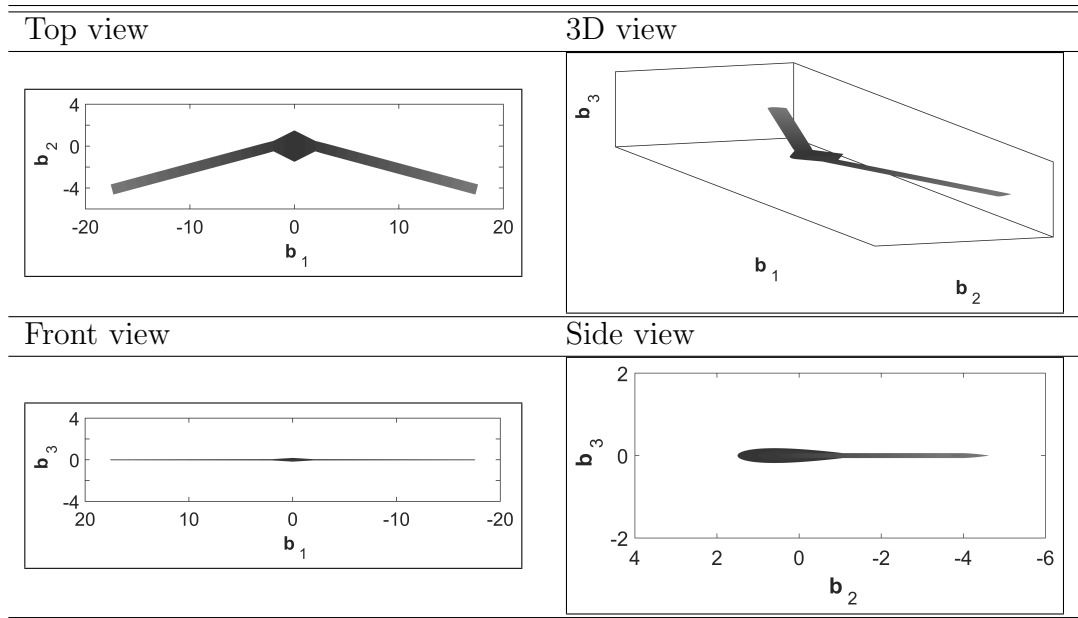
Figure 3.23: Schematic views of swept flying wing model [46].
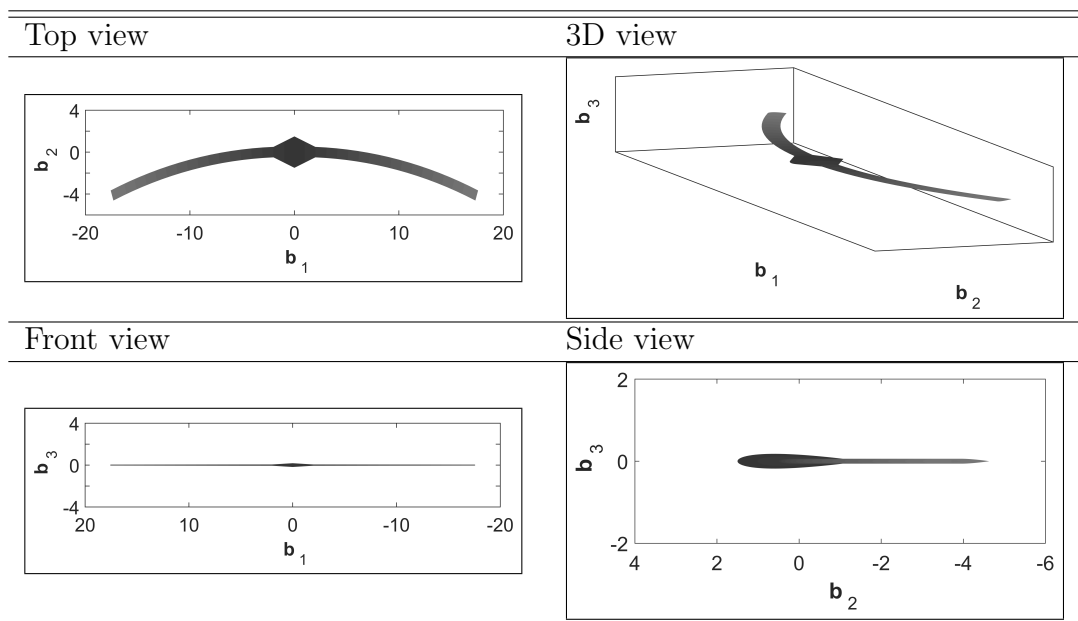
Figure 3.24: Schematic views of curved flying wing model [46].

Additionally, the properties of the wings for these configurations are presented in Tables 3.5 and 3.6. These values are calculated using VABS software. As suggested

by Yu et al. [108], the flexibility components of curved geometry with the isotropic material are slightly different compared to uncurved ones. These minor differences between curved and uncurved wings are observable in Tables 3.5 and 3.6. Both configurations have a total length of 36 m, while each wing has 16 m span, and fuselage length is 4 m. The chords of the wings are constant and equal to 1 m. The aerodynamic properties and coefficients are presented in Table 3.7. Moreover, Table 3.8 shows the properties of the fuselage in the plane of symmetry of the aircraft. These properties are changing linearly from the plane of symmetry of the aircraft to the root of the wings [46].

Property	Value
Span $[m]$	16
R $[N^{-1}]$	$\begin{bmatrix} 7.243 \times 10^{-9} & 0 & 0 \\ 0 & 2.580 \times 10^{-8} & 1.757 \times 10^{-13} \\ 0 & 1.757 \times 10^{-13} & 9.661 \times 10^{-7} \end{bmatrix}$
S $[N^{-1}.m^{-1}]$	$\begin{bmatrix} 0 & -7.547 \times 10^{-15} & 7.370 \times 10^{-9} \\ -3.339 \times 10^{-14} & 0 & 0 \\ -1.161 \times 10^{-6} & 0 & 0 \end{bmatrix}$
T $[N^{-1}.m^{-2}]$	$\begin{bmatrix} 3.480 \times 10^{-6} & 0 & 0 \\ 0 & 4.266 \times 10^{-6} & -6.664 \times 10^{-14} \\ 0 & -6.664 \times 10^{-14} & 6.509 \times 10^{-8} \end{bmatrix}$
I $[kg.m]$	$\begin{bmatrix} 1.760 \times 10^{-1} & 0 & 0 \\ 0 & 2.335 \times 10^{-3} & -3.900 \times 10^{-18} \\ 0 & -3.900 \times 10^{-18} & 1.736 \times 10^{-1} \end{bmatrix}$
ξ $[m]$	$\begin{bmatrix} 0 \\ 1.132 \times 10^{-1} \\ 1.253 \times 10^{-17} \end{bmatrix}$
Mass per unit length $[kg.m^{-1}]$	1.560
Chord $[m]$	1

Table 3.5: Properties of swept wing in SI units [46].

Property	Value
Span $[m]$	16
R $[N^{-1}]$	$\begin{bmatrix} 7.384 \times 10^{-9} & 0 & 0 \\ 0 & 2.571 \times 10^{-8} & 1.587 \times 10^{-13} \\ 0 & 1.587 \times 10^{-13} & 9.630 \times 10^{-7} \end{bmatrix}$
S $[N^{-1}.m^{-1}]$	$\begin{bmatrix} 0 & -3.509 \times 10^{-15} & 7.078 \times 10^{-9} \\ -2.696 \times 10^{-14} & 0 & 0 \\ -1.143 \times 10^{-6} & 0 & 0 \end{bmatrix}$
T $[N^{-1}.m^{-2}]$	$\begin{bmatrix} 3.470 \times 10^{-6} & 0 & 0 \\ 0 & 4.295 \times 10^{-6} & -3.756 \times 10^{-14} \\ 0 & -3.756 \times 10^{-14} & 6.498 \times 10^{-8} \end{bmatrix}$
I $[kg.m]$	$\begin{bmatrix} 1.770 \times 10^{-1} & 0 & 0 \\ 0 & 2.347 \times 10^{-3} & -1.393 \times 10^{-15} \\ 0 & -1.393 \times 10^{-18} & 1.746 \times 10^{-1} \end{bmatrix}$
ξ $[m]$	$\begin{bmatrix} 0 \\ 1.163 \times 10^{-1} \\ 1.486 \times 10^{-17} \end{bmatrix}$
Mass per unit length $[kg.m^{-1}]$	1.566
Chord $[m]$	1

Table 3.6: Properties of curved wing in SI units [46].

Property	Value
Offset of aerodynamic center from reference line, e $[m]$	0.25
c_{l_α}	2π
c_{l_δ}	1
c_{d_0}	0.01
c_{m_0}	0.0
c_{m_α}	0.08
c_{m_δ}	-0.25
Air density $[kg.m^{-3}]$, ρ	0.0889

Table 3.7: Aerodynamic properties and coefficients [46].

Property	Value
Span $[m]$	4
R $[N^{-1}]$	$\begin{bmatrix} 1.308 \times 10^{-9} & 0 & 0 \\ 0 & 4.659 \times 10^{-9} & 3.172 \times 10^{-14} \\ 0 & 3.172 \times 10^{-14} & 1.744 \times 10^{-7} \end{bmatrix}$
S $[N^{-1}.m^{-1}]$	$\begin{bmatrix} 0 & -6.114 \times 10^{-16} & 5.971 \times 10^{-10} \\ -2.705 \times 10^{-15} & 0 & 0 \\ -9.405 \times 10^{-8} & 0 & 0 \end{bmatrix}$
T $[N^{-1}.m^{-2}]$	$\begin{bmatrix} 1.302 \times 10^{-7} & 0 & 0 \\ 0 & 1.596 \times 10^{-7} & -2.494 \times 10^{-15} \\ 0 & -2.494 \times 10^{-15} & 2.436 \times 10^{-9} \end{bmatrix}$
I $[kg.m]$	$\begin{bmatrix} 8.535 & 0 & 0 \\ 0 & 1.133 \times 10^{-1} & -1.447 \times 10^{-16} \\ 0 & -1.447 \times 10^{-16} & 8.421 \end{bmatrix}$
ξ $[m]$	$\begin{bmatrix} 0 \\ 2.831 \times 10^{-1} \\ -8.018 \times 10^{-18} \end{bmatrix}$
Mass per unit length $[kg.m^{-1}]$	10.143
Chord $[m]$	4

Table 3.8: Properties of fuselage in SI units [46].

3.5.2 Eigenvalue analysis and mode shapes

Figure 3.25 shows the normalized results of the eigenvalue analysis of the swept and curved flying wing aircraft. These results are for base model configurations, aircraft with 15-degree swept wings, and curved flying wing with 30-degree curvature. The real and imaginary parts of the eigenvalues for both aircraft are normalized with their flutter frequency. The speed in Fig. 3.25 also is normalized with flutter speeds of the base models. Flutter speed of swept configuration with a 15-degree sweep angle is 50.8 m/s, and the flutter frequency is 11.2 rad/s. On the other hand, the

flutter speed of curved wing aircraft with 30-degree curvature is 42.1 m/s with a frequency of 10.3 rad/s. It is found that the flutter speed of the swept configuration is approximately 21% larger than the flutter speed of the curved wing [46].
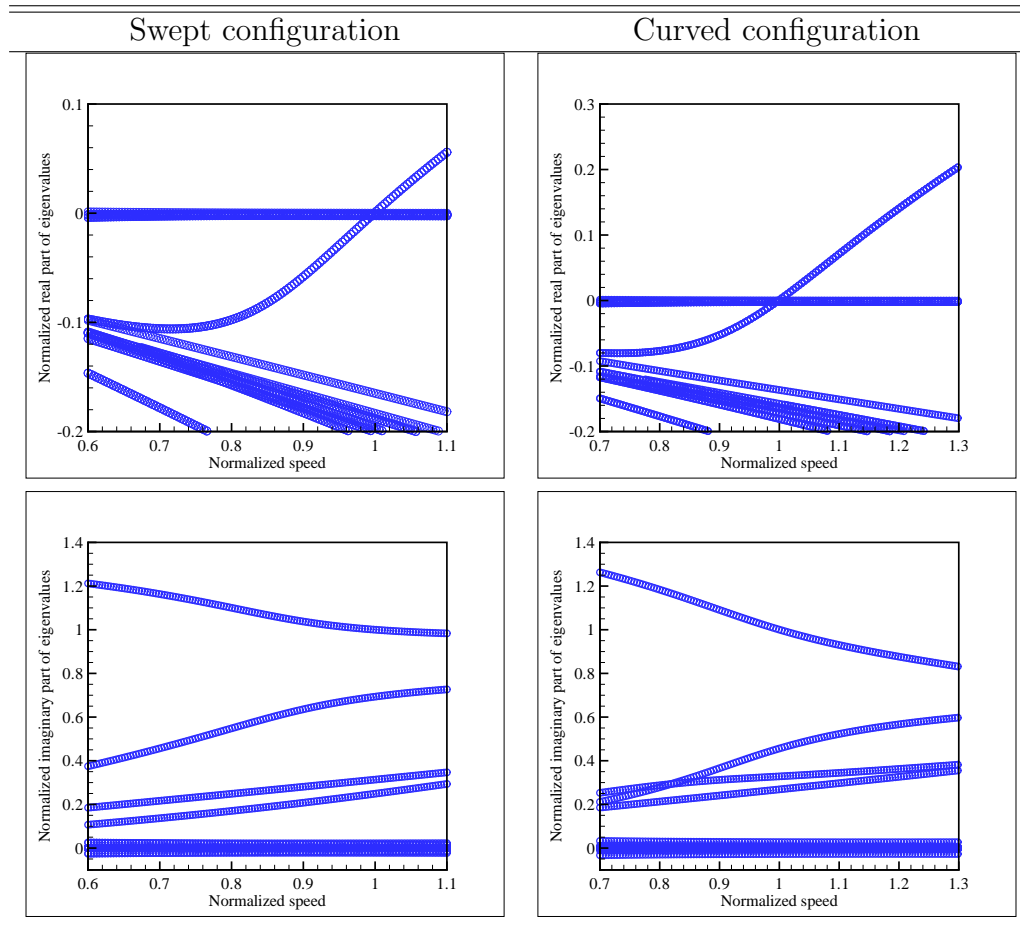
Figure 3.25: Eigenvalue analysis of base model configurations (i.e., aircraft with 15-degree swept wings and curved flying wing with 30-degree curvature) [46].

The unstable modes of both aircraft are shown in Figs. 3.26 and 3.27. The body-freedom flutter mode of the swept flying wing configurations is a combination of the first and second bending mode with the short period mode of the aircraft, and the body-freedom flutter mode of the curved flying wing is a combination of the first bending mode and the short period mode of the aircraft [46].
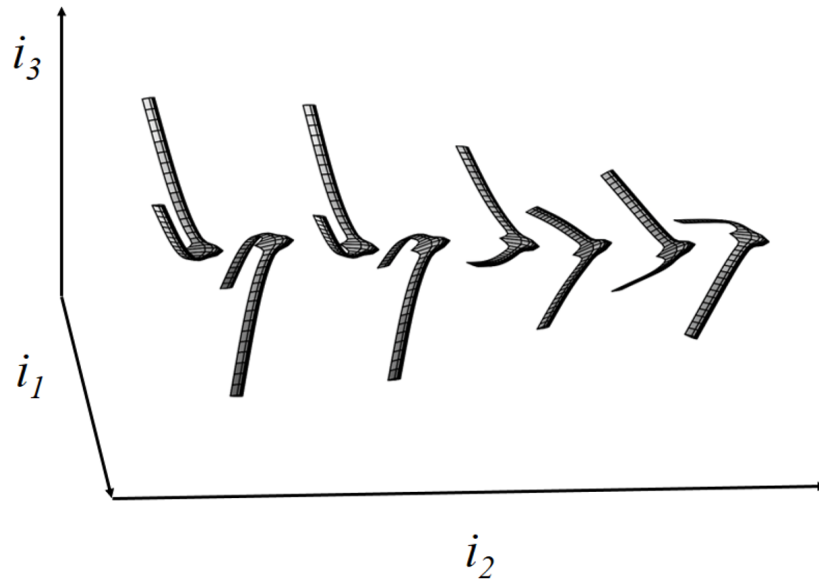
Figure 3.26: The schematic view of the body-freedom flutter mode shape of the flying wing aircraft with 15-degree swept wings [46].
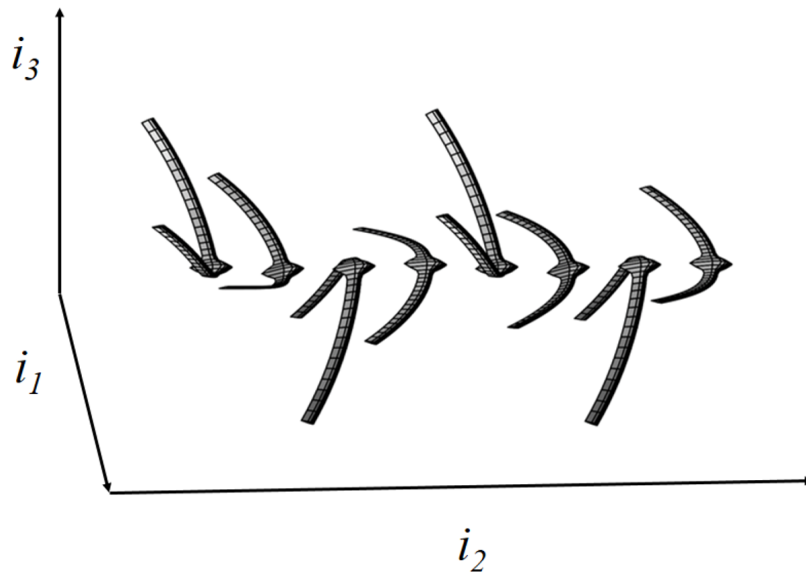
Figure 3.27: The schematic view of the body-freedom flutter mode shape of the flying wing aircraft with 30-degree curved wings [46].

3.5.3 Flutter analysis

In this section, the results of the stability analysis of the curved and the swept flying wing are illustrated. Three sweep and three curvature angles are considered, and the stability results are presented [46].

Here, case I is the comparison between two flying wing aircraft, one has wings with a 15-degree sweep angle and the other one with 30-degree curvature in its wings. Case II offers two configurations, one with 17.5-degree swept wings and another one with 35-degree curved wings. Lastly, case III contains two designs; one has wings with a 20-degree sweep angle and the other one with 40-degree curved wings [46].
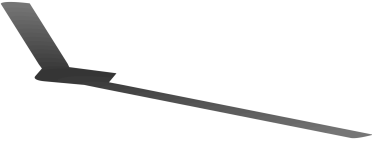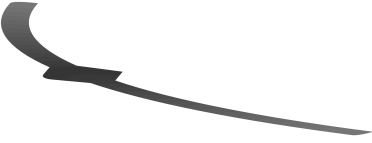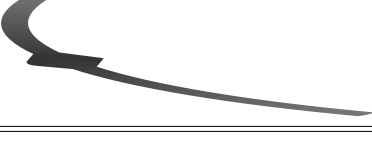
	Angle	Aircraft	Flutter Speed (m/s)	Flutter frequency (rad/s)
Case I	Sweep 15		50.8	11.2
	Curvature 30		42.1	10.3
Case II	Sweep 17.5		60.8	12.6
	Curvature 35		47.7	11.7
Case III	Sweep 20		73.8	13.9
	Curvature 40		54.1	13.1

Table 3.9: Flutter speed and frequency of cases I, II, and III [46].

The flutter characteristics of these cases are available in Table 3.9. All the cases show a significant difference between the flutter speed of swept and curved flying wing aircraft — the difference increases as the sweep and curvature angle increases. In case I, the difference between flutter speeds is 8.7 m/s, while for case III, it increases to 19.7 m/s. This shows the advantageous of swept configuration compared to the curved model [46].

CHAPTER 4

GUST AND BLAST–INDUCED GUST RESPONSE SUPPRESSION

4.1   Background

Very flexible high-aspect-ratio wings are widely used in the design of HALE aircraft. These wings, due to their characteristics, may subject to large deformation, which causes geometric nonlinearities. As a result, conducting the nonlinear aeroelastic analysis is necessary when it comes to the design of very flexible configurations [85, 86, 87]. Additionally, time-dependent external excitation including gust [50, 65, 97, 103], and blast [48, 53, 70, 79, 99], can lead to instability even if the aircraft is flying below the stability boundary. Therefore, the determination of nonlinear aeroelastic responses to time-dependent excitation is a crucial topic for the design of very flexible flying wings [45].

Gust loads can result in large deformations in the case of a highly flexible aircraft [45]. The flight dynamic characteristics and gust response of highly flexible aircraft were investigated by Patil and Taylor [88]. It was reported that the non-uniform gust creates higher responses in a case of high-aspect-ratio flying wing compare to uniform gusts. Additionally, the nonlinear gust response of a highly flexible aircraft was reported by Patil [84], which he found that the time domain response matches with frequency domain response presented in work by Patil and Taylor [88].

Ricciardi et al. [93] investigated the accuracy of the Pratt method for unconventional HALE aircraft. The Pratt method and transient method were used to analyze the gust response on the joined-wing and flying-wing model. It was found that the Pratt method is only useful for the preliminary design of the joined-wing model. However, when it comes to the design of the flying-wing model, the Pratt method is inadequate. Yi et al. [55] compared a theoretical and experimental approach of

a flexible high-aspect-ratio wing exposed to a harmonic gust. It was found that a very flexible wing experiences different gust response characteristics under different load conditions, and the responses are difficult to evaluate using linear analysis [45].

Marzocca et al. [69] studied the aeroelastic response of a 2D lifting surface to time-dependent excitations in an incompressible flow field with plunging and pitching motions. The response for different types of gust loads (e.g., sharp-edged gusts, I-cosine, triangular gust, graded gust, and blast loads due to a sonic boom overpressure signature) has been reported. They found that an increase in the structural coupling parameter will increase the frequency of oscillations when the lifting surface is subjected to the blast load and I-cosine gust. For lifting surfaces subjected to both gust and blast loads, it was shown that the influence of the gust was almost insignificant compared to the influence of the blast load, especially at higher mass ratio [64].

In similar research that involved determining the aeroelastic response of a 2D airfoil to blast loads in a compressible field [70], the authors calculated the aerodynamic loads for different flight regimes starting from subsonic to hypersonic. The flutter speed and frequency for the subsonic regimes were calculated using Theodorsen model, whereas for the hypersonic speed regime the piston theory aerodynamics was applied [64].

Na and Librescu [79] further investigated the effects of blast loads to adaptive cantilevers carrying external stores by measuring their dynamic response [79]. They considered an isotropic beam with a biconvex cross-section. The results revealed that a more efficient control could be achieved when the store is located toward the middle of the beam [64].

Finding ways to suppress the responses of highly flexible configuration due to time-dependent excitations is a challenging aspect of design. Tang et al. [97] con-

ducted an experimental and theoretical study to investigate the effect of store location on the flutter velocity and LCO. A delta wing for the purpose of experimentation was chosen. It was reported that the experimental investigation and theoretical studies were in good agreement and they showed that the structural natural frequency of the wing/store declines as the store moves from the root to the tip of the wing. They concluded that mounting the store at the leading edge of the wingtip leads to higher critical flutter velocity [45].

In this chapter, first, the effects of engine placement on the gust response of a very flexible cantilever wing are presented. Then, the effects of engine placement on aeroelastic gust response of a flying wing aircraft, which is subjected to different gust load are provided. Finally, the effect of armament placement on the on blast load and blast-induced gust response is discussed. The results reveal that the correct choice of design leads to suppression of gust and blast load responses.

4.2 Engine Placement Effects on Nonlinear Aeroelastic Gust Response of High-Aspect-Ratio Wings

The effects of engine placement on the nonlinear aeroelastic response of a very flexible high-aspect-ratio wing is investigated in the presence of gust. The properties of the cantilever wing are presented in Chapter 3 Table 3.1. The wing is aft swept 15°, and modeled using 20 elements. As shown in Fig. 4.1, η is the dimensionless length in the $\mathbf{b}_1$ direction, along which the engine is located.

The problem is studied by the second-order, central-difference, time marching algorithm with high-frequency damping in NATASHA [86]. In order to study the effects of engine placement on the gust response, the airspeed is considered constant and equal to 35 m/s while the engine moves along the wing. Furthermore, the

duration of the gust is chosen to be equal to 5 seconds. The appropriate time step is 0.01 seconds. Time and the wingtip position are normalized using the period of oscillation of the base model at flutter boundary (i.e., 0.0445 1/s) and the wing length (i.e., 16 m), respectively.
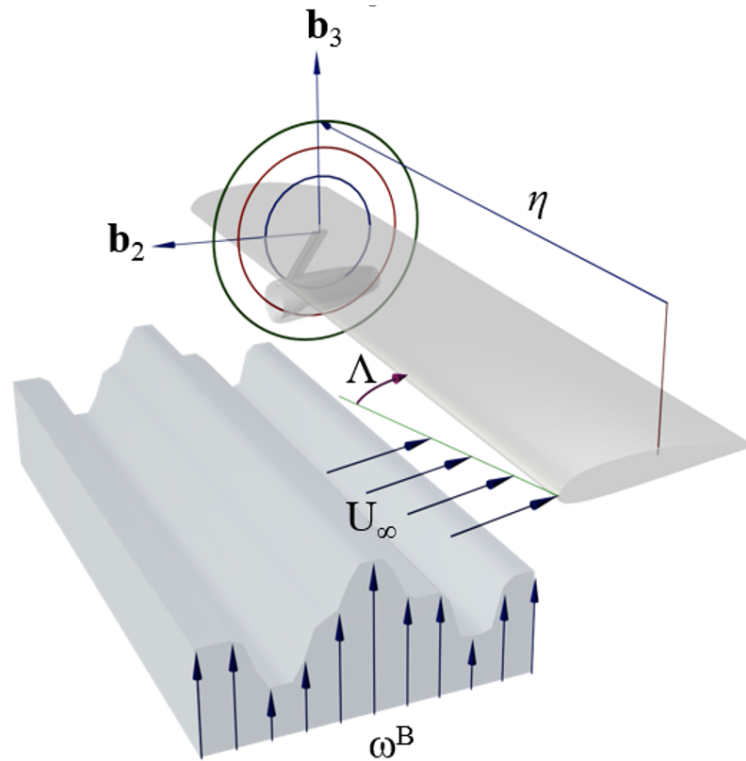
Figure 4.1: Schematic 3D view of a very flexible high-aspect-ratio exposed to gust.

– Root of the wing: Fig. 4.2 illustrates the normalized results of wingtip position for the engine placement at the root of the wing with no offset. The response shows that the wing becomes unstable and experiences LCO with a relatively small amplitude.

– 25% of the span: Fig. 4.3 shows the results of the time domain in the 25% of the span without offset. It is observed that the wing experiences limit cycle oscillations similar to the engine placement at the root of the wing. The amplitude of the oscillation is relatively small for this case. The flutter speed of the wing for

this engine placement is equal to the flutter speed of the engine placement at the root of the wing (see Figs. 3.4 – 3.6).
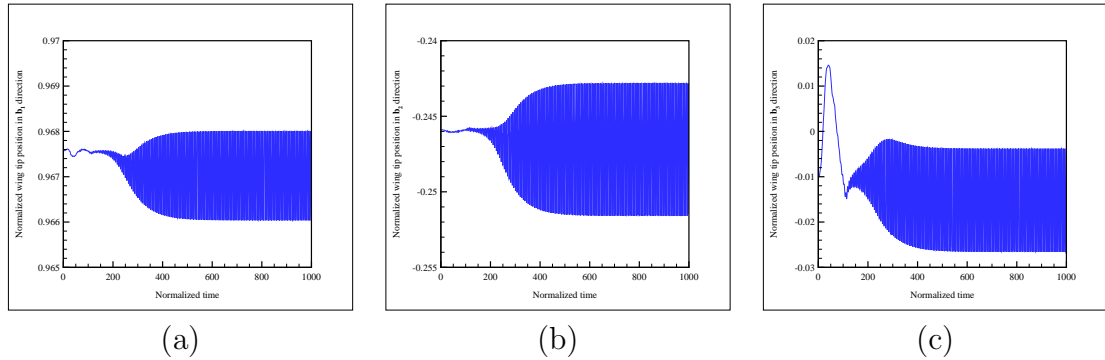
Figure 4.2: Normalized wing tip position $\frac{r_1+u_1}{l}$ vs normalized time $\frac{t}{t_N}$ for engine placement at $x_1/l = 0$ and $x_2/b = 0$ ((a): In $\mathbf{b}_1$ direction, (b): In $\mathbf{b}_2$ direction, and (c): In $\mathbf{b}_3$ direction [66]).
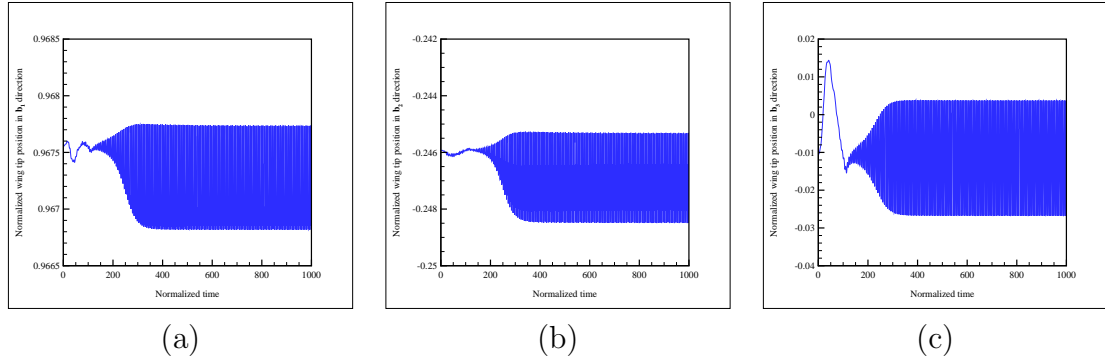
Figure 4.3: Normalized wing tip position $\frac{r_1+u_1}{l}$ vs normalized time $\frac{t}{t_N}$ for engine placement at $x_1/l = 0.25$ and $x_2/b = 0$ ((a): In $\mathbf{b}_1$ direction, (b): In $\mathbf{b}_2$ direction, and (c): In $\mathbf{b}_3$ direction).

   – 50% of the span: The time-domain results for the engine placement at the 50% of the span without offset are displayed in Fig. 4.4. Compare to the results for engine placement at the root of the wing and 25% of the wingspan, the amplitude of the oscillation is very small. It is noteworthy that although the amplitude of the oscillation is smaller than the amplitude of the oscillation for the engine placement at the root and 25% of the wingspan, the flutter speed is higher (see Fig. 3.6).

– 75% of the span: Fig. 4.5 presents the results of the time domain analysis for the engine placement at the 75% of the span and $x_2/b = 1$. NATASHA's results for this point indicate that all the excitations from gust die out, and the wing remains stable. Referring to Fig. 3.4, it is observed that this point has the maximum flutter speed. Additionally, Fig. 4.6 illustrates the effects of engine placement on the gust excitation for engine placement at the 75% of the span and $x_2/b = -1$. The results indicate chaotic oscillation with a significantly larger amplitude compares to the aforementioned cases.

(a)   (b)   (c)
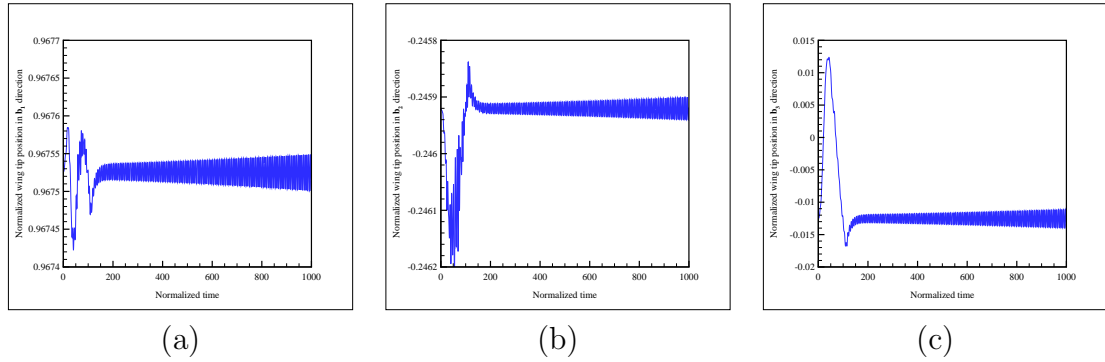
Figure 4.4: Normalized wing tip position $\frac{r_1+u_1}{l}$ vs normalized time $\frac{t}{t_N}$ for engine placement at $x_1/l = 0.5$ and $x_2/b = 0$ ((a): In $\mathbf{b}_1$ direction, (b): In $\mathbf{b}_2$ direction, and (c): In $\mathbf{b}_3$ direction).

(a)   (b)   (c)
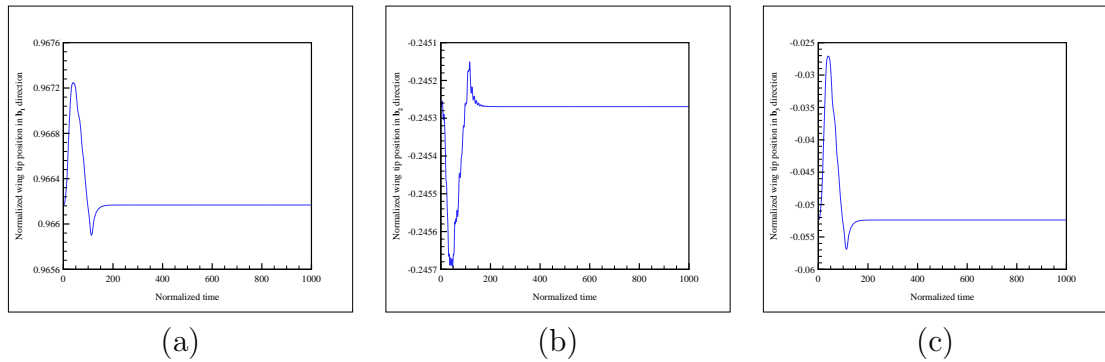
Figure 4.5: Normalized wing tip position $\frac{r_1+u_1}{l}$ vs normalized time $\frac{t}{t_N}$ for engine placement at $x_1/l = 0.75$ and $x_2/b = 1$ ((a): In $\mathbf{b}_1$ direction, (b): In $\mathbf{b}_2$ direction, and (c): In $\mathbf{b}_3$ direction [66]).
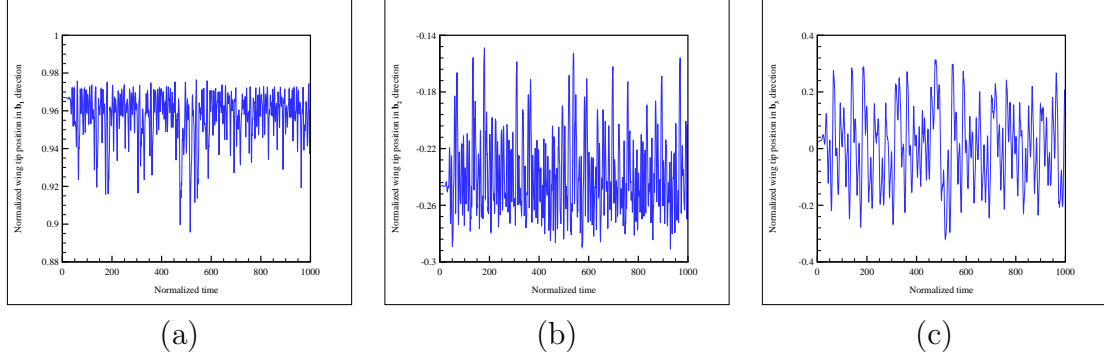
Figure 4.6: Normalized wing tip position $\frac{r_1+u_1}{l}$ vs normalized time $\frac{t}{t_N}$ for engine placement at $x_1/l = 0.75$ and $x_2/b = -1$ ((a): In $\mathbf{b}_1$ direction, (b): In $\mathbf{b}_2$ direction, and (c): In $\mathbf{b}_3$ direction).

– Tip of the wing: Fig. 4.7 shows the results for the engine placement at the tip of the wing and $x_2/b = 1$. Similar to engine placement at the 75% of the span and $x_2/b = -1$, the results show chaotic oscillation with a large amplitude. Based on the results of the contours of flutter speed presented in Fig. 3.4, these two areas have considerably lower flutter speed compare to the flutter speed of the wing root.
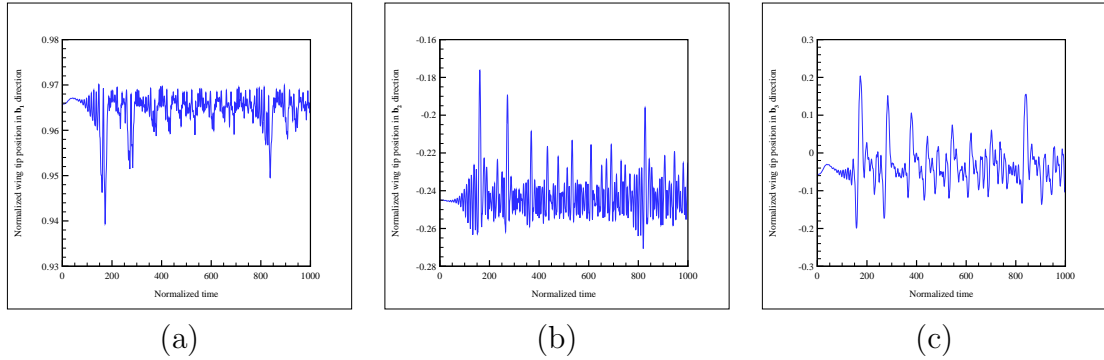
Figure 4.7: Normalized wing tip position $\frac{r_1+u_1}{l}$ vs normalized time $\frac{t}{t_N}$ for engine placement at $x_1/l = 1$ and $x_2/b = 1$ ((a): In $\mathbf{b}_1$ direction, (b): In $\mathbf{b}_2$ direction, and (c): In $\mathbf{b}_3$ direction).

4.3 Nonlinear Aeroelastic Response of Highly Flexible Flying Wing Due to Different Gust Loads

A very flexible high-aspect-ratio flying wing, presented in Fig. 4.8, is designed in order to investigate the effects of different gust loads. The gust profiles are presented in Fig. 4.9. These profiles presented in Fig. 4.9 is generated by passing the Gaussian white noise through the Dryden spectrum model. The properties of the flying wing are presented in Table 4.1. The wings are aft swept 15°, and each wing has 20 elements. The fuselage is considered as a rigid body which contains four elements. The weight of each element of the fuselage is five times the weight of the elements of the wings. The aircraft has two engines with a mass of 10 kg [45].

Figure 4.8: Schematic 3D view of a very flexible high-aspect-ratio wing [45].
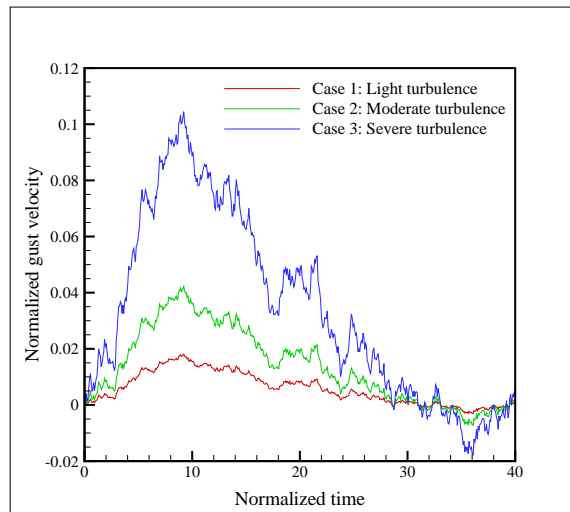
Figure 4.9: Gust velocity profile vs. time [45].

Property	Value
Span	16
Number of elements	20
Sweep angle	15

$$R = \begin{bmatrix} 9.06 \times 10^{-9} & 0 & 0 \\ 0 & 3.50 \times 10^{-8} & 7.22 \times 10^{-13} \\ 0 & 7.22 \times 10^{-13} & 1.18 \times 10^{-6} \end{bmatrix}$$

$$S = \begin{bmatrix} 0 & 2.63 \times 10^{-12} & 7.57 \times 10^{-11} \\ -3.01 \times 10^{-12} & 0 & 0 \\ -1.02 \times 10^{-6} & 0 & 0 \end{bmatrix}$$

$$T = \begin{bmatrix} 4.33 \times 10^{-6} & 0 & 0 \\ 0 & 5.53 \times 10^{-6} & 2.42 \times 10^{-14} \\ 0 & 2.42 \times 10^{-14} & 8.43 \times 10^{-8} \end{bmatrix}$$

$$I = \begin{bmatrix} 4.78 \times 10^{-1} & 0 & 0 \\ 0 & 7.2 \times 10^{-3} & -1.04 \times 10^{-10} \\ 0 & -1.04 \times 10^{-10} & 4.71 \times 10^{-1} \end{bmatrix}$$

$$\xi = \begin{bmatrix} 0 \\ 8.98 \times 10^{-4} \\ -4.76 \times 10^{-7} \end{bmatrix}$$

Property	Value
Mass per unit length	4.38
Chord, c	1
Offset of aerodynamic center from reference line, e	0.125
c_{l_α}	2π
c_{l_δ}	1
c_{d_0}	0.01
c_{m_0}	0.0
c_{m_α}	-0.08
Gravity, g	9.8
Air Density, ρ	0.4135

Table 4.1: Properties of wing in SI units [45].

In this section, two cases are considered. First, when the engines are mounted at the root of the wing, and the second case when the engines are located at 60% of the span forward of the reference line. The velocity results are normalized with the aircraft cruise speed 50 m/s. The wingtip deflection also normalized with the length of the entire flying wing (i.e., 35.2 m), and the time is normalized with the period of oscillation of the flying wing at the flutter boundary when the engines are located at the root (i.e., 0.129 s) [45].

4.3.1 Engine placement at root of the wings

When the engines are located at the root of the flying wing, the wings experience flutter at the speed of 48.9 m/s with a frequency of 7.7 rad/s [45].

Figures 4.10– 4.15 illustrate the results of time-domain analysis when the engine is mounted at the root of the flying wing for different gust profiles in which case 1, case 2, and case 3 indicate the results when the flying wing exposed to light, moderate and severe turbulence, respectively. It is found that the tip deflection increases in all directions when the gust load changes from light to severe turbulence. The same also happens for velocities — the velocity of the wingtip in different directions increases [45].

(a) (b) (c)
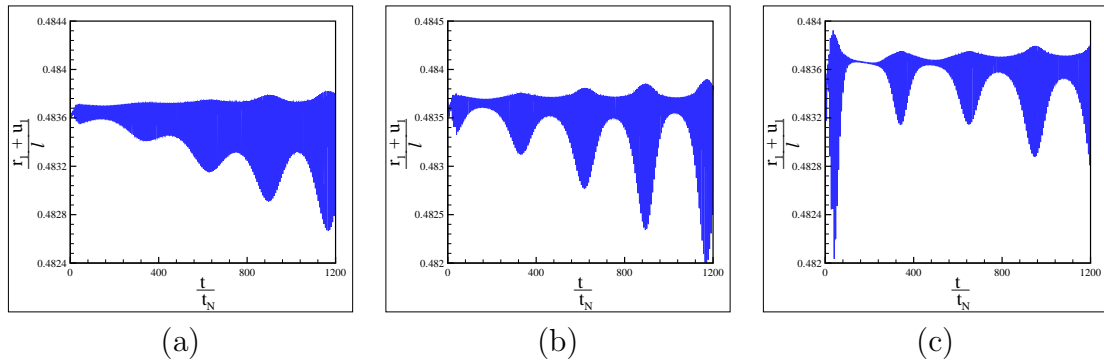
Figure 4.10: Normalized wing tip position $\frac{r_1+u_1}{l}$ vs normalized time $\frac{t}{t_N}$ ((a): Case 1, (b): Case 2, and (c): Case 3) [45].

(a) (b) (c)
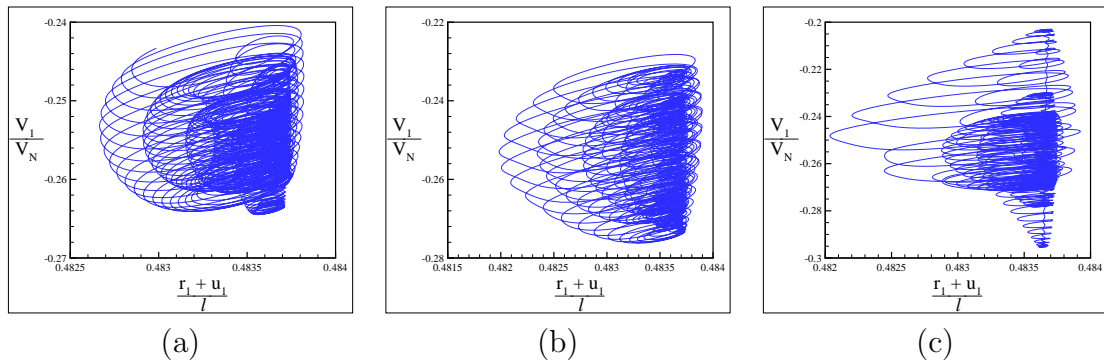
Figure 4.11: Normalized velocity vector of wing tip $\frac{V_1}{V_N}$ vs normalized wing tip position $\frac{r_1+u_1}{l}$ ((a): Case 1, (b): Case 2, and (c): Case 3) [45].
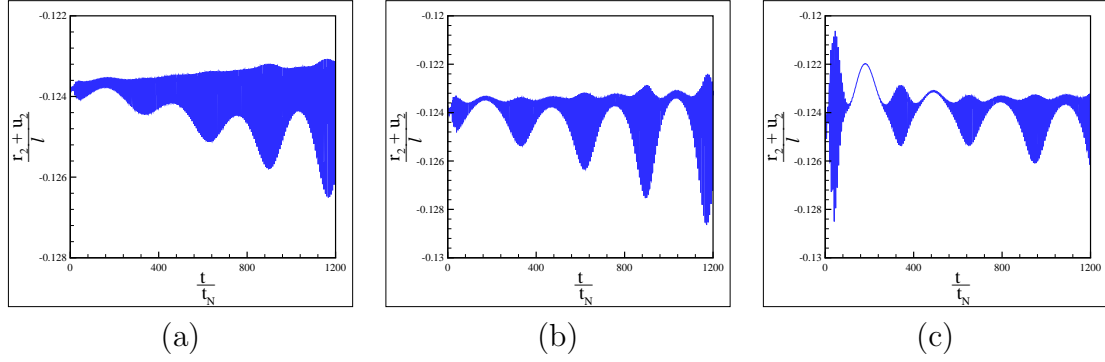
Figure 4.12: Normalized wing tip position $\frac{r_2+u_2}{l}$ vs normalized time $\frac{t}{t_N}$ ((a): Case 1, (b): Case 2, and (c): Case 3) [45].
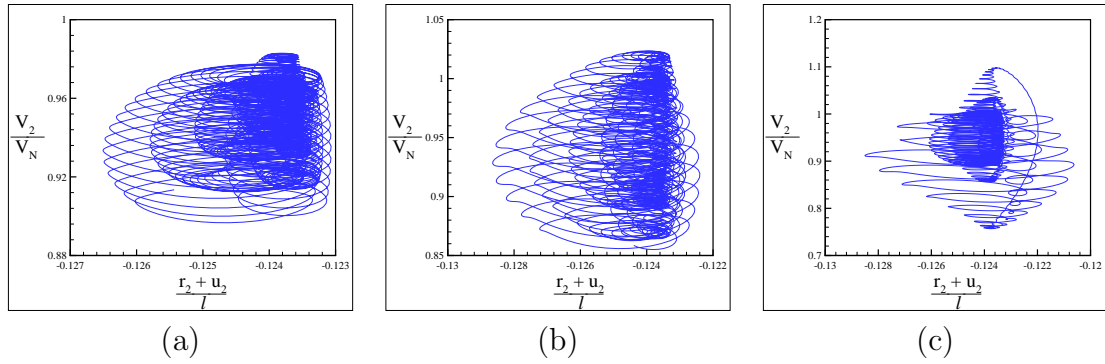
Figure 4.13: Normalized velocity vector of wing tip $\frac{V_2}{V_N}$ vs normalized wing tip position $\frac{r_2+u_2}{l}$ ((a): Case 1, (b): Case 2, and (c): Case 3) [45].
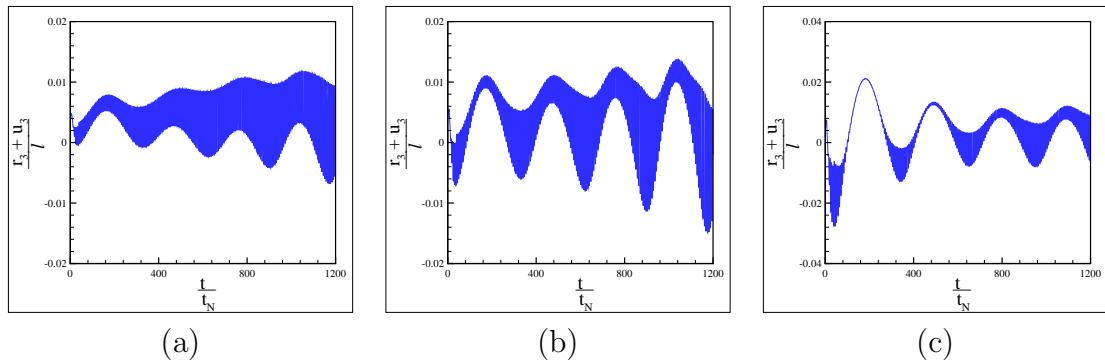
Figure 4.14: Normalized wing tip position $\frac{r_3+u_3}{l}$ vs normalized time $\frac{t}{t_N}$. ((a): Case 1, (b): Case 2, and (c): Case 3) [45].
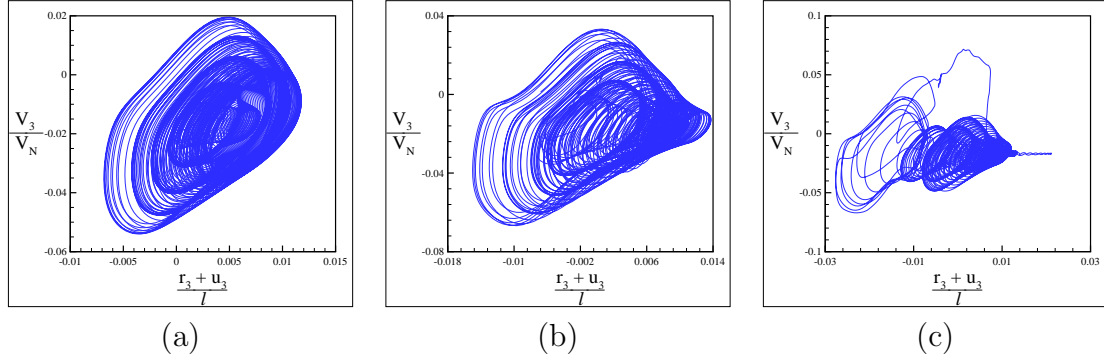
Figure 4.15: Normalized velocity vector of wing tip $\frac{V_3}{V_N}$ vs normalized wing tip position $\frac{r_3+u_3}{l}$ ((a): Case 1, (b): Case 2, and (c): Case 3) [45].

4.3.2 Engine placement at 60% of span forward of reference line

In another case, the engines are mounted at 60% of the span forward of the reference line. It is found that the flying wing becomes unstable at the speed of 75.6 m/s [45].

Figures 4.16 – 4.18 show the results of time-domain analysis when the engine is located in the area of maximum flutter speed (i.e., 60% of span forward of reference line). The results reported for three different gust profiles. The results for this arrangement indicate that all the excitations from gust loads with different strength, range from light to severe loads die out, and the wing remains stable [45].

(a)   (b)   (c)
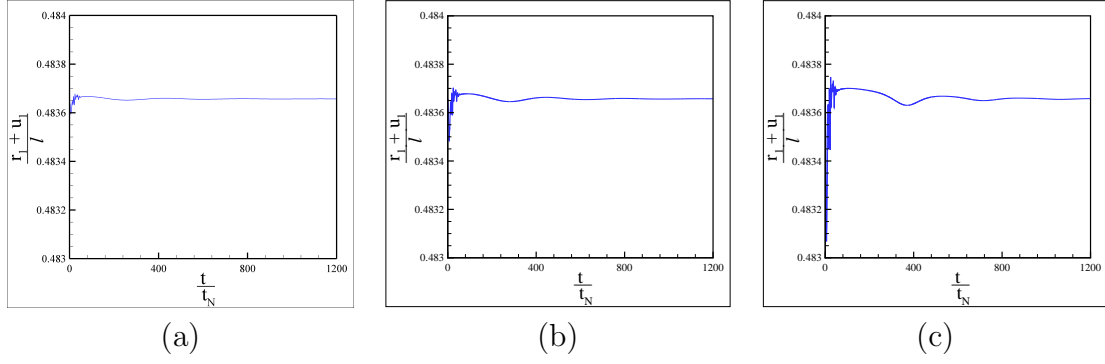
Figure 4.16: Normalized wing tip position $\frac{r_1+u_1}{l}$ vs normalized time $\frac{t}{t_N}$ ((a): Case 1, (b): Case 2, and (c): Case 3) [45].

(a)   (b)   (c)
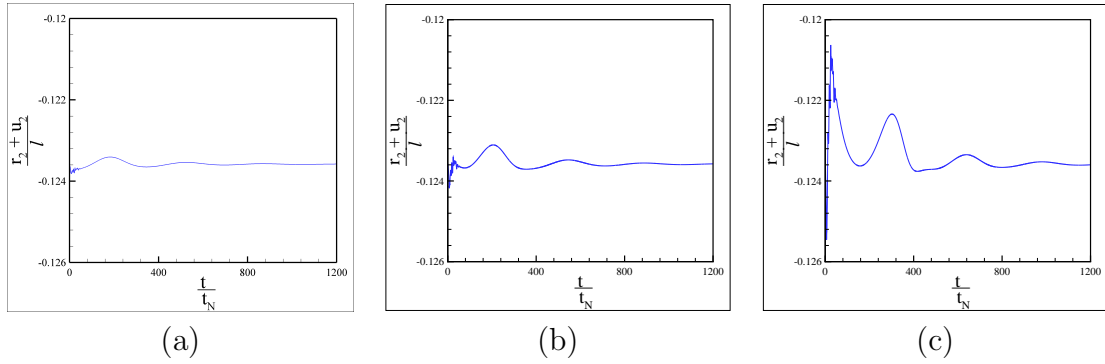
Figure 4.17: Normalized wing tip position $\frac{r_2+u_2}{l}$ vs normalized time $\frac{t}{t_N}$ ((a): Case 1, (b): Case 2, and (c): Case 3) [45].

(a)   (b)   (c)
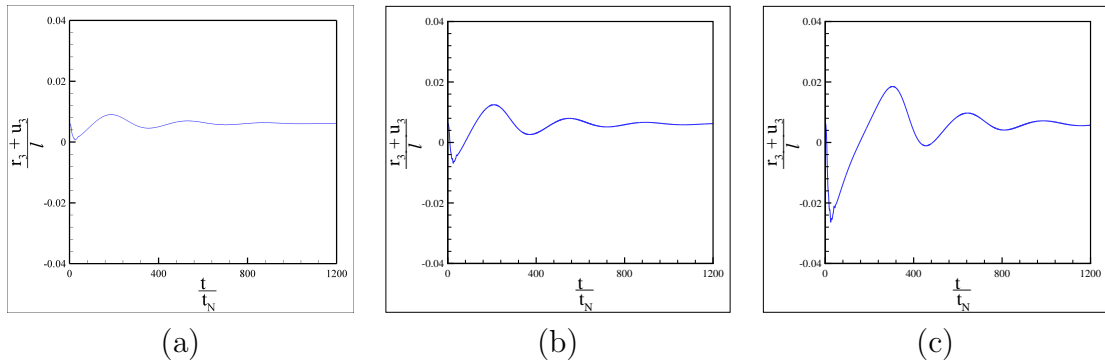
Figure 4.18: Normalized wing tip position $\frac{r_3+u_3}{l}$ vs normalized time $\frac{t}{t_N}$ ((a): Case 1, (b): Case 2, and (c): Case 3) [45].

4.4 Effect of Shooting and Blast-Induced Gust on Nonlinear Aeroelastic Stability and Behavior of High-Aspect-Ratio Wing

This section discusses the effects of armament placement on the nonlinear aeroelastic stability of high-aspect-ratio wing due to blast-induced gust, blast load, and mass release. The flutter analysis of this problem was presented in section 3.3.

In order to study the effects of shooting and blast-induced gust on the gun placements, the airspeed is considered constant and equal to 40 m/s. Furthermore, the duration of the gust is chosen to be equal to 31.3 (i.e., 2 seconds) with a sharp edge linearly decreasing pattern. The wingtip position vector, velocity vector of the wingtip and the time are normalized using the length of the beam (i.e. $l = 18$ m), the airspeed (i.e. $V_N = 40$ m/s) and the period of oscillation of the base model at flutter boundary (i.e. $t_N = 0.064$ s), respectively [64].
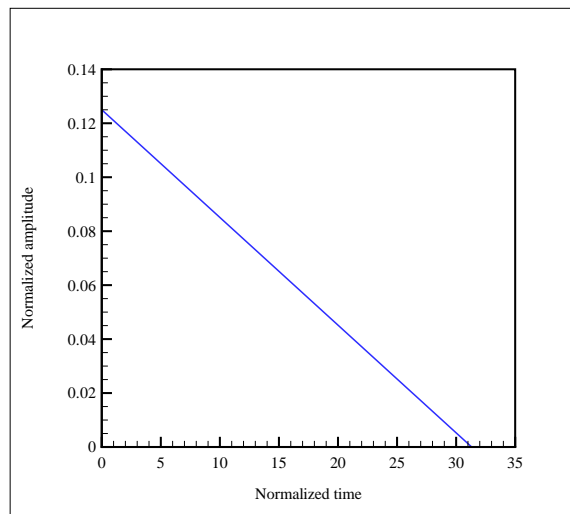
Figure 4.19: Local blast-induced gust profile in vertical direction [64].

Figure 4.20 shows a summary of the results of the time-domain analysis. The re-

sponses are presented in four different categories: no oscillation, damped oscillation, decreasing oscillation, and stable LCO. No oscillation indicates that the amplitude of oscillation is zero. Damped oscillation represents a kind of oscillation that starts from a specific magnitude and approaches zero after some time. On the other hand, decreasing oscillation presents the cases that the magnitude of oscillation is decreasing with time; however, there is no report on whether it reaches zero or not. Stable LCO represents the cases in which the magnitude of oscillation is constant from the beginning or reaches a constant value after some time. Fig. 4.20 indicates that for the gun placement at the root of the wing, 25% and 50% of span, there are no oscillations or the oscillations are so small which make this area a safe zone for the gun to be mounted. Likewise, the area of maximum flutter speed (i.e., 75% of the span, forward of the reference line) is a suitable place for armament placement [64].
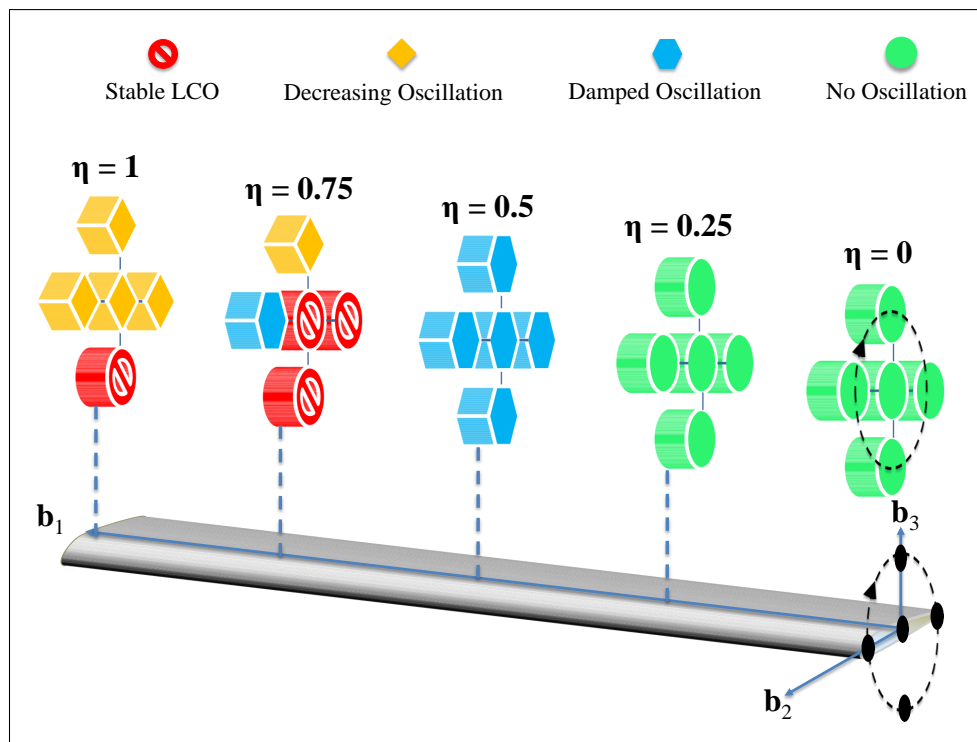
Figure 4.20: A schematic of gun placement along the span of the wing [64].

Figures 4.21 - 4.22 display the results for time domain when the gun is placed at 75% of span without offset. The flutter speed of the wing for this arrangement is almost equal to the flutter speed of the gun when placed at the root of the wing. The wing experiences limit cycle oscillations with relatively large amplitudes [64].

Figures 4.23 - 4.24 illustrate the results of time-domain when the gun is placed at 75% of the span below the reference line, with an offset $x_3/b = -1$. The amplitude of oscillation increases at the beginning until it reaches a constant value [64].

Figures 4.25 - 4.26 display the time domain results for the gun placement at 75 % of the span above the reference line, with an offset $x_3/b = 1$. For this arrangement, the amplitudes of oscillations decrease with time. Fig. 3.13 shows that for this arrangement, the flutter speed is almost equal to the flutter speed of the base model [64].

Additionally, Figs. 4.27 - 4.28 show the time domain results for the gun placement at 75 % of the span forward of the reference line. The oscillation initially shows a small perturbation but soon dies out, indicating that placing the gun forward of the reference line helps to reduce the oscillation of the wing significantly. It is interesting that the flutter speed of this arrangement is substantially large. Comparing the flutter speed and time-domain results for 75% of span indicates that the area with maximum flutter speed (i.e., forward of reference line) provides a safe zone for the gun placement. In contrast, the gun placement in the area with minimum flutter speed (i.e., below the reference line) produces large oscillations [64].

Figures 4.29 - 4.30 illustrate the results for the gun placement at the tip of the wing, with no offsets. The magnitude of the oscillation is relatively large. However, it slowly decreases with time. Fig. 4.20 indicates that for the gun placement below the reference line, the wing experiences LCO, but for the rest of the positions, the oscillations decrease through time [64].
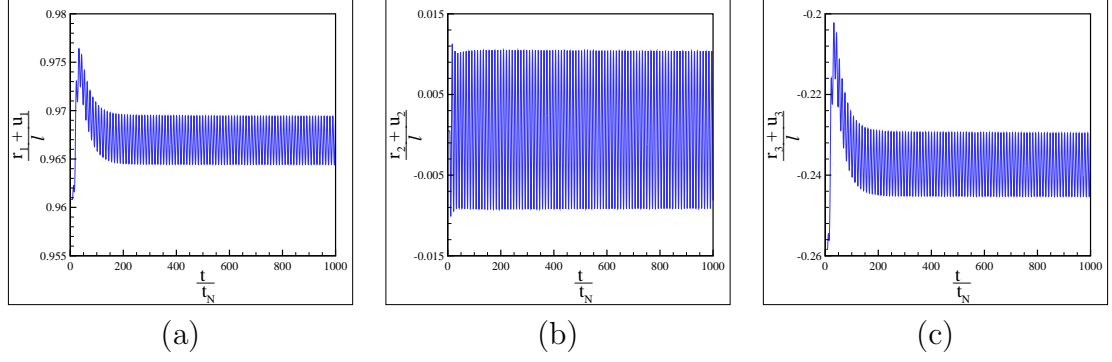
Figure 4.21: Time domain results of wing tip for gun placement at 75% of the span, with no offset ((a):$\frac{r_1+u_1}{l}$ vs. $\frac{t}{t_N}$, (b): $\frac{r_2+u_2}{l}$ vs. $\frac{t}{t_N}$, and (c): $\frac{r_3+u_3}{l}$ vs. $\frac{t}{t_N}$) [64].

Figure 4.22: Time domain results of wing tip for gun placement at 75% of the span, with no offset ((a): $\frac{V_1}{V_N}$ vs. $\frac{r_1+u_1}{l}$, (b): $\frac{V_2}{V_N}$ vs. $\frac{r_2+u_2}{l}$, and (c): $\frac{V_3}{V_N}$ vs. $\frac{r_3+u_3}{l}$) [64].
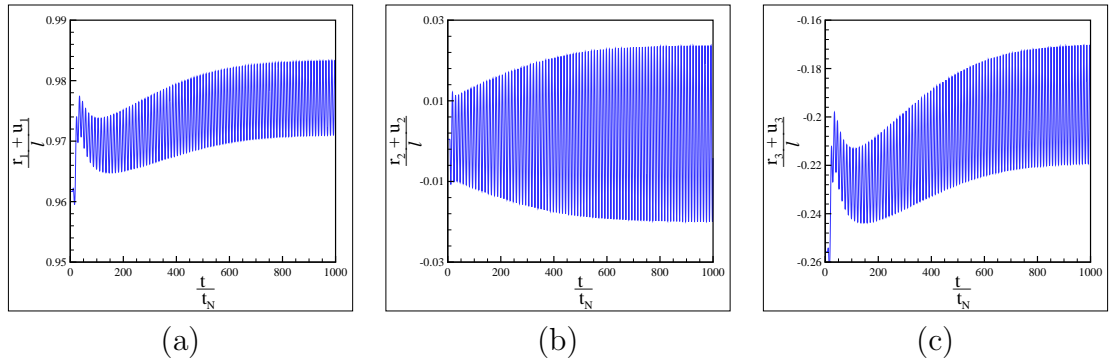
Figure 4.23: Time domain results of wing tip for gun placement at 75% of the span, below the reference line ((a):$\frac{r_1+u_1}{l}$ vs. $\frac{t}{t_N}$, (b): $\frac{r_2+u_2}{l}$ vs. $\frac{t}{t_N}$, and (c): $\frac{r_3+u_3}{l}$ vs. $\frac{t}{t_N}$) [64].

60
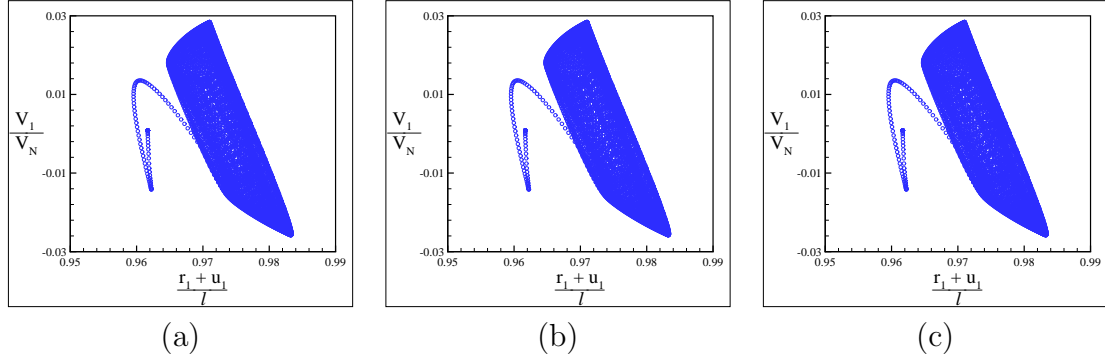
Figure 4.24: Time domain results of wing tip for gun placement at 75% of the span, below the reference line ((a): $\frac{V_1}{V_N}$ vs. $\frac{r_1+u_1}{l}$, (b): $\frac{V_2}{V_N}$ vs. $\frac{r_2+u_2}{l}$, and (c): $\frac{V_3}{V_N}$ vs. $\frac{r_3+u_3}{l}$) [64]).
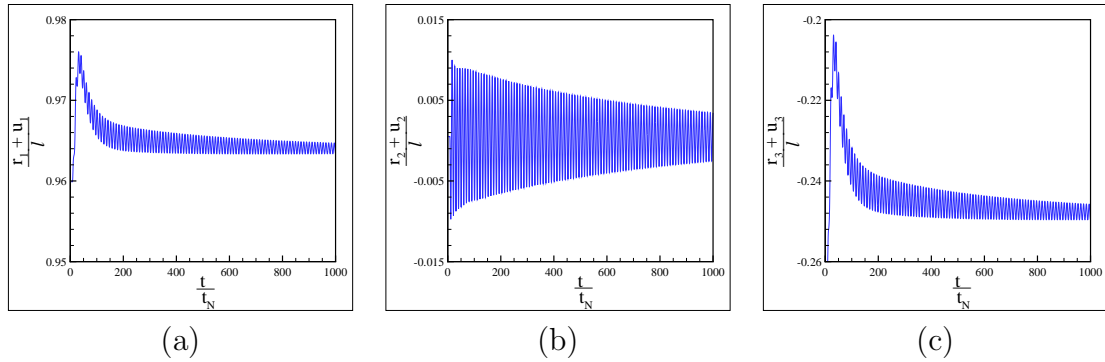
Figure 4.25: Time domain results of wing tip for gun placement at 75% of the span, above the reference line ((a):$\frac{r_1+u_1}{l}$ vs. $\frac{t}{t_N}$, (b): $\frac{r_2+u_2}{l}$ vs. $\frac{t}{t_N}$, and (c): $\frac{r_3+u_3}{l}$ vs. $\frac{t}{t_N}$) [64].
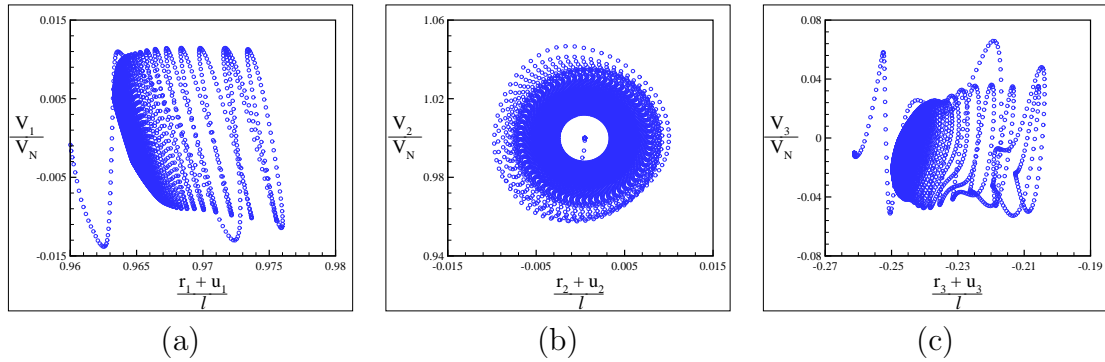
Figure 4.26: Time domain results of wing tip for gun placement at 75% of the span, above the reference line ((a): $\frac{V_1}{V_N}$ vs. $\frac{r_1+u_1}{l}$, (b): $\frac{V_2}{V_N}$ vs. $\frac{r_2+u_2}{l}$, and (c): $\frac{V_3}{V_N}$ vs. $\frac{r_3+u_3}{l}$) [64].
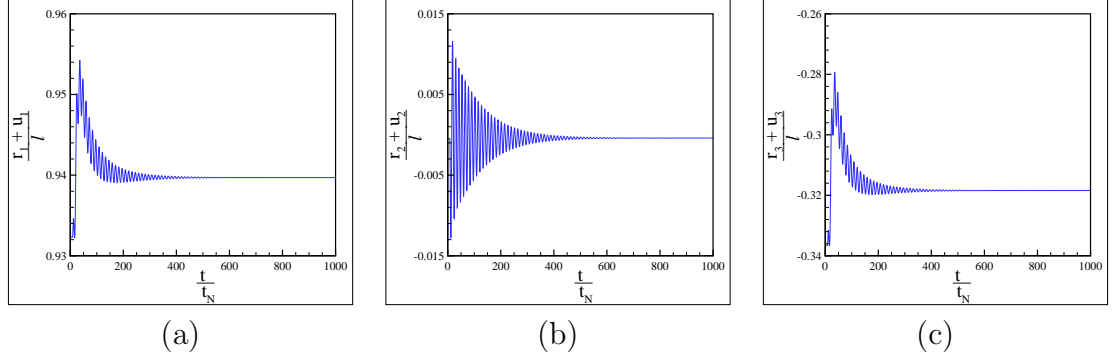
Figure 4.27: Time domain results of wing tip for gun placement at 75% of the span, forward of the reference line ((a):$\frac{r_1+u_1}{l}$ vs. $\frac{t}{t_N}$, (b): $\frac{r_2+u_2}{l}$ vs. $\frac{t}{t_N}$, and (c): $\frac{r_3+u_3}{l}$ vs. $\frac{t}{t_N}$) [64].
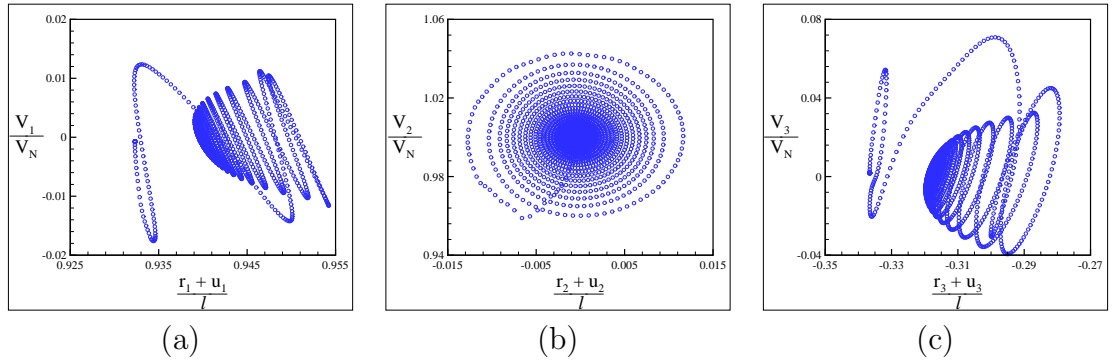
Figure 4.28: Time domain results of wing tip for gun placement at 75% of the span, forward of the reference line ((a): $\frac{V_1}{V_N}$ vs. $\frac{r_1+u_1}{l}$, (b): $\frac{V_2}{V_N}$ vs. $\frac{r_2+u_2}{l}$, and (c): $\frac{V_3}{V_N}$ vs. $\frac{r_3+u_3}{l}$) [64].
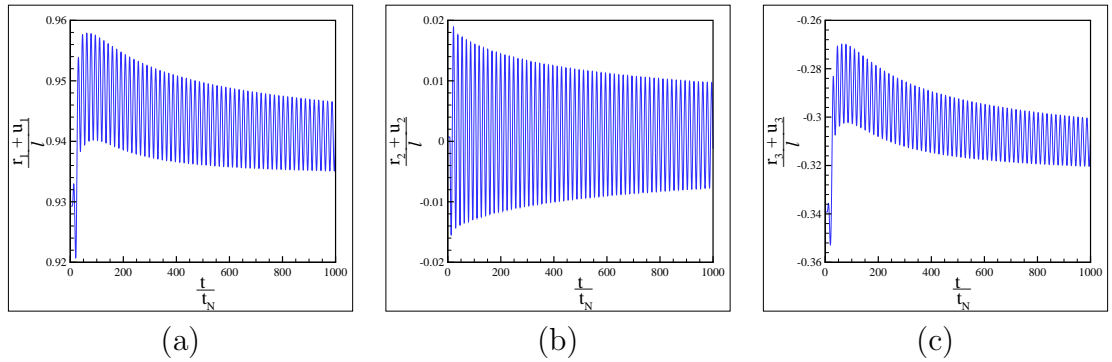
Figure 4.29: Time domain results of wing tip for gun placement at the tip of the wing, with no offset ((a):$\frac{r_1+u_1}{l}$ vs. $\frac{t}{t_N}$, (b): $\frac{r_2+u_2}{l}$ vs. $\frac{t}{t_N}$, and (c): $\frac{r_3+u_3}{l}$ vs. $\frac{t}{t_N}$) [64].

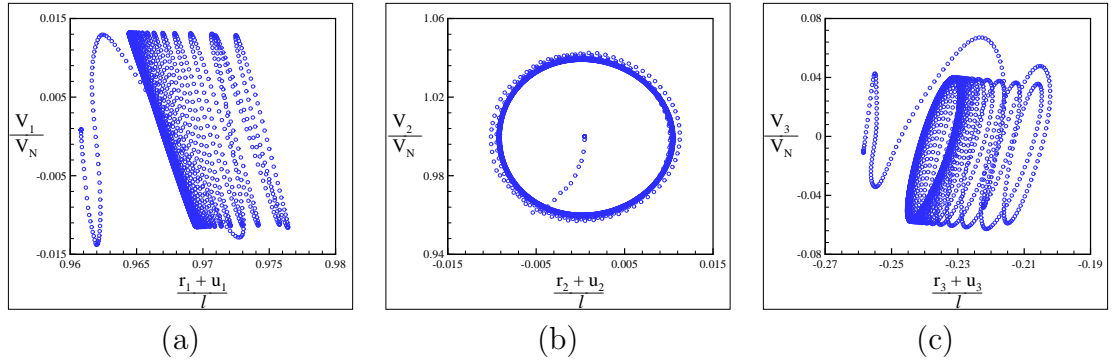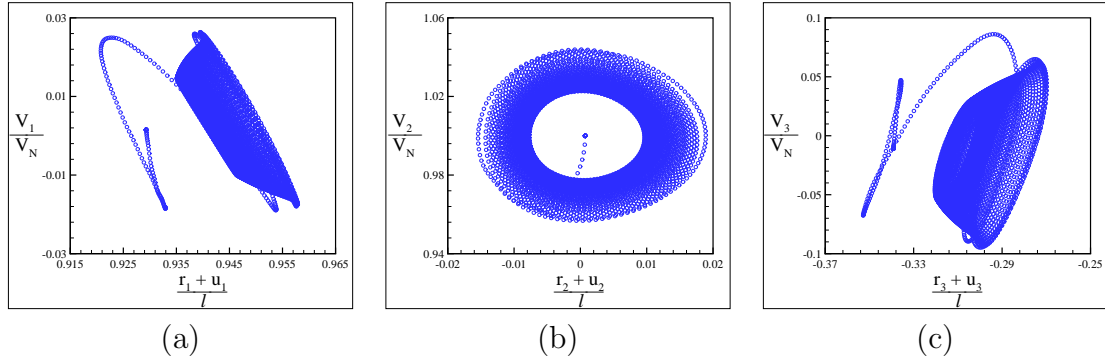Figure 4.30: Time domain results of wing tip for gun placement at the tip of the wing, with no offset ((a): $\frac{V_1}{V_N}$ vs. $\frac{r_1+u_1}{l}$, (b): $\frac{V_2}{V_N}$ vs. $\frac{r_2+u_2}{l}$, and (c): $\frac{V_3}{V_N}$ vs. $\frac{r_3+u_3}{l}$) [64].

CHAPTER 5

CONSTRUCTAL APPROACH IN DESIGN OF HALE AIRCRAFT

5.1 Background

The chief objective of this chapter is to explore and explain the reasoning behind the changes in the flutter speed of different flying wing aircraft configurations. So far, I presented the effects of different design parameters on the aeroelastic stability. Here, I try to explain why these changes have occurred. This phenomena can be explained based on the constructal law [5] and concept of flow of stresses [12, 57]. Constructal law and design with constructal theories are capable of explaining, analyzing, and predicting the generation of energy flow configuration [67].

Investigating the evolution of airplanes through the lens of constructal law reveals that "they obey theoretical allometric rules that unite them with the birds and other animals. For example, larger airplanes should be faster, more efficient vehicles, and have a greater flying range. Large or small, airplanes should exhibit a proportionality between wingspan and fuselage length, and between fuel load and body size" [9].

Engines characteristics such as size, trust, weight, etc. can make a tremendous difference in efficiency and stability of different types of aircraft, and the correct choice of design enhances the performance of the vehicle. For instance, engine mass should be proportional to the body size [9, 67], "this scaling is analogous to animal design, where the mass of the motive organs (muscles, heart, lungs) is proportional to the body size" [9].

Lorente et al. [57] proposed the concept of "flow of stresses", by revealing the analogy between heat convection configurations and the flow of stresses in mechanically loaded elastic solid structures. They reported that the structural designs that facilitate the flow of stresses provide the maximum load-carrying capacity.

I invoke constructal law to explain the problem in hand. I explore the differences in the instability boundaries (i.e., flutter speed) of different configurations of aircraft and explain why some of these configurations have higher flutter speed utilizing the concept of "flow of stresses." The flow system is the aircraft structure that carries the flow of stresses. This concept explains that the lighter and stronger configuration is the one that avoids flow strangulation. Here, I seek a stronger aircraft that has a better and smoother flow of stresses [67].

In this chapter, first, the flow of stresses study for a flying wing aircraft with different engine placement is presented. Then, this chapter provides the study of the flow of stresses of swept and curved flying wing aircraft. The stresses are carried out by using the trim state results as the input to the VABS software. The recovery process is explained in chapter 2 section 2.4.

5.2   Effects of Engine Placement on Flow of Stresses

In this section, I seek to find out the possible relation between flutter instability and flow of stresses throughout the wings of flying wing aircraft with different engine placements. The results of the flutter analysis of this aircraft are presented in chapter 3 section 3.4. Accordingly, some extreme cases, including the maximum and minimum areas of flutter speed, are chosen to study the possible relation between the instability and flow of stresses. Moreover, the engines are placed along the span from root to the tip, in order to show how the stresses vary continuously as the configuration is morphed [67].

The first case is the base model in which the engine is placed at the root of the wing. In this case, the flutter occurs at 34.5 m/s. Case 2 is the engine placement at 10% of the span behind the reference line, which is close to the area of minimum

flutter speed. Case 3 considers the engine placement behind the reference line at 20% of the span. This is the area of minimum flutter speed. The flutter speed of this configuration is 24.4 m/s. Cases 4, 5, and 6 are the engine placements at 40%, 60%, and 80% of the span behind the reference line. Case 7 is the engine placement at 80% of the span forward the reference line. This area coincides with the area of maximum flutter speed, which is larger than 100 m/s. The last case is the engine placement at tip behind the reference line [67].

The details of the cases are presented in Table 5.1. These configurations are studied at a cruise speed of 34 m/s. The trim results are then obtained using NATASHA and used as the inputs to VABS [67]. The stresses are obtained for these configurations, and they are presented in Figs. 5.1 – 5.7.

Figure 5.1 shows σ_{11} for cases 1 to 8. Except for case 8, the results for the rest of the cases indicate large magnitudes of stress close to the root of the wings. It is more observable for cases 2, 3, and 4, which are the engine placements in the area of minimum flutter speed. Hence, the result for case 8 shows a very small magnitude of stress. As the flutter speed increases by morphing the configuration, σ_{11} magnitude becomes smaller [67].

The results of σ_{12} are displayed in Fig. 5.2. Cases 1 to 4 are clearly indicating a high concentration of σ_{12} close to the root of the wings. The worst cases of stress concentration are observed at 10% and 20% of the span behind the reference line. Moving the engine toward the tip makes the flow of stress smoother. The smoothest flow of stress is achieved for the engine placement at the area of maximum flutter speed (i.e., 80% of the span forward of the reference line). Additionally, it is worth mentioning that the stresses in cases 2 and 3 have larger magnitudes compared to the rest of the configurations [67].

Case position of engines	Configuration	Flutter speed
Case 1 At the root		34.5 m/s
Case 2 At 10% of the span behind the reference line		25 m/s
Case 3 At 20% of the span behind the reference line		24.4 m/s
Case 4 At 40% of the span behind the reference line		27 m/s
Case 5 At 60% of the span behind the reference line		31.6 m/s
Case 6 At 80% of the span behind the reference line		37 m/s
Case 7 At the tip of the span behind the reference line		42.7 m/s
Case 8 At 80% of the span forward of the reference line		> 100 m/s

Table 5.1: Flutter speed for different engine placements [67].

Figure 5.3 presents the σ_{13} for cases 1 to 8. Although the values of σ_{13} in all the cases are small, it is found that the stresses in cases 2 and 3 are slightly larger,

and also, strangulation of stress flow can be observed in the wings. Figures 5.4 – 5.6 illustrate the results for σ_{22}, σ_{23}, and σ_{33}. The magnitudes of these components of the stress matrix are found to be very small in all the cases compared to σ_{11} and σ_{12}. Thus these components of stress matrix are not significant when the aim is to study the flow of stresses [67].

The Von Mises stresses are shown in Fig. 5.7. For cases 1 to 4, the stresses are substantially larger at the root of the wing, in which the extreme cases are cases 2 and 3. However, as the engine moves toward the tip, the Von Mises decreases. The smallest Von Mises stress is obtained for case 8, which is the engine placement at 80% of the span forward of the reference line. Additionally, the result for the engine placement at the tip behind the reference line (i.e., case 7) shows the stress localization close to the tip and the root of the wings [67].

So far, the stresses results are shown in Figs. 5.1 – 5.7. It is found that case 8 has the smoothest flow of stresses and also the smallest magnitude of stresses. Case 8 presents the configuration in which the engine is placed at 80% of the span forward of the reference line. On the other hand, case 6 represents the engine placement at 80% of the span behind the reference line. Comparing cases 6 and 8 indicates that moving the engine from the trailing edge to the leading edge results in considerable differences in both stability and flow of stresses. Case 8 provides the necessary path for the stresses to flow smoothly, and it avoids strangulation, which leads to a significant extension of the boundary of stability [67].
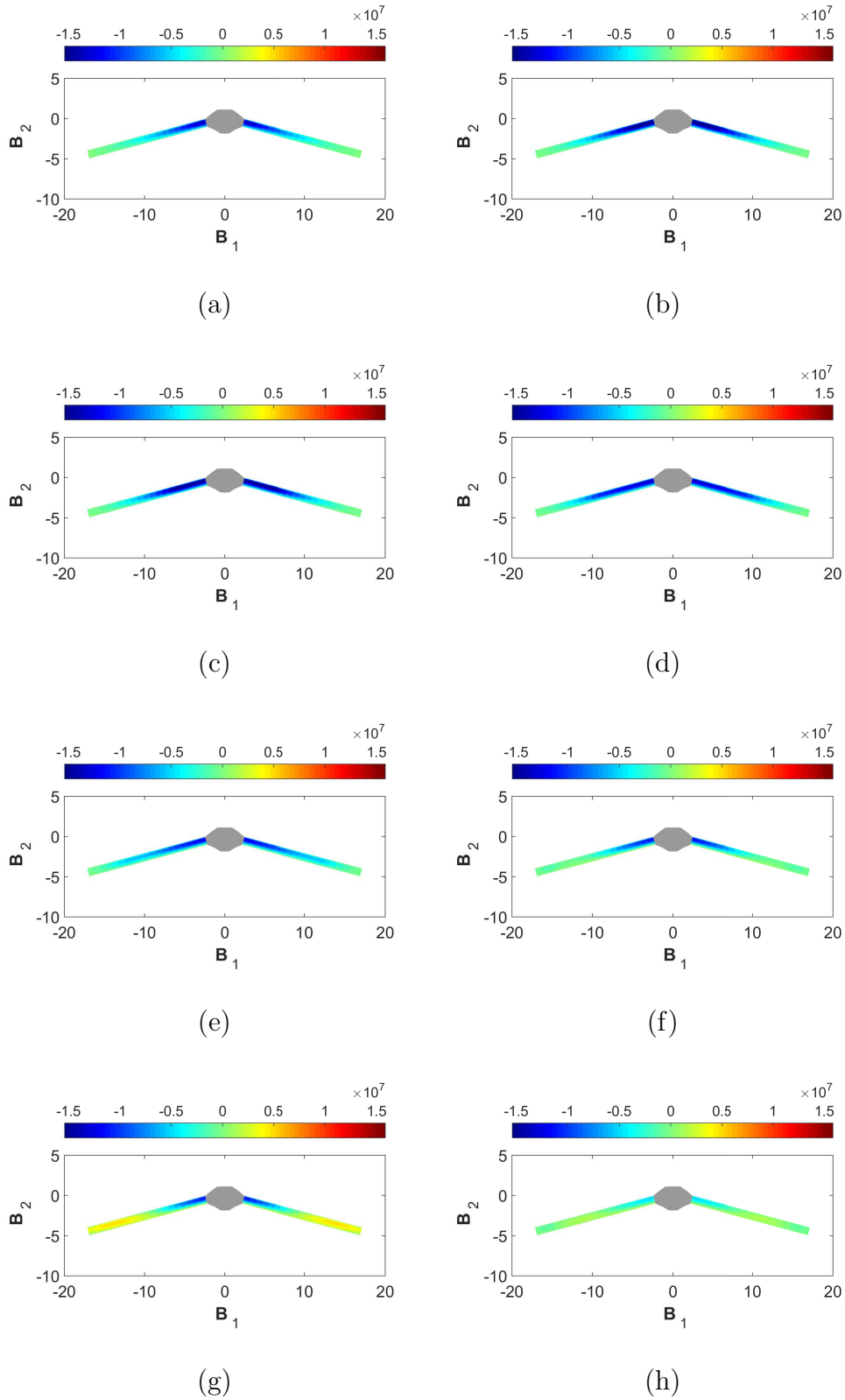
Figure 5.1: Stress distribution along the wing, σ_{11} (Pa): (a) Case 1, (b) Case 2, (c) Case 3, (d) Case 4, (e) Case 5, (f) Case 6, (g) Case 7, and (h) Case 8 [67].
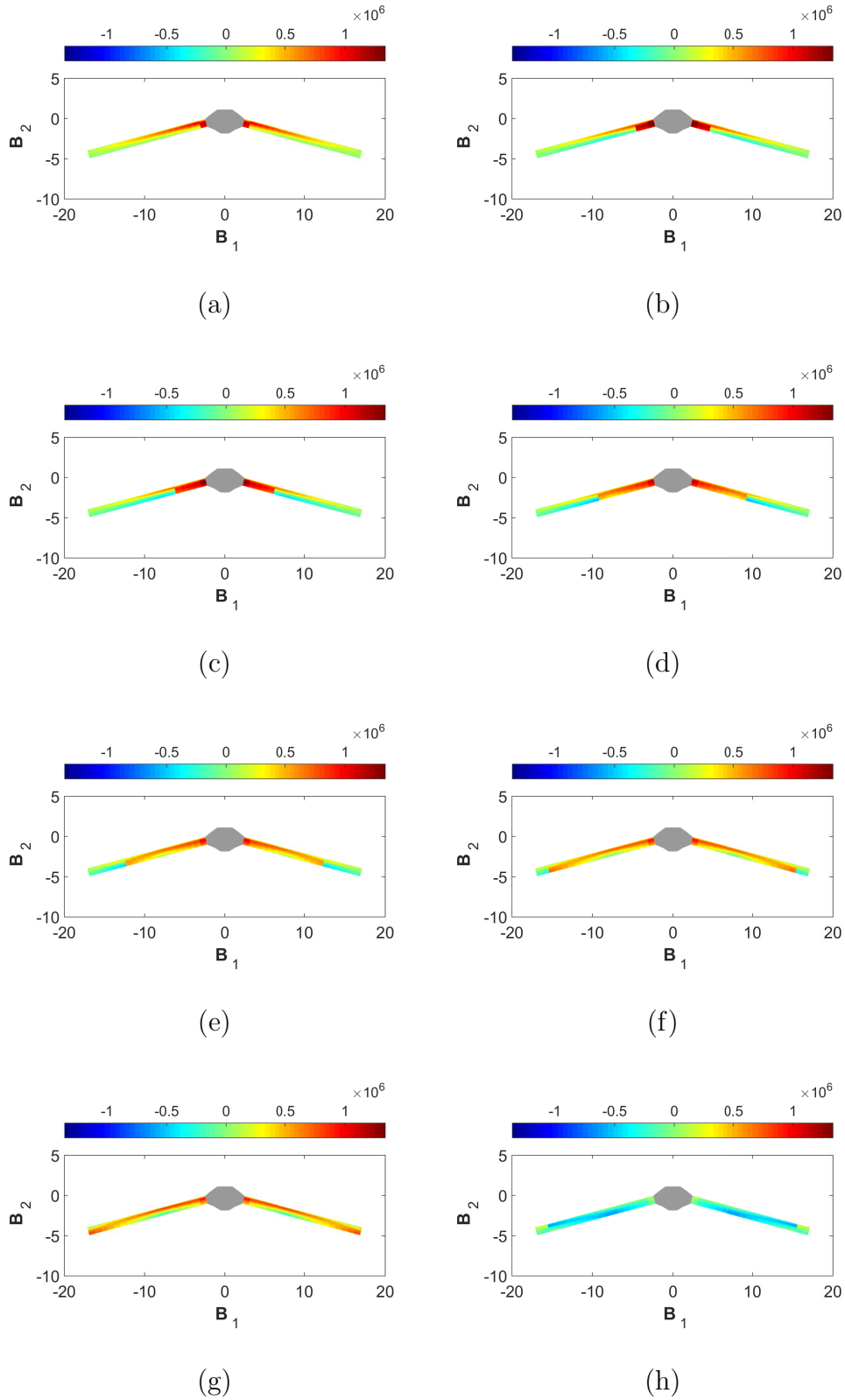
Figure 5.2: Stress distribution along the wing, σ_{12} (Pa): (a) Case 1, (b) Case 2, (c) Case 3, (d) Case 4, (e) Case 5, (f) Case 6, (g) Case 7, and (h) Case 8 [67].

70
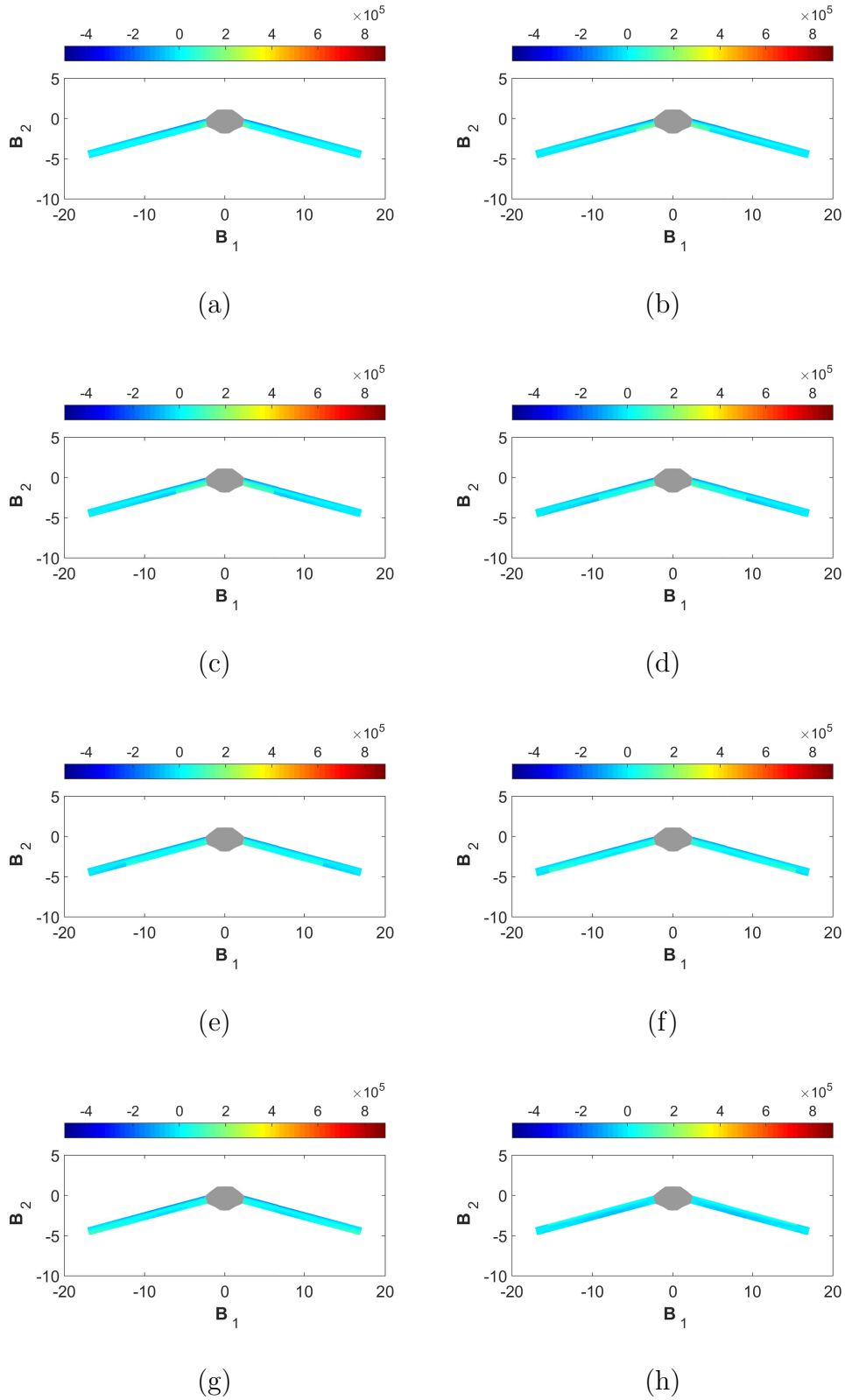
Figure 5.3: Stress distribution along the wing, σ_{13} (Pa): (a) Case 1, (b) Case 2, (c) Case 3, (d) Case 4, (e) Case 5, (f) Case 6, (g) Case 7, and (h) Case 8 [67].
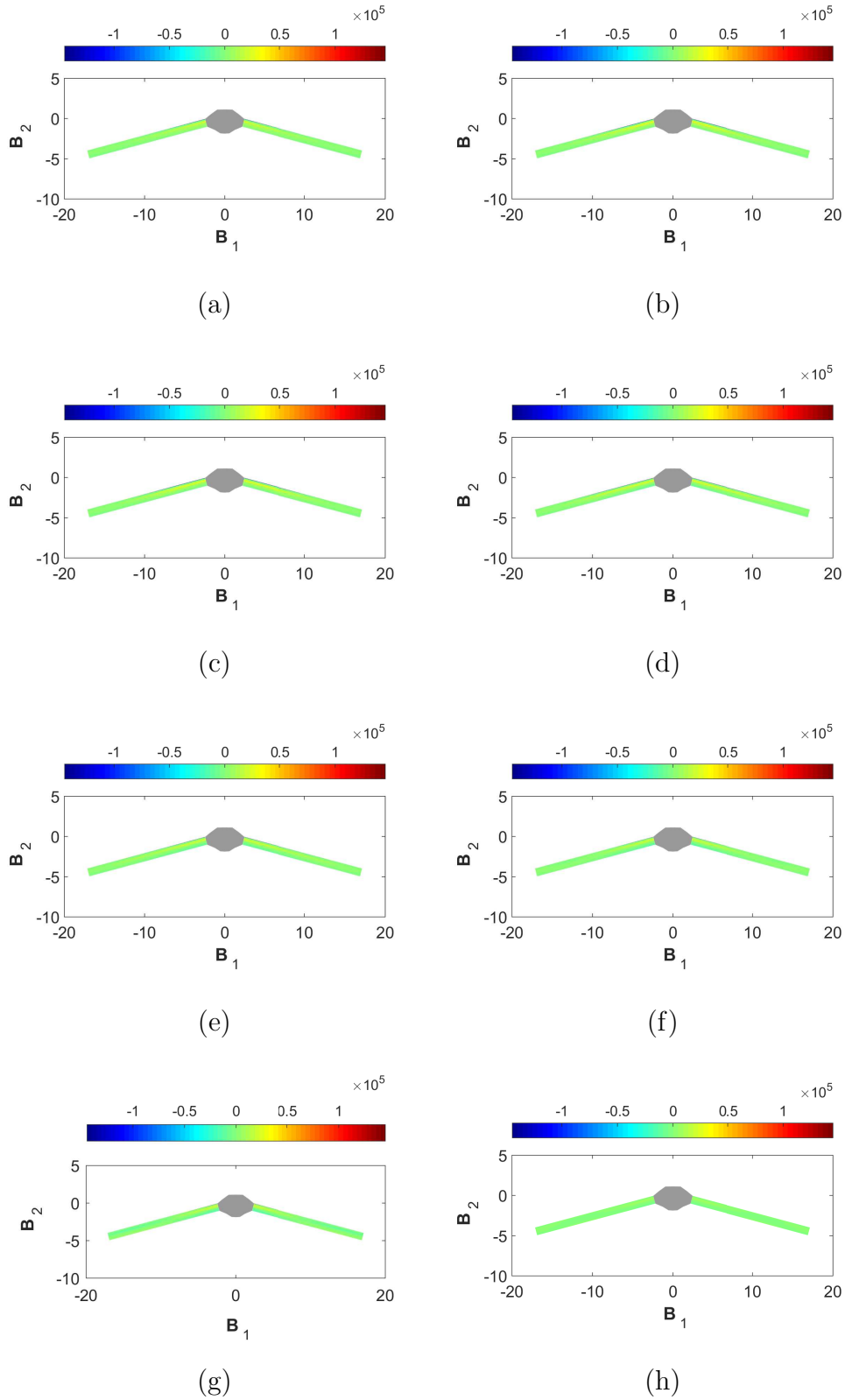
Figure 5.4: Stress distribution along the wing, σ_{22} (Pa): (a) Case 1, (b) Case 2, (c) Case 3, (d) Case 4, (e) Case 5, (f) Case 6, (g) Case 7, and (h) Case 8 [67].
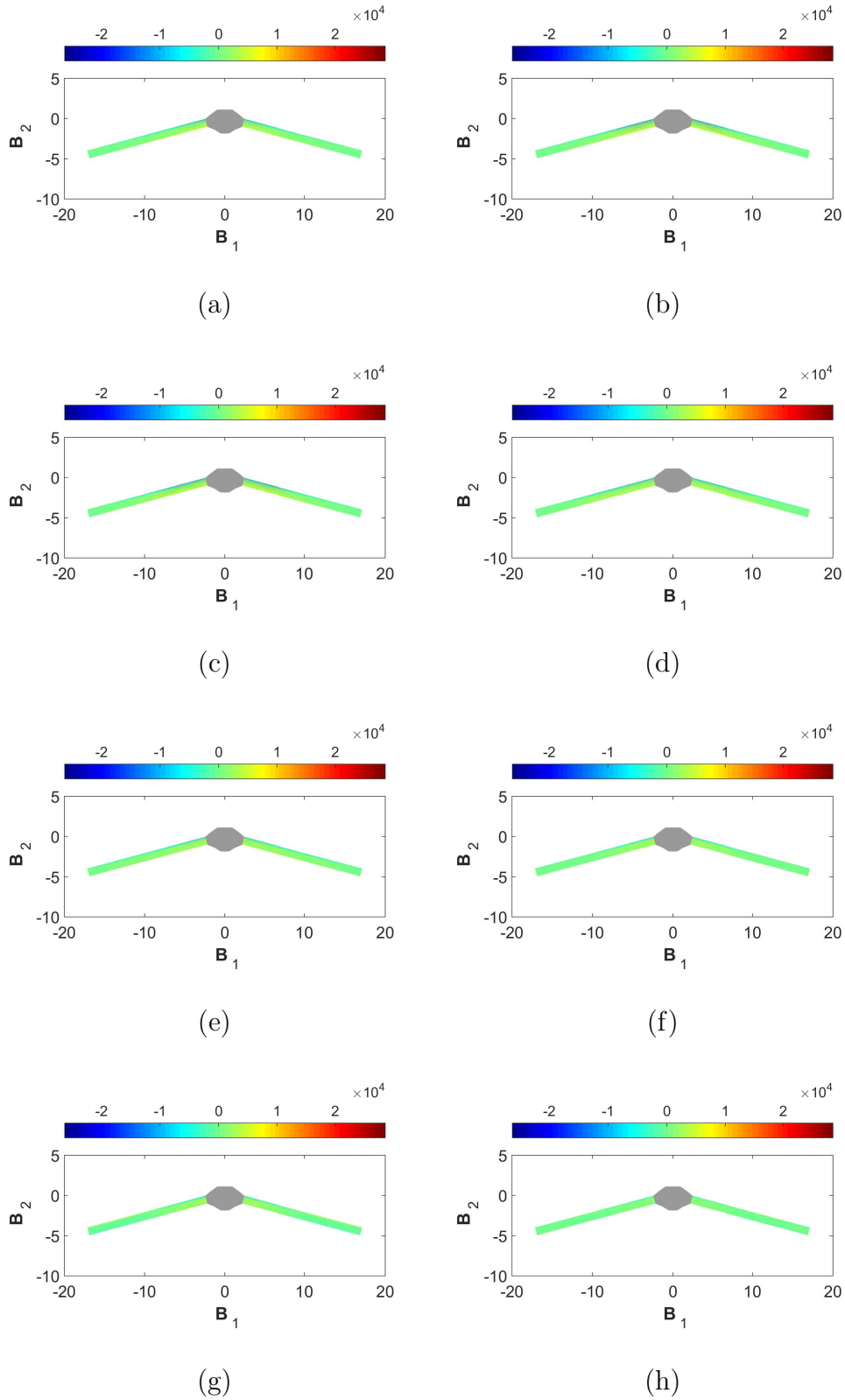
Figure 5.5: Stress distribution along the wing, σ_{23} (Pa): (a) Case 1, (b) Case 2, (c) Case 3, (d) Case 4, (e) Case 5, (f) Case 6, (g) Case 7, and (h) Case 8 [67].

73
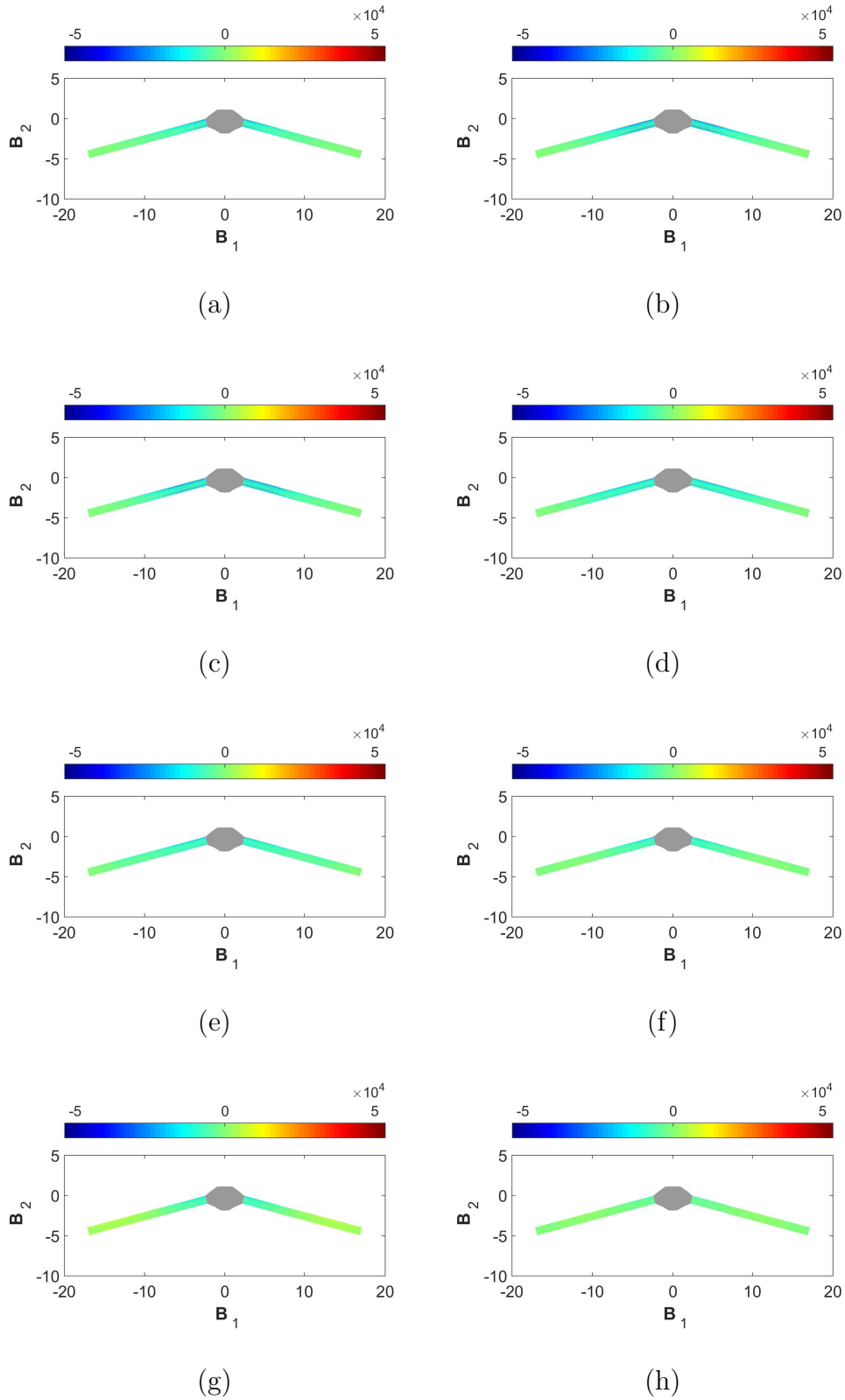
Figure 5.6: Stress distribution along the wing, σ_{33} (Pa): (a) Case 1, (b) Case 2, (c) Case 3, (d) Case 4, (e) Case 5, (f) Case 6, (g) Case 7, and (h) Case 8 [67].
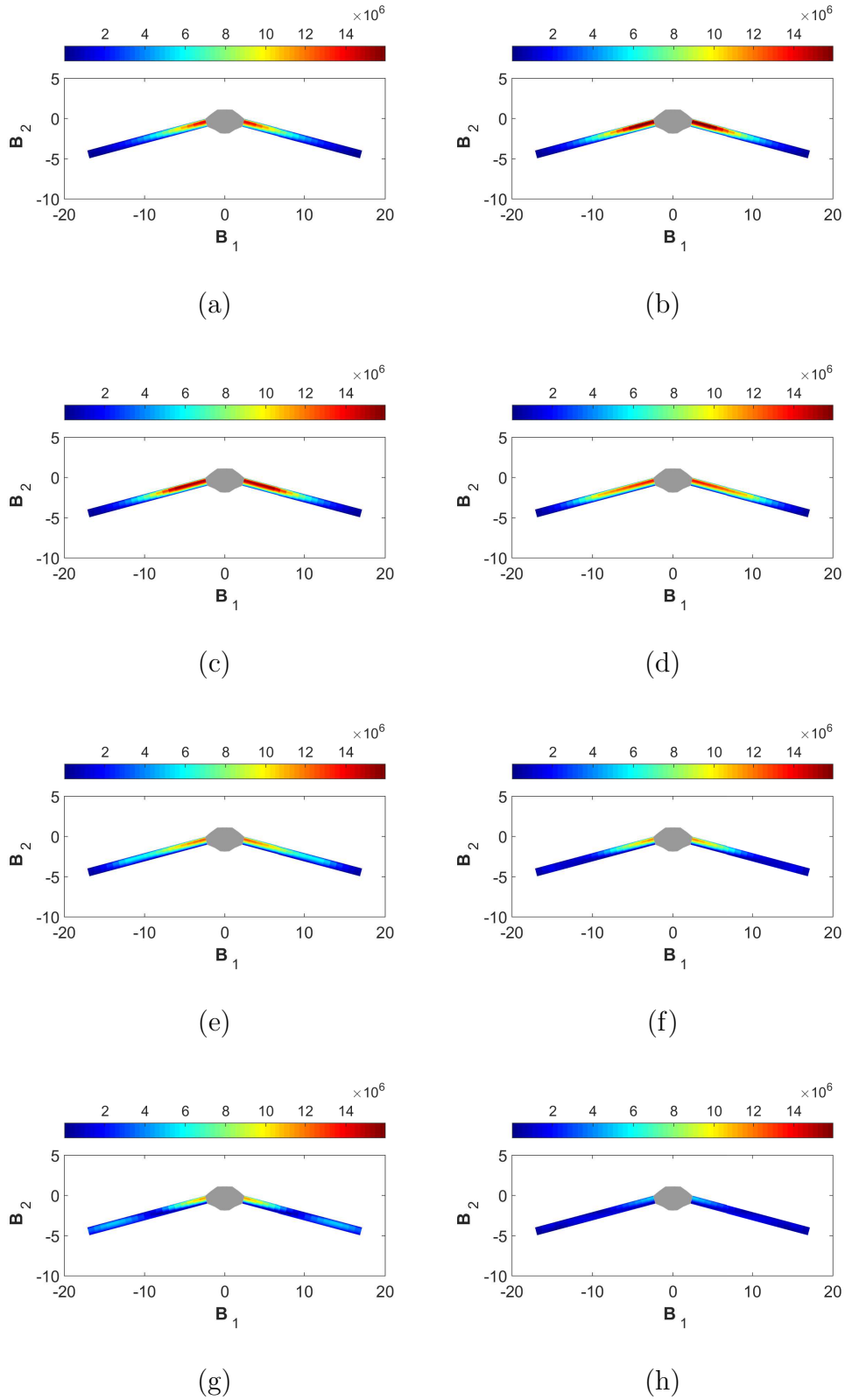
Figure 5.7: Distribution of Von Mises stresses along the wing (Pa): (a) Case 1, (b) Case 2, (c) Case 3, (d) Case 4, (e) Case 5, (f) Case 6, (g) Case 7, and (h) Case 8 [67].

5.3 Flow of Stresses in Curved and Swept Configuration

In this section, the results of stability and stress analysis of the curved and swept flying wing are presented to investigate the analogy between stability and flow of stresses of these two designs. The details of these configurations are presented in chapter 3 section 3.5. First, I consider three sweep and three curvature angles to investigate how the stability and stress flow vary with changing the sweep and curvature angles. These configurations are trimmed at 40 m/s. Second, I investigated the effects of trim condition on the flow of stresses. In this case, I obtained the results of base model configurations (i.e., one configuration with 15-degree sweep and one configuration with 30-degree curvature) at 30 m/s cruise speeds. Finally, the last part of our study aimed to assess the stresses flow distribution of the base model configurations under equal load distribution. In order to do so, a concentrated mass is added to the reference node of the aircraft on the fuselage. The offset of the concentrated mass is chosen in a way that it results in equal flap deflection at the same cruise speed [46].

5.3.1 Effects of sweep and curvature variation

In this section, three different cases are discussed. Case I is the comparison between two flying wing aircraft; one has wings with a 15-degree sweep angle and one with 30-degree curvature. Case II includes two configurations, one with 17.5-degree swept wings and one with 35-degree curved wings. Finally, case III offers two designs; one with 20-degree swept wings and the other one with 40-degree curved wings [46]. The flutter characteristics of these cases are available in Table 3.9 chapter 3 section 3.5.

To perform the stress analysis, all the configurations are trimmed at a cruise speed of 40 m/s. The internal forces in $\mathbf{b}_3$ direction at 40 m/s cruise speed for

all three cases are available in Fig. 5.8. At this value of the cruise speed, which is below the flutter speed of all configurations, the internal force associated with the curved geometry has higher magnitudes almost throughout half of the span. This component of the internal force represents the forces in $\mathbf{b}_3$ direction, including lift and weight. Since the weights of both structures are almost equal, it is concluded that the curved geometry produces a higher lift force. It is shown in the literature that when the structure experiences a larger component of the airflow, the flutter speed decreases [43]. The same phenomena are happening here, the area closer to the fuselage of the curved aircraft is exposed to larger components of the airflow [46].
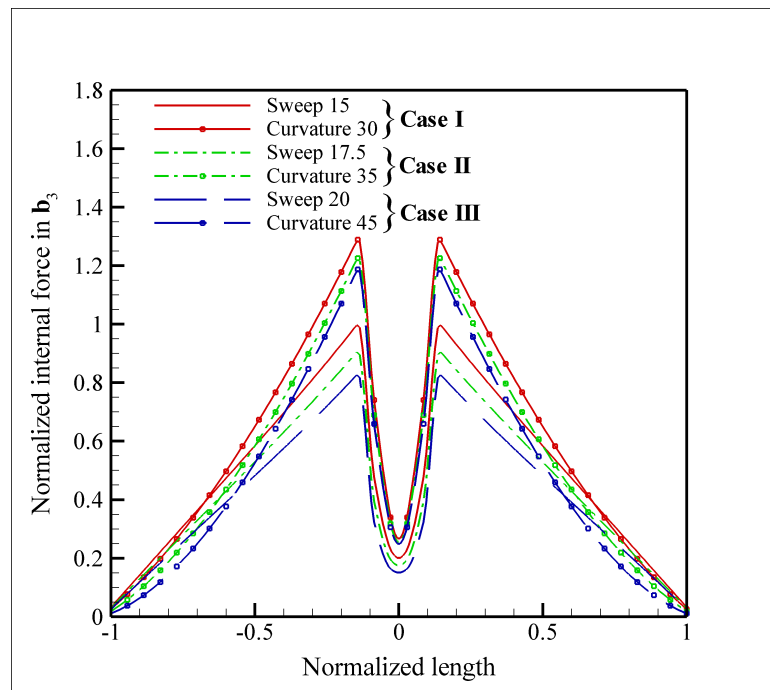
Figure 5.8: Normalized internal force in $\mathbf{b}_3$ direction for cases I, II, and III; cruise speed= 40 (m/s) [46].

The trimmed results at this cruise speed are used to recover the stresses using VABS software. The patterns and magnitudes of the flow of stresses are presented in

Figs. 5.9– 5.12. The components of the stress matrix are plotted, and the significant ones are illustrated and discussed here. The first component of the stress matrix σ_{11} (see Fig. 5.9) shows that all cases are experiencing compression at the upper surface of the wings. The magnitudes of σ_{11} decline as the sweep and curvature increases. Comparing σ_{11} distribution between curved and swept configuration of each case shows no sensible difference in the σ_{11} distribution [46].
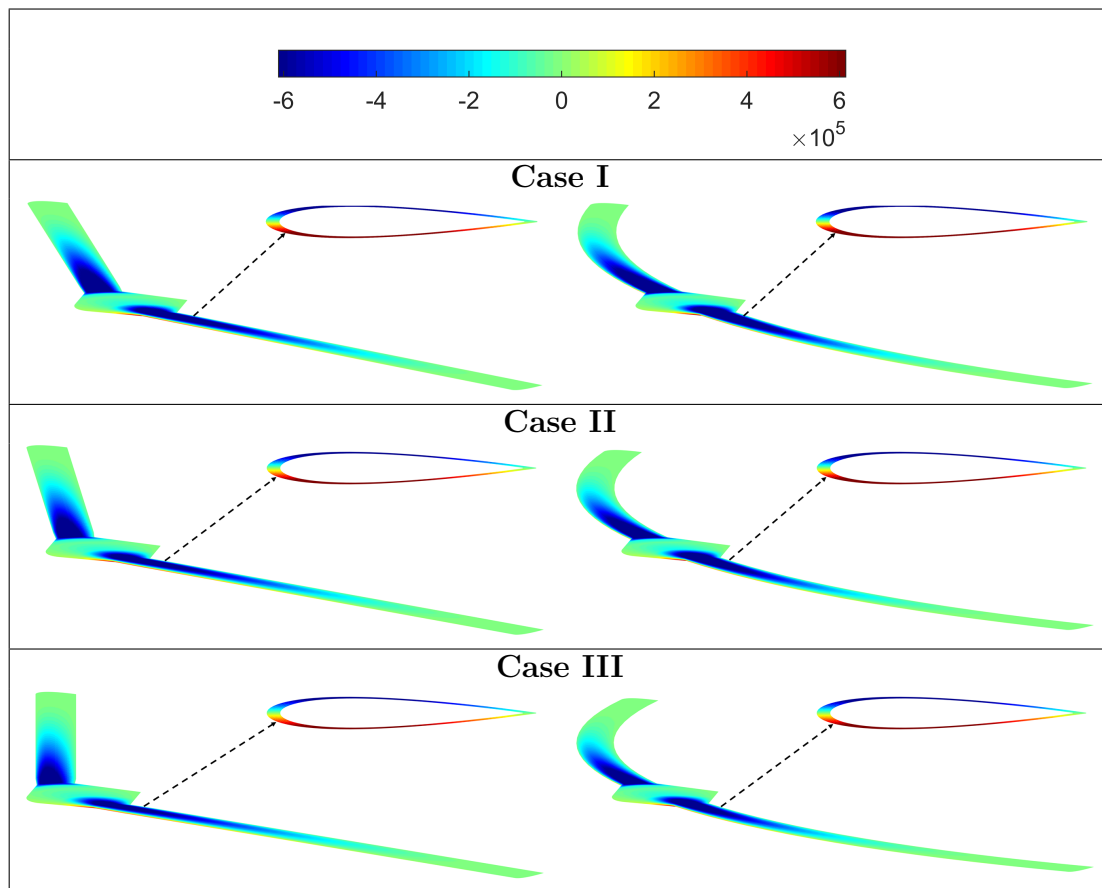
Figure 5.9: σ_{11} (Pa) distribution of cases I, II, and III; cruise speed= 40 (m/s) [46].

On the contrary, σ_{12} in Fig. 5.10 depicts completely different distribution throughout the wings and airfoil of the swept and curved aircraft. While in the swept configuration σ_{12} changes from root to tip smoothly, the curved model shows stress

strangulation at the trailing edge of the root of the wings as well as the leading edge of mid-span of the wings [46].
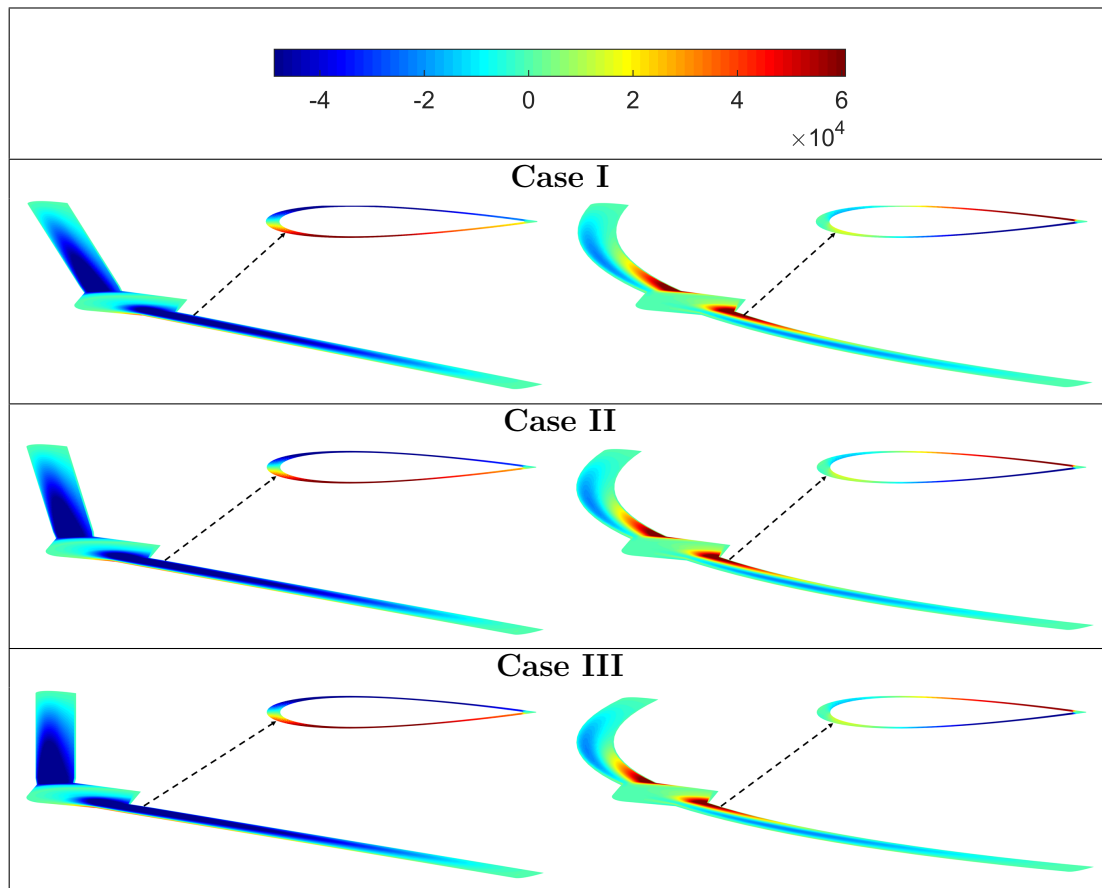
Figure 5.10: σ_{12} (Pa) distribution of cases I, II, and III; cruise speed= 40 (m/s) [46].

Figure 5.11 depicts the σ_{13} distribution on the wings and airfoils of all six configurations. High concentrations of σ_{13} can be observed at the leading edge of the swept aircraft, whereas the curved aircraft has a smoother distribution of σ_{13}. However, comparing the magnitude of this component of stress, it is notable that it is almost two orders of magnitude smaller than σ_{11} and one order of magnitude smaller than σ_{12} [46].
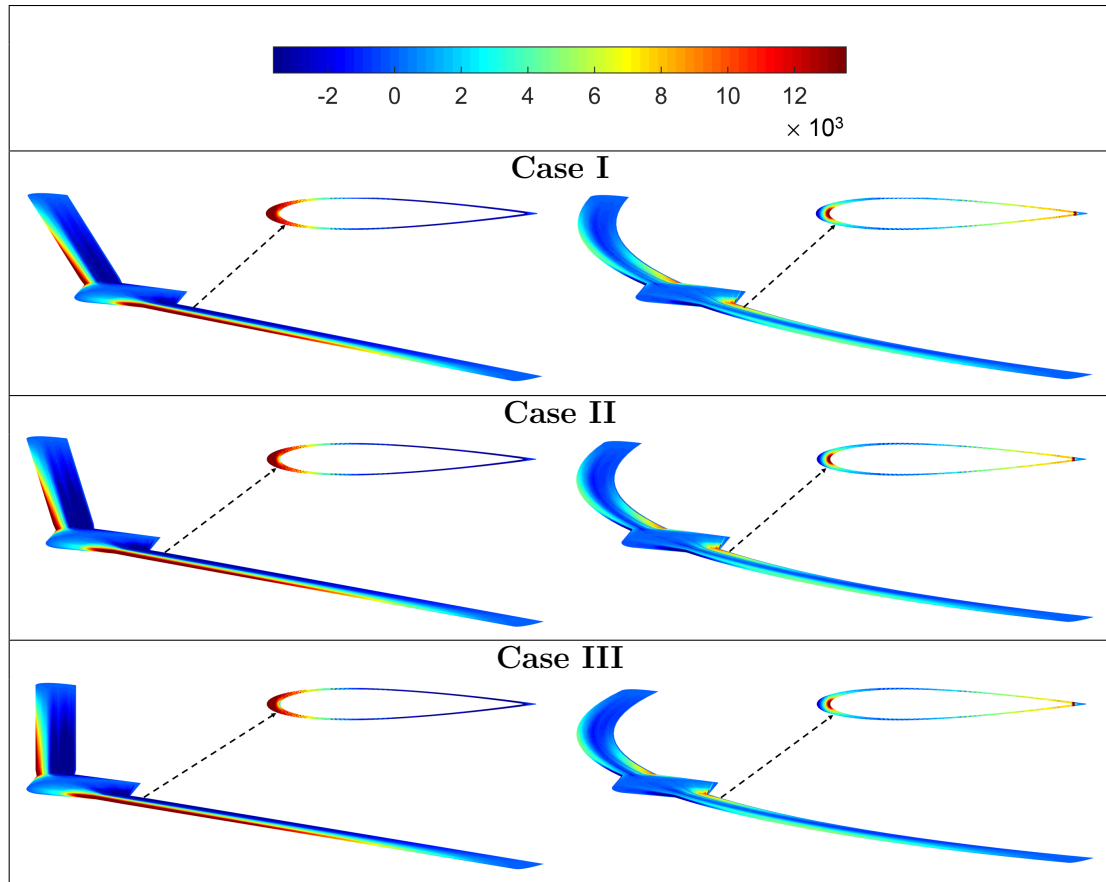
Figure 5.11: σ_{13} (Pa) distribution of cases I, II, and III; cruise speed= 40 (m/s) [46].

Furthermore, the results of the Von Mises stress are shown in Fig. 5.12. The Von Mises stress shows larger magnitudes in the curved wing aircraft compared to swept wings. This can be explained by the fact that this configuration is under larger loads (see Fig. 5.8). Von Mises also decreases as the sweep and curvature angle increases. Figure. 5.8 shows that swept and curved configurations with larger angles have lower magnitudes of internal forces [46].
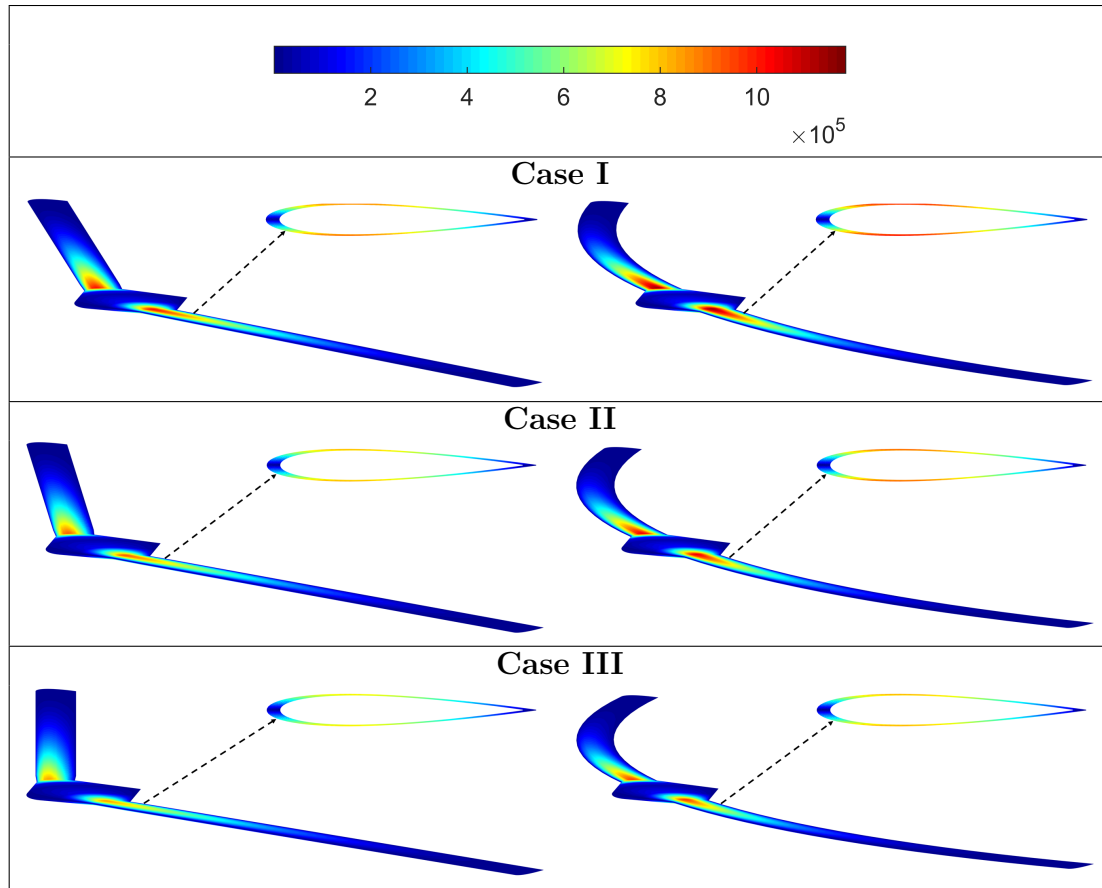
Figure 5.12: Von Mises stress (Pa) distribution of cases I, II, and III; cruise speed= 40 (m/s) [46].

5.3.2   Trim condition and flow of stresses

In the previous section, I analyzed the stress distributions at the cruise speed of 40 m/s. To asses the effects of a different trim condition on the characteristics of the flow of stresses, the cruise speed is set equal to 30 m/s for the base model aircraft [46].

The internal forces , as presented in Fig. 5.13, are not experiencing significant changes compared to the cruise speed of 40 m/s, and it shows that the curved flying wing is subjected to larger magnitudes of internal force [46].

The results of stress analysis at the cruise speed of 30 m/s are available in Figs. 5.14– 5.17. The flow of stresses demonstrates the same characteristics as the results for a cruise speed of 40 m/s, Figs. 5.9– 5.12 [46].

The first component of the stress matrix σ_{11} shows that both configurations are experiencing compression at the upper surface of the wings, while the stress strangulation could still be observed in curved configuration as shown in Fig. 5.10 for σ_{12}, and for the swept configuration as shown in Fig. 5.11 for σ_{13}. Similar to the results of Fig. 5.12, the Von Mises stress shows larger magnitudes in the curved wing aircraft [46].

This shows that differences in the characteristics of the flow of stresses and their pattern of distribution are not a function of trim condition, but it solely depends on the geometry and shape of the structure [46].
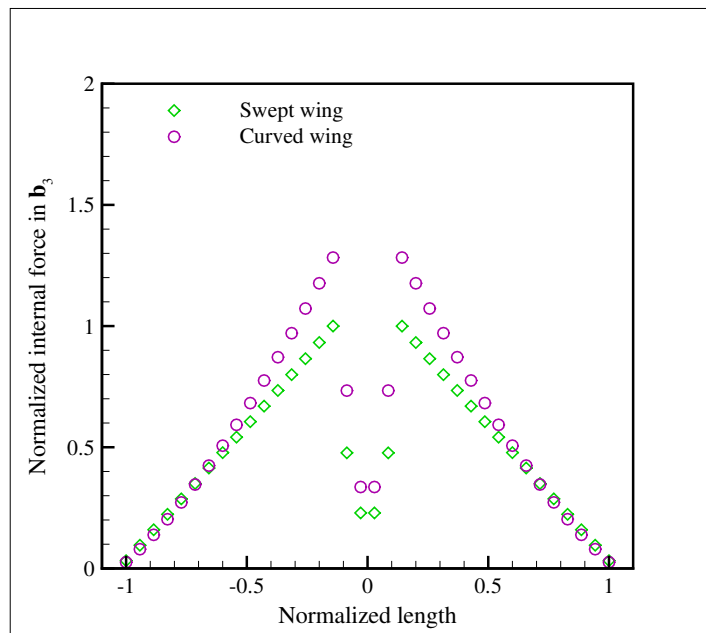
Figure 5.13: Normalized internal force of base model configurations (i.e., case I) in $\mathbf{b}_3$ direction; cruise speed= 30 (m/s) [46].
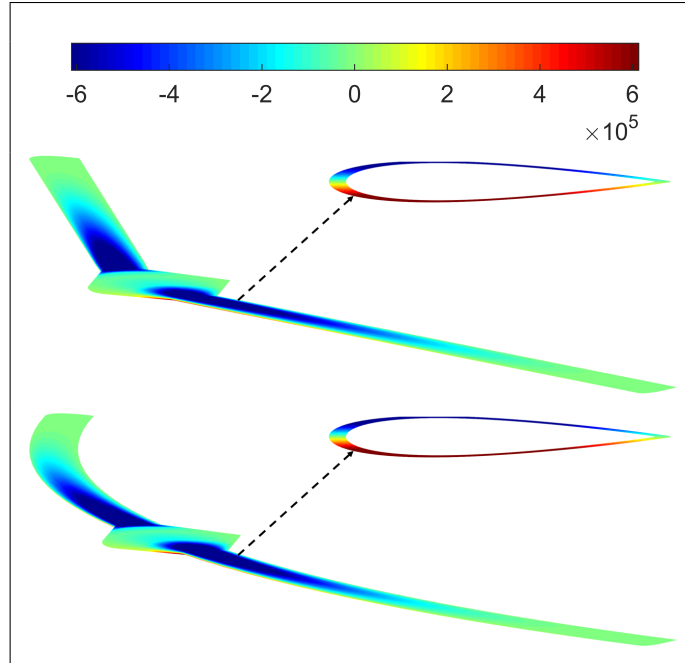
Figure 5.14: σ_{11} (Pa) distribution of base model configurations (i.e., case I); cruise speed= 30 (m/s) [46].
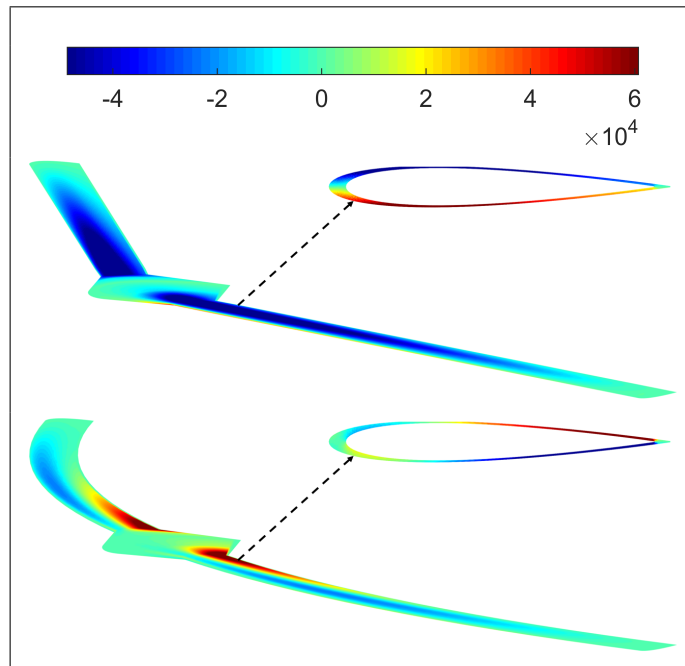
Figure 5.15: σ_{12} (Pa) distribution of base model configurations (i.e., case I); cruise speed= 30 (m/s) [46].
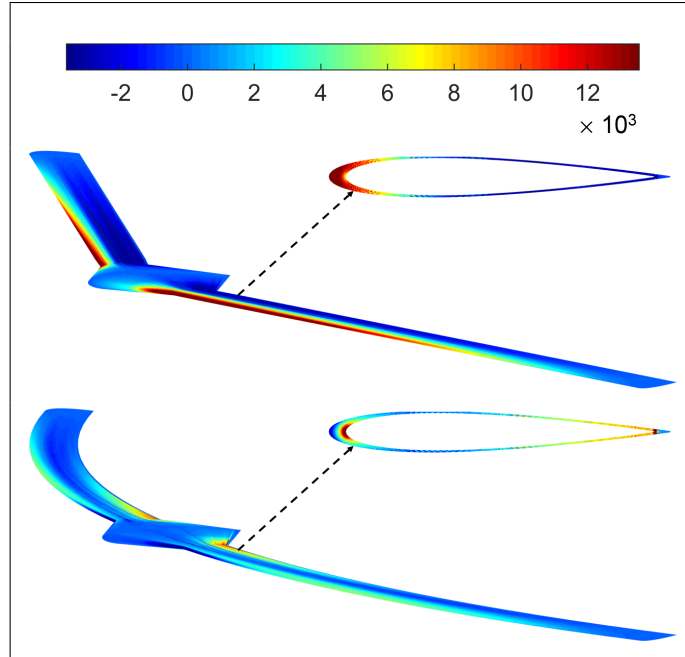
Figure 5.16: σ_{13} (Pa) distribution of base model configurations (i.e., case I); cruise speed= 30 (m/s) [46].
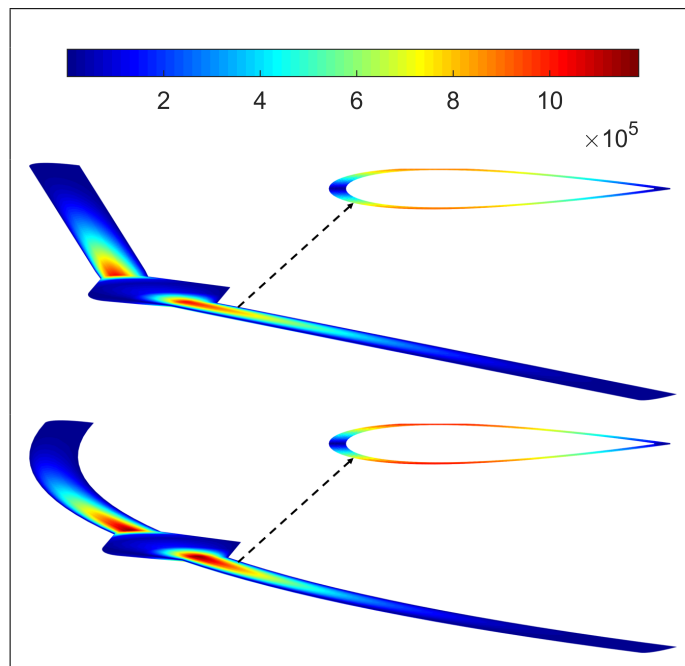
Figure 5.17: Von Mises stress (Pa) distribution of base model configurations (i.e., case I); cruise speed= 30 (m/s) [46].

5.3.3 Equally distributed aerodynamic loading

In previous sections, it was observed in Figs. 5.8 and 5.13 that swept and curved aircraft experience different loading conditions. To expose these configurations to the same loading condition, a concentrated mass is added in the plane of the symmetry of the aircraft with different offsets. The concentrated mass is equal to 10 kg. The offset for the curved aircraft is 0.6 forward of the reference line and 0.8 behind the reference line for the swept configuration. These values result in equal flap deflections for both configurations [46].

This change in the structures significantly affects their stability. The flutter speed of both cases decreases, as shown in Table 5.2, while the impact on the swept case is more significant. Still, the flutter speed of the swept aircraft is larger than the curved configuration but only by 9%. Moreover, the internal force in $\mathbf{b}_3$ direction, as illustrated in Fig. 5.18, changes substantially compared to previous cases. Here, the internal force in $\mathbf{b}_3$ direction for curved and swept flying wing aircraft has the same magnitudes and patterns of distribution [46].

For the case of the equal flap deflection, the stresses analysis is presented in Figs. 5.19– 5.22. The stress distribution patterns remain the same as in previous cases. However, it is apparent that the magnitudes are different. It is observable from Figs. 5.20 that the blue area at the leading edge of the curved wing has substantially higher magnitudes compare to Figs. 5.10, and 5.15. For the swept-wing aircraft, the blue color, which represents higher magnitudes of stresses, is covering a larger area of the span compared to previous cases. The same is true for σ_{13}, in Fig. 5.21 [46].

For the curved wing configuration, the stresses strangulation at the leading edge of the aircraft has higher magnitudes compared to the previous cases (i.e., Figs. 5.11, and 5.16). Additionally, for the σ_{13} of the swept wing, the stress concentration is observed at the leading edge extends to areas closer to the tip of the wings. The Von

Mises stress distribution presented in Figs. 5.22 highlights the higher magnitudes of the stresses more clearly. The area close to the root has significantly higher magnitudes of the Von Mises stress compared to Figs. 5.12 and 5.17 [46].
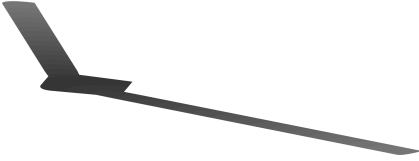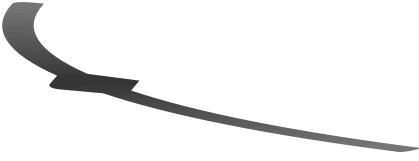
Aircraft	Flutter Speed (m/s)	Flutter frequency (rad/s)
	44.2	11.7
	40.5	10.4

Table 5.2: Flutter speed and frequency of base model configurations (i.e., case I) with a concentrated mass [46].
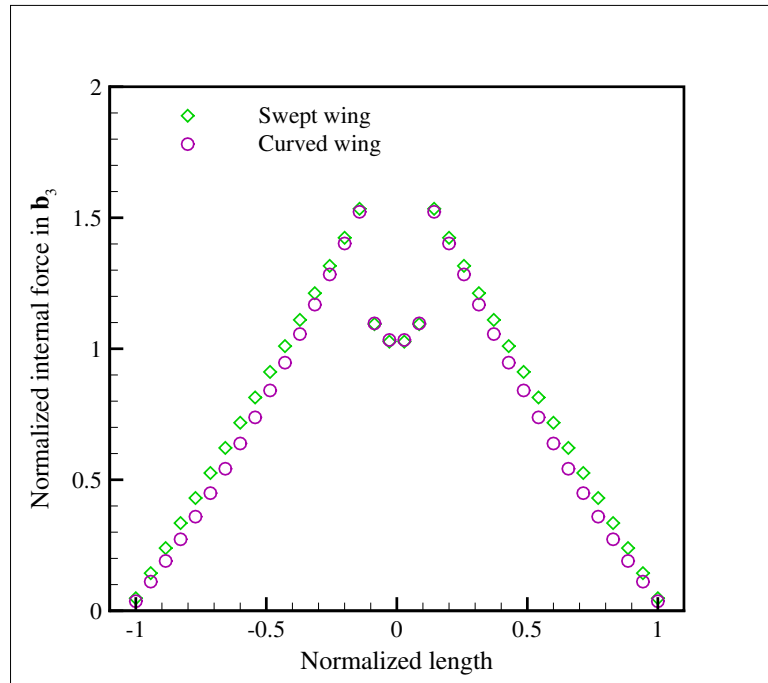
Figure 5.18: Normalized internal force of base model configurations (i.e., case I) in $\mathbf{b}_3$ direction with a concentrated mass; Cruise speed = 40 (m/s) [46].
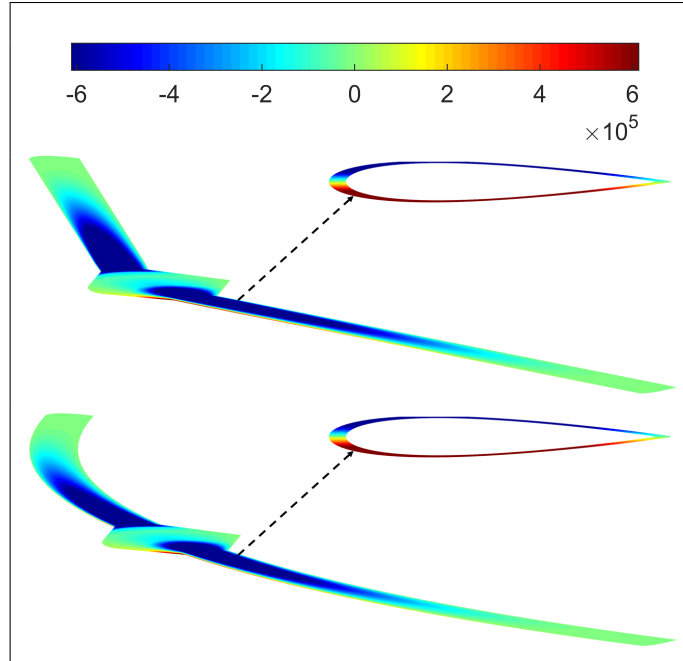
Figure 5.19: σ_{11} (Pa) distribution of base model configurations (i.e., case I) with a concentrated mass; cruise speed = 40 (m/s) [46].
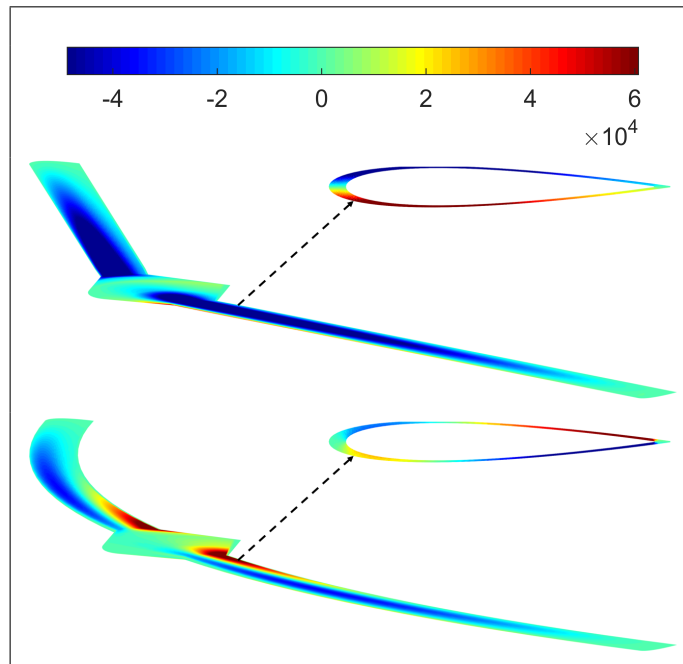
Figure 5.20: σ_{12} (Pa) distribution of base model configurations (i.e., case I) with a concentrated mass; cruise speed = 40 (m/s) [46].
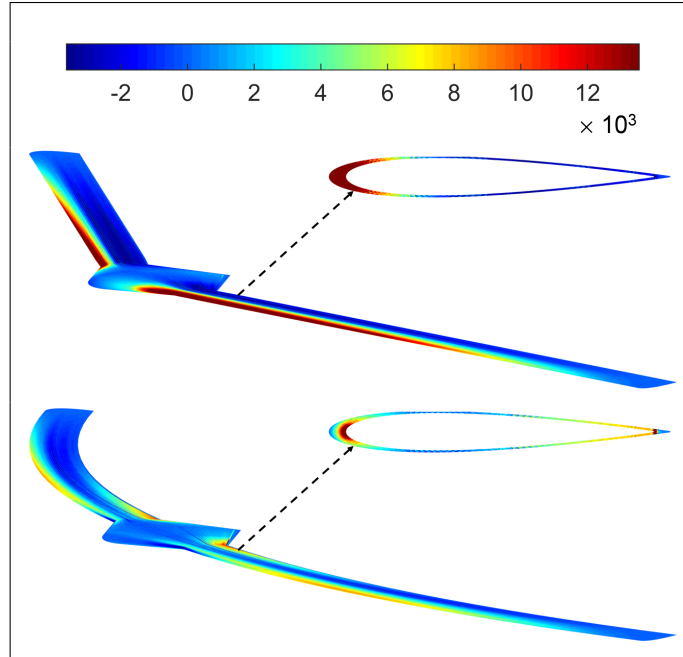
Figure 5.21: σ_{13} (Pa) distribution of base model configurations (i.e., case I) with a concentrated mass; cruise speed = 40 (m/s) [46].
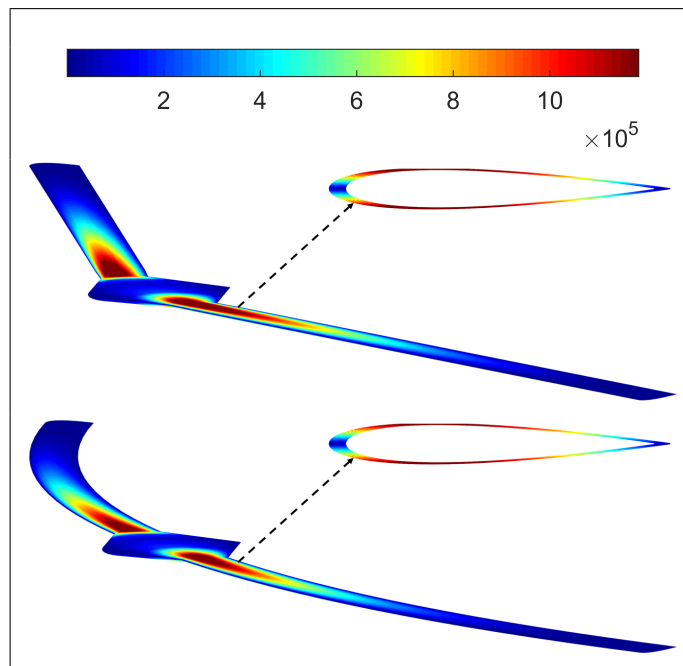
Figure 5.22: Von Mises stress (Pa) distribution of base model configurations (i.e., case I) with a concentrated mass; cruise speed = 40 (m/s) [46].

CHAPTER 6

CONCLUSION

Summary and Discussion

Changes in the design parameters of an aircraft affect its static and dynamic aeroelastic instability significantly. This study considers a variety of design parameters and their effects on the nonlinear aeroelastic response of HALE aircraft. I presented the effects of engine placement, armament placement, sweep, and curvature on aeroelastic stability and flow of stresses of HALE aircraft.

This research is conducted using three computer programs; Gmsh, VABS, and NATASHA. Gmsh provides geometry and mesh. VABS uses the geometry and mesh to calculate the structural properties. NATASHA utilizes the structural properties to assess the aeroelastic trim and stability. Finally, VABS uses the trim solution to recover the stress distribution.

To solve the problem of aeroelastic instability in HALE aircraft, we must first address the root aeroelastic problems. While studies [18, 31, 83] agree that during flutter system absorbs energy from the airstream, there is no discussion on how the energy flow configuration is involved in flutter phenomenon. Here, I used constructal law to explore the configuration of the flow system and explain the analogy between the flow of stresses and aeroelastic instability.

The nonlinear aeroelastic responses are investigated when the structure is exposed to gust and blast loads. The results indicate that a correct choice of engine or armament placement can suppress undesirable responses. The gust loads with light, moderate, and severe intensities are applied to the aircraft in the time domain when the aircraft is cruising at 50 m/s. The results indicate that when the engines are mounted at the root of the wings, large oscillations exist, which their amplitude

increase as the intensity of the gust loads increase. On the contrary, for all of the gust loads, when the engines are located at 60% of the span forward of the reference line, the oscillations suppress. I also showed that for a cantilever wing gust responses are suppressed when the engines are mounted at the area of maximum flutter speed.

The physics of shooting, including the combined effect of a concentrated mass release (bullet), a local blast-induced gust, and an impulse on the wing are investigated. The comparison of the results of frequency domain analysis and the time domain analysis yielded the conclusion that when the wings are subjected to untimely blast forces accompanied with constant impulsive forces generated due to shooting of bullets, it becomes necessary to place the armaments in a suitable location, which is found to be close to the root or at 75% of the span forward of the reference line. Apparently, the area of maximum flutter speed is a suitable area for placement of armament as well as an engine that can suppress the responses due to a different kind of excitation. However, the armament also is safe to be mounted close to the root of the wing.

Extensive literature exists and shows that the arrangement of any stores (e.g., engines) on the aircraft affects the stability [28, 30, 33, 59, 62, 63, 68, 72, 73, 96]. Here, I took this a step further and demonstrated that when the arrangement of engines on the wing changes, the stress flow through the wing is altered, and that flow strangulation would be a negative feature for flow access from one point to another point. Additionally, detailed structural analysis results for critical engine locations are presented. The results show that with the engine at 80% of the span, the flow of stress is in its most homogeneous form, and consequently, the occurrence of flutter is postponed the most.

Additionally, I used constructal law and the concept of the flow of stresses to explain the differences in flutter speeds of two different designs of flying wing aircraft;

swept and curved configurations. I considered different swept back and curved configuration while the positions of the wingtips for swept and curved configurations were identical. The flow of stresses is studied close and away from the flutter boundary. The results reveal that regardless of the curvature and sweep degree, the condition of the trim state, and the internal force distribution, the stresses patterns of distribution remain the same, while the only changes are the magnitudes of the stresses.

At fixed altitude and cruise speed, the aircraft is exposed to the same drag, lift, and thrust [68] – the same externally applied loads. Here, I showed that under the same working condition, if stress strangulation happens, the structure becomes unstable. This approach, based on the constructal law, shows how a degree of freedom in design will change the performance of the system.

Limitations and Future Works

There is a clear need to pursue and develop an evolutionary design theory that covers the entire range of design, all united under the same principles of physics. Theory enables us to envision the effect of curvature in the aeroelastic design of aircraft predictably and discovers the configuration with lower stress strangulation and a larger aeroelastic flight envelope.

This research provided a variety of designs and configurations. However, there are still many details in the design that can be investigated through the lens of constructal law. One of these problems is the design and arrangements of rips and spar in the wings that can affect the stability substantially. There are also dropped wing and gull wing designs that can be evaluated for their stability characteristics.

Moreover, the current aerodynamic theory used in NATASHA is a 2D thin airfoil theory that is suitable for a high-aspect-ratio wing and is fall short of simulating

physical phenomena like stall or flow separation. Improving the aerodynamic part of the developed numerical package helps to broaden the type of geometries and configurations that can be investigated. This package can be improved by incorporating 3D aerodynamic theories or linking the package to a CFD software.

BIBLIOGRAPHY

[1] A. Abdelkefi. Aeroelastic energy harvesting: A review. *International Journal of Engineering Science*, 100:112–135, 2016.

[2] A. V. Azad and M. Amidpour. Economic optimization of shell and tube heat exchanger based on constructal theory. *Energy*, 36(2):1087–1096, 2011.

[3] Y. Azoumah, N. Mazet, and P. Neveu. Constructal network for heat and mass transfer in a solid–gas reactive porous medium. *International Journal of Heat and mass transfer*, 47(14-16):2961–2970, 2004.

[4] J. G. Barmby, H. J. Cunningham, and I. Garrick. Study of effects of sweep on the flutter of cantilever wings. 1951.

[5] A. Bejan. Constructal-theory network of conducting paths for cooling a heat generating volume. *International Journal of Heat and Mass Transfer*, 40(4):799–816, 1997.

[6] A. Bejan. *Shape and structure, from engineering to nature.* Cambridge university press, 2000.

[7] A. Bejan. *The physics of life : the evolution of everything.* St. Martins Press, New York City, 2016.

[8] A. Bejan, V. Badescu, and A. De Vos. Constructal theory of economics structure generation in space and time. *Energy Conversion and Management*, 41(13):1429–1451, 2000.

[9] A. Bejan, J. Charles, and S. Lorente. The evolution of airplanes. *Journal of Applied Physics*, 116(4):044901, 2014.

[10] A. Bejan and S. Lorente. The constructal law and the thermodynamics of flow systems with configuration. *International Journal of Heat and Mass Transfer*, 47(14-16):3203–3214, 2004.

[11] A. Bejan and S. Lorente. Constructal theory of generation of configuration in nature and engineering. *Journal of Applied Physics*, 100(4), 2006.

[12] A. Bejan and S. Lorente. *Design with Constructal Theory.* Wiley, Hoboken, 2008.

[13] A. Bejan and S. Lorente. The constructal law of design and evolution in nature. *Philosophical Transactions of the Royal Society B: Biological Sciences*, 365(1545):1335–1347, 2010.

[14] A. Bejan and S. Lorente. The constructal law and the evolution of design in nature. *Physics of Life Reviews*, 8(3):209–240, 2011.

[15] A. Bejan and S. Lorente. Constructal law of design and evolution: Physics, biology, technology, and society. *Journal of Applied Physics*, 113(15):–, 2013.

[16] A. Bejan, S. Lorente, and A. Miguel. *Constructal human dynamics, security and sustainability*, volume 50. IOS Press, 2009.

[17] A. Benaouali and S. Kachel. Parametric design of aircraft wing with curved leading edge. *Problemy Mechatroniki: uzbrojenie, lotnictwo, inżynieria bezpieczeństwa*, 9, 2018.

[18] O. O. Bendiksen. Energy approach to flutter suppression and aeroelastic control. *Journal of Guidance, Control, and Dynamics*, 24(1):176–184, 2001.

[19] M. J. Carone, C. B. Williams, J. K. Allen, and F. Mistree. An application of constructal theory in the multi-objective design of product platforms. In *ASME 2003 International Design Engineering Technical Conferences and Computers and Information in Engineering Conference*, pages 719–730. American Society of Mechanical Engineers, 2003.

[20] C.-S. Chang and D. Hodges. Vibration characteristics of curved beams. *Journal of Mechanics of Materials and Structures*, 4(4):675–692, 2009.

[21] C.-S. Chang, D. H. Hodges, and M. J. Patil. Flight dynamics of highly flexible aircraft. *Journal of Aircraft*, 45(2):538–545, 2008.

[22] M. Chiarelli, M. Cagnoni, M. Ciabattari, M. De Biasio, and A. Massai. High aspect ratio wing with curved planform: Cfd and fe analyses. In *ICAS*, Nice, France, 2010.

[23] M. Chiarelli, G. Lombardi, and A. Nibio. A straight wing and a forward swept wing compared with a curved planform wing in the transonic regime. In *CEAS*, Venice, Italy, 2011.

[24] M. R. Chiarelli, M. Cagnoni, M. Ciabattari, M. De Biasio, and A. Massai. Preliminary analysis of a high aspect ratio wing with curved planform. In *AIDAA*, Milan, Italy, 2009.

[25] M. Dora. An investigation on naca 2312 aerofoil with curved and straight leading edge wing. *International Journal of Research*, 5(12):2435–2440, 2018.

[26] V. Falkner. Sweepback and wing taper: The effect of sweepback on the lift, drag, and aerodynamic centre of a tapered wing. *Aircraft Engineering and Aerospace Technology*, 22(10):296–300, 1950.

[27] S. Fazelzadeh, P. Marzocca, E. Rashidi, and A. Mazidi. Effects of rolling maneuver on divergence and flutter of aircraft wing store. *Journal of Aircraft*, 47(1):64–70, 2010.

[28] S. Fazelzadeh and A. Mazidi. Nonlinear aeroelastic analysis of bending-torsion wings subjected to a transverse follower force. *Journal of Computational and Nonlinear Dynamics*, 6(3):031016, 2011.

[29] S. Fazelzadeh, A. Mazidi, A. Rahmati, and P. Marzocca. The effect of multiple stores arrangement on flutter speed of a shear deformable wing subjected to pull-up angular velocity. *The Aeronautical Journal*, 113(1148):661–668, 2009.

[30] S. A. Fazelzadeh, A. H. Ghasemi, and A. Mazidi. Aeroelastic analysis of unrestrained aircraft wing with external stores under roll maneuver. *International Journal of Acoustics and Vibration*, 21(3):327–333, 2016.

[31] Y. C. Fung. *An introduction to the theory of aeroelasticity*. Courier Dover Publications, Mineola, New York, 2008.

[32] V. Galantai, A. Sofla, S. Meguid, K. Tan, and W. Yeo. Bio-inspired wing morphing for unmanned aerial vehicles using intelligent materials. *International Journal of Mechanics and Materials in Design*, 8(1):71–79, 2012.

[33] F. H. Gern and L. Librescu. Static and dynamic aeroelasticity of advanced aircraft wings carrying external stores. *AIAA journal*, 36(7):1121–1129, 1998.

[34] C. Geuzaine and J.-F. Remacle. Gmsh: A 3-d finite element mesh generator with built-in pre-and post-processing facilities. *International journal for numerical methods in engineering*, 79(11):1309–1331, 2009.

[35] M. Goland and Y. Luke. The flutter of a uniform wing with tip weights. *Journal of Applied Mechanics*, 15(1):13–20, 1948.

[36] J. Gundlach. *Designing Unmanned Aircraft Systems: A Comprehensive Approach*. American Institute of Aeronautics and Astronautics, Reston, Virginia, USA, 2012.

[37] Q. Guo and B. F. Song. The effect of structural geometric nonlinearities on the flutter of the straight and swept wing configurations. In *Applied Mechanics and Materials*, volume 189, pages 306–311. Trans Tech Publ, 2012.

[38] D. W. Hall, C. D. Fortenbach, E. V. Dimiceli, and R. W. Parks. A preliminary study of solar powdered aircraft and associated power trains. 1983.

[39] C. W. Harper and R. L. Maki. A review of the stall characteristics of swept wings. 1964.

[40] G. Hernandez, J. K. Allen, and F. Mistree. Design of hierarchic platforms for customizable products. In *ASME 2002 International Design Engineering Technical Conferences and Computers and Information in Engineering Conference*, pages 567–577. American Society of Mechanical Engineers, 2002.

[41] G. Hernandez, J. K. Allen, and F. Mistree. Platform design for customizable products as a problem of access in a geometric space. *Engineering Optimization*, 35(3):229–254, 2003.

[42] D. H. Hodges. Geometrically exact, intrinsic theory for dynamics of curved and twisted anisotropic beams. *AIAA journal*, 41(6):1131–1137, 2003.

[43] D. H. Hodges and G. A. Pierce. *Introduction to structural dynamics and aeroelasticity*, volume 15. Cambridge University Press, Cambridge, UK, 2011.

[44] G. Hodges. Active flutter suppression-b-52 controls configured vehicle. In *Dynamics Specialists Conference*, page 322, Williamsburg, VA, 1973.

[45] E. Izadpanahi and P. Mardanpour. Nonlinear aeroelastic response of highly flexible flying wing due to different gust loads. In M. Reyhanoglu, editor, *Nonlinear Systems*, chapter 5, pages 89–106. IntechOpen, 2018.

[46] E. Izadpanahi, S. Rastkar, and P. Mardanpour. Constructal design of flying wing aircraft: Curved and swept configurations. *AIAA Journal*, 0(0):1–16, 0.

[47] G. Karpouzian and L. Librescu. Nonclassical effects on divergence and flutter of anisotropic swept aircraft wings. *AIAA journal*, 34(4):786–794, 1996.

[48] Z. Kazancı and Z. Mecitoğlu. Nonlinear dynamic behavior of simply supported laminated composite plates subjected to blast load. *Journal of Sound and Vibration*, 317(3):883–897, 2008.

[49] M. M. I. Khan and A. Al-Faruk. Comparative analysis of aerodynamic characteristics of rectangular and curved leading edge wing planforms. *American Journal of Engineering Research*, 7(5):281–291, 2018.

[50] A. S. Lau, S. Haeri, and J. W. Kim. The effect of wavy leading edges on aerofoil–gust interaction noise. *Journal of Sound and Vibration*, 332(24):6234–6253, 2013.

[51] D. Lentink, U. Müller, E. Stamhuis, R. De Kat, W. Van Gestel, L. Veldhuis, P. Henningsson, A. Hedenström, J. J. Videler, and J. L. Van Leeuwen. How swifts control their glide performance with morphing wings. *Nature*, 446(7139):1082, 2007.

[52] F.-M. Li. Active aeroelastic flutter suppression of a supersonic plate with piezoelectric material. *International Journal of Engineering Science*, 51:190–203, 2012.

[53] L. Librescu, S. Na, P. Marzocca, C. Chung, and M. K. Kwak. Active aeroelastic control of 2-d wing-flap systems operating in an incompressible flowfield and impacted by a blast pulse. *Journal of Sound and Vibration*, 283(3):685–706, 2005.

[54] X. Liu, L. Chen, H. Feng, and F. Sun. Constructal design for blast furnace wall based on the entransy theory. *Applied Thermal Engineering*, 100:798–804, 2016.

[55] Y. Liu, C. Xie, C. Yang, and J. Cheng. Gust response analysis and wind tunnel test for a high-aspect ratio wing. *Chinese Journal of Aeronautics*, 29(1):91–103, 2016.

[56] S. Lorente. Constructal view of electrokinetic transfer through porous media. *Journal of Physics D: Applied Physics*, 40(9):2941–2947, apr 2007.

[57] S. Lorente, J. Lee, and A. Bejan. The "flow of stresses" concept: The analogy between mechanical strength and heat convection. *International Journal of Heat and Mass Transfer*, 53(15-16):2963–2968, 2010.

[58] G. Lorenzini, C. Biserni, L. Isoldi, E. Dos Santos, and L. Rocha. Constructal design applied to the geometric optimization of y-shaped cavities embedded in a conducting medium. *Journal of Electronic Packaging*, 133(4):041008, 2011.

[59] I. Lottati. Aeroelastic stability characteristics of a composite swept wing withtip weights for an unrestrained vehicle. *Journal of Aircraft*, 24(11):793–802, 1987.

[60] J. G. Lowry and J. F. Cahill. Review of the maximum-lift characteristics of thin and swept wings. 1951.

[61] A. Malley-Ernewein and S. Lorente. Constructal design of thermochemical energy storage. *International Journal of Heat and Mass Transfer*, 130:1299 – 1306, 2019.

[62] P. Mardanpour, D. H. Hodges, R. Neuhart, and N. Graybeal. Engine placement effect on nonlinear trim and stability of flying wing aircraft. *Journal of Aircraft*, 50(6):1716–1725, 2013.

[63] P. Mardanpour, D. H. Hodges, and R. Rezvani. Nonlinear aeroelasticity of high-aspect-ratio wings excited by time-dependent thrust. *Nonlinear Dynamics*, 75(3):475–500, 2014.

[64] P. Mardanpour, E. Izadpanahi, S. Rastkar, S. Calastawad, and C. Levy. Effect of shooting and blast-induced gust on nonlinear aeroelastic stability and behavior of high-aspect ratio wing. *Journal of Sound and Vibration*, 433:299–313, 2018.

[65] P. Mardanpour, E. Izadpanahi, S. Rastkar, and D. H. Hodges. Effects of engine placement on nonlinear aeroelastic gust response of high-aspect-ratio wings. In *AIAA Modeling and Simulation Technologies Conference*, page 0576, 2017.

[66] P. Mardanpour, E. Izadpanahi, S. Rastkar, and D. H. Hodges. Nonlinear aeroelastic gust suppression and engine placement. *Journal of Aircraft*, 54(6):2402–2404, 2017.

[67] P. Mardanpour, E. Izadpanahi, S. Rastkar, S. Lorente, and A. Bejan. Constructal design of aircraft: Flow of stresses and aeroelastic stability. *AIAA Journal*, 57(10):4393–4405, 2019.

[68] P. Mardanpour, P. W. Richards, O. Nabipour, and D. H. Hodges. Effect of multiple engine placement on aeroelastic trim and stability of flying wing aircraft. *Journal of Fluids and Structures*, 44:67–86, 2014.

[69] P. Marzocca, L. Librescu, and G. Chiocchia. Aeroelastic response of 2-d lifting surfaces to gust and arbitrary explosive loading signatures. *International Journal of Impact Engineering*, 25(1):41–65, 2001.

[70] P. Marzocca, L. Librescu, and G. Chiocchia. Aeroelastic response of a 2-d airfoil in a compressible flow field and exposed to blast loading. *Aerospace Science and Technology*, 6(4):259–272, 2002.

[71] A. Mazidi and S. Fazelzadeh. Flutter of a swept aircraft wing with a powered engine. *Journal of Aerospace Engineering*, 23(4):243–250, 2009.

[72] A. Mazidi and S. Fazelzadeh. Aeroelastic modeling and flutter prediction of swept wings carrying twin powered engines. *Journal of Aerospace Engineering*, 26(3):586–593, 2011.

[73] A. Mazidi, S. Fazelzadeh, and P. Marzocca. Flutter of aircraft wings carrying a powered engine under roll maneuver. *Journal of Aircraft*, 48(3):874–883, 2011.

[74] A. Mazidi, H. Kalantari, and S. Fazelzadeh. Aeroelastic response of an aircraft wing with mounted engine subjected to time-dependent thrust. *Journal of Fluids and Structures*, 39:292–305, 2013.

[75] G. W. Merkx. Flow systems, catastrophes, and public policy. *Constructal Human Dynamics, Security and Sustainability*, 50:37, 2009.

[76] A. Miguel. Dendritic structures for fluid flow: laminar, turbulent and constructal design. *Journal of Fluids and Structures*, 26(2):330–335, 2010.

[77] W. Molyneux and H. Hall. *The aerodynamic effects of aspect ratio and sweepback on wing flutter*. Citeseer, 1957.

[78] M. Mosa, M. Labat, and S. Lorente. Role of flow architectures on the design of radiant cooling panels, a constructal approach. *Applied Thermal Engineering*, 150:1345 – 1352, 2019.

[79] S. Na and L. Librescu. Dynamic response of adaptive cantilevers carrying external stores and subjected to blast loading. *Journal of Sound and Vibration*, 231(4):1039–1055, 2000.

[80] N. Nguyen, K. Trinh, K. Reynolds, J. Kless, M. Aftosmis, and J. Urnes. Elastically shaped wing optimization and aircraft concept for improved cruise efficiency. In *51st AIAA Aerospace Sciences Meeting Including the New Horizons Forum and Aerospace Exposition*, page 141, 2013.

[81] T. E. Noll, J. M. Brown, M. E. Perez-Davis, S. D. Ishmael, G. C. Tiffany, and M. Gaier. Investigation of the helios prototype aircraft mishap volume i mishap report. 9, 2004.

[82] T. E. Noll, S. D. Ishmael, B. Henwood, M. E. Perez-Davis, G. C. Tiffany, J. Madura, M. Gaier, J. M. Brown, and T. Wierzbanowski. Technical findings, lessons learned, and recommendations resulting from the helios prototype vehicle mishap. Technical report, NATIONAL AERONAUTICS AND SPACE ADMIN LANGLEY RESEARCH CENTER HAMPTON VA, 2007.

[83] M. Patil. Energy perspectives in aeroelastic control. In *44th AIAA/ASME/ASCE/AHS/ASC Structures, Structural Dynamics, and Materials Conference*, page 1800, 2003.

[84] M. J. Patil. Nonlinear gust response of highly flexible aircraft. In *Proc. 48th AIAA, Structural Dynamics, and Materials Conf*, pages 2007–2103, 2007.

[85] M. J. Patil and D. H. Hodges. On the importance of aerodynamic and structural geometrical nonlinearities in aeroelastic behavior of high-aspect-ratio wings. *Journal of Fluids and Structures*, 19(7):905–915, 2004.

[86] M. J. Patil and D. H. Hodges. Flight dynamics of highly flexible flying wings. *Journal of Aircraft*, 43(6):1790–1799, 2006.

[87] M. J. Patil, D. H. Hodges, and C. E. S. Cesnik. Nonlinear aeroelasticity and flight dynamics of high-altitude long-endurance aircraft. *Journal of Aircraft*, 38(1):88–94, 2001.

[88] M. J. Patil and D. J. Taylor. Gust response of highly flexible aircraft. In *Proceedings of the 47th Structures, Structural Dynamics, and Materials Conference, Newport, Rhode Island*, Reston, Virginia, May 2006. AIAA. AIAA-2006-1638.

[89] D. A. Peters and M. J. Johnson. Finite-state airloads for deformable airfoils on fixed and rotating wings. In *Symposium on Aeroelasticity and Fluid/Structure Interaction, Proceedings of the Winter Annual Meeting, AD Volume 44*, pages 1 – 28. ASME, November 6 – 11, 1994.

[90] D. A. Peters, S. Karunamoorthy, and W.-M. Cao. Finite state induced flow models. i-two-dimensional thin airfoil. *Journal of Aircraft*, 32(2):313–322, 1995.

[91] S. Powell, E. Izadpanahi, S. Rastkar, and P. Mardanpour. Constructal approach to the design of inflected airplane wings. In *AIAA Scitech 2019 Forum*, page 0226, 2019.

[92] V. A. P. Raja, T. Basak, and S. K. Das. Thermal performance of a multi-block heat exchanger designed on the basis of bejan's constructal theory. *International Journal of Heat and Mass Transfer*, 51(13-14):3582–3594, 2008.

[93] A. P. Ricciardi, M. J. Patil, R. A. Canfield, and N. Lindsley. Evaluation of quasi-static gust loads certification methods for high-altitude long-endurance aircraft. *Journal of Aircraft*, 50(2):457–468, 2013.

[94] A. Sofla, S. Meguid, K. Tan, and W. Yeo. Shape morphing of aircraft wing: Status and challenges. *Materials & Design*, 31(3):1284–1292, 2010.

[95] Z. Sotoudeh, D. H. Hodges, and C.-S. Chang. Validation studies for aeroelastic trim and stability of highly flexible aircraft. *Journal of Aircraft*, 47(4):1240–1247, 2010.

[96] D. Tang, P. Attar, and E. H. Dowell. Flutter/limit cycle oscillation analysis and experiment for wing-store model. *AIAA journal*, 44(7):1662–1675, 2006.

[97] D. Tang and E. H. Dowell. Experimental and theoretical study of gust response for a wing–store model with freeplay. *Journal of Sound and Vibration*, 295(3):659–684, 2006.

[98] M. Trancossi, A. Dumas, and M. Madonia. Optimization of airships with constructal design for efficiency method. Technical report, SAE Technical Paper, 2013.

[99] H. Türkmen and Z. Mecitoğlu. Dynamic response of a stiffened laminated composite plate subjected to blast load. *Journal of Sound and Vibration*, 221(3):371–389, 1999.

[100] C. Van Dam. Induced-drag characteristics of crescent-moon-shaped wings. *Journal of Aircraft*, 24(2):115–119, 1987.

[101] T. Wattez and S. Lorente. From pore network prediction based on the constructal law to macroscopic properties of porous media. *Journal of Physics D: Applied Physics*, 48(48):485503, nov 2015.

[102] A. Wickenheiser and E. Garcia. Aerodynamic modeling of morphing wings using an extended lifting-line analysis. *Journal of Aircraft*, 44(1):10–16, 2007.

[103] J. Xiang, Y. Wu, and D. Li. Energy harvesting from the discrete gust response of a piezoaeroelastic wing: Modeling and performance evaluation. *Journal of Sound and Vibration*, 343:176–193, 2015.

[104] J. Yang, S.-R. Oh, and W. Liu. Optimization of shell-and-tube heat exchangers using a general design approach motivated by constructal theory. *International Journal of Heat and Mass Transfer*, 77:1144–1154, 2014.

[105] J. Youngblood and T. Talay. Solar-powered airplane design for long-endurance, high-altitude flight. In *2nd International Very Large Vehicles Conference*, page 811, 1982.

[106] W. Yu and D. H. Hodges. Generalized timoshenko theory of the variational asymptotic beam sectional analysis. *Journal of the American Helicopter Society*, 50(1):46–55, 2005.

[107] W. Yu, D. H. Hodges, and J. C. Ho. Variational asymptotic beam sectional analysis–an updated version. *International Journal of Engineering Science*, 59:40–64, 2012.

[108] W. Yu, D. H. Hodges, V. Volovoi, and C. E. Cesnik. On timoshenko-like modeling of initially curved and twisted composite beams. *International Journal of Solids and Structures*, 39(19):5101–5121, 2002.

[109] W. Yu, V. V. Volovoi, D. H. Hodges, and X. Hong. Validation of the variational asymptotic beam sectional analysis. *AIAA journal*, 40(10):2105–2112, 2002.

VITA

EHSAN IZADPANAHI

2011	B.S., Mechanical Engineering Yasouj University Yasouj, Iran
2014	M.S., Mechanical Engineering Chamran Ahvaz University Ahvaz, Iran
2020	Ph.D., Mechanical Engineering Florida International University Miami, Florida

Publications

Mardanpour, P., Izadpanahi, E., Rastkar, S., and Hodges, D. H. (2017). *Nonlinear Aeroelastic Gust Suppression and Engine Placement.* Journal of Aircraft, 54(6):2402-2404.

Mardanpour, P., Izadpanahi, E., Rastkar, S., and Hodges, D. H. (2017). *Effects of Engine Placement on Nonlinear Aeroelastic Gust Response of High-Aspect-Ratio Wings.* In AIAA Modeling and Simulation Technologies Conference, p. 0576.

Mardanpour, P., Izadpanahi, E., Rastkar, S., Fazelzadeh, S. A., and Hodges, D. H. (2017). *Geometrically-exact, fully intrinsic analysis of pretwisted beams under distributed follower forces.* In 58th AIAA/ASCE/AHS/ASC Structures, Structural Dynamics, and Materials Conference, p. 1986.

Ehsan Izadpanahi and Pezhman Mardanpour (July 18th 2018). *Nonlinear Aeroelastic Response of Highly Flexible Flying Wing Due to Different Gust Loads.* Nonlinear Systems Mahmut Reyhanoglu, IntechOpen, DOI: 10.5772/intechopen.75804.

Mardanpour, P., Izadpanahi, E., Rastkar, S., Fazelzadeh, S. A., and Hodges, D. H. (2018). *Geometrically Exact, Fully Intrinsic Analysis of Pre-Twisted Beams Under Distributed Follower Forces.* AIAA Journal, 56(2):836-848.

Mardanpour, P., Izadpanahi, E., Rastkar, S., Calastawad, S., and Levy, C. (2018). *Effect of shooting and blast-induced gust on nonlinear aeroelastic stability and behavior of high-aspect ratio wing.* Journal of Sound and Vibration, 433:299-313.

Mardanpour, P., Izadpanahi, E., Rastkar, S., Lorente, S., and Bejan, A. (2018). *Constructal Approach in Design of High Aspect Ratio Aircraft: The Concept of Flow of Stresses and Aeroelastic Stability.* IMECE conference, Pisburgh, PA.

Izadpanahi, E., Powell, S., Rastkar, S., and Mardanpour, P., (2018). *Constructal Approach for Stability Analysis of Initially Twisted Beam Under Distributed Follower Forces.* IMECE conference, Pisburgh, PA.

Mardanpour, P., Izadpanahi, E., Rastkar, S., Calastawad, S., and Levy, C. (2018). *Effects of Armament Placement on Nonlinear Dynamic Behavior of High-aspect Ratio Wing Due to Shooting and Blast-Induced Gust.* In 2018 Fluid Dynamics Conference, AIAA AVIATION Forum, p. 3391.

Mardanpour, P., Izadpanahi, E., Rastkar, S., Lorente, S., and Bejan, A. (2019). *Constructal Design of Aircraft: Flow of Stresses and Aeroelastic Stability.* AIAA Journal, 57(10):4393-4405.

Izadpanahi, E., Rastkar, S., Zisis, I., Fazelzadeh, S. A., and Mardanpour, P. (2019). *Nonlinear time domain and stability analysis of beams under partially distributed follower force.* Applied Mathematical Modelling, 73:303-326.

Izadpanahi, E., Rastkar, S., and Mardanpour, P. (2019). *Constructal Design of Flying Wing Aircraft: Curved and Swept Configurations.* AIAA Journal, 1-16.

Powell, S., Izadpanahi, E., Rastkar, S., and Mardanpour, P. (2019). *Constructal Approach to the Design of Inflected Airplane Wings.* In AIAA Scitech 2019 Forum, p. 0226.

Mardanpour, P., Izadpanahi, E., Rastkar, S., Camberos, J. A., Lorente, S., and Bejan, A. (2019). *Constructal Approach in Aeroelastic Design and Analysis of Flying Wing Aircraft.* In AIAA Scitech 2019 Forum, p. 0552.